

© Copyright by Tanushree Sinha 2014
All Rights Reserved

Atomistic Study of Fracture and Deformation Mechanisms in Nanotwinned FCC Metals

A Dissertation

Presented to

the Faculty of the Department of Mechanical Engineering

University of Houston

In Partial Fulfillment

of the Requirements for the Degree

Doctor of Philosophy

in Mechanical Engineering

by

Tanushree Sinha

August 2014

Atomistic Study of Fracture and Deformation Mechanisms in Nanotwinned FCC Metals

Tanushree Sinha

Approved:

Chair of the Committee
Yashashree Kulkarni, Assistant
Professor,
Mechanical Engineering

Committee Members:

Pradeep Sharma, Professor,
Mechanical Engineering

Kalyana Nakshatrala, Assistant
Professor,
Civil Engineering

Ken White, Professor,
Mechanical Engineering

Anastassios Mavrokefalos, Assistant
Professor,
Mechanical Engineering

Suresh K. Khator, Associate Dean,
Cullen College of Engineering

Pradeep Sharma, Department Chair,
Mechanical Engineering

In loving memory of my grandparents,
Dida and Dadu

Wish you were here...

Acknowledgements

I take this opportunity to express my profound gratitude and deep regards to my supervisor, Dr. Yashashree Kulkarni, whose valuable guidance and encouragement helped me successfully complete this research. She showed utmost patience in reading and correcting my paper and dissertation drafts. I thank her for her constructive criticisms. I am also grateful for her financial support to complete my studies. I am truly thankful to my dissertation defense committee, Dr. Pradeep Sharma, Dr. Ken White, Dr. Kalyana Nakshatrala, and Dr. Anastasios Mavrokefalos for taking the time and patience to go through my work and providing valuable input on my thesis.

I am especially grateful to Dr. Sharma for being such an enthusiastic mentor and for his benevolent personality. His amiable suggestions have often proven to be the life-jacket in a sinking boat. My sincere thanks to Dr. White for his guidance and the knowledge that he has imparted to me. His acute insight and the depth of his knowledge base in the field of Materials Engineering are indeed inspiring. I have also benefited greatly from the fruitful discussions and suggestions from Dr. Nakshatrala. I have learned so much from him and am deeply grateful to him for lending his expertise and intuition to engineering and technical problems.

I would like to acknowledge my wonderful lab-mates for their congeniality and support all through my PhD. A special thanks to Qian and Dengke who have willingly discussed ideas with me whenever I thought my research had reached a stalemate. It has been an absolute pleasure to know Farah and Sana, who have graciously opened their doors for me to experience Tunisian cuisine and a convivial culture. I am extremely fortunate to have met Shuyin, who has always been there for me during my highs and lows and proven to be my confidant and

my best friend. I am ever-grateful to her for this invaluable friendship.

I shall always remain indebted to my parents for their unconditional love, relentless support, and countless sacrifices that they have made for me. They have been my primary source of inspiration in life and this achievement would have simply been impossible without them. I am obliged to my sister, Debashree, for the reinforcement she provided to me throughout the course of my graduate studies. I have been so blessed to have such a kind-hearted and loving sister. I am grateful to my kitties, Mowgli and Minnie, for being my silly little entertainers and loyal companions. Even at the oddest hours of the night, their companionship makes my task seemingly easy. I fall short of words to express my gratitude to my husband, Aaron McClellan, for his enduring love and doubtless faith in me even during the hardest times. He has been my guide and support at every step and has helped me to get through this agonizing period in the most positive way. Thank you for always bringing a smile to my face.

Finally, I would like to dedicate this dissertation to the loving memory of my grandparents (Dida and Dadu) who I lost in the past year. Their selflessness, patience, and generosity are inexplicable. I owe them so much for the kindness and love they showered on me. It is heart-breaking to not be able to share this moment of happiness that they were so eagerly waiting for. They are very close to my heart and mind, even though they have gone to the other side of the veil.

Atomistic Study of Fracture and Deformation Mechanisms in Nanotwinned FCC Metals

An Abstract
of a
Dissertation
Presented to
the Faculty of the Department of Mechanical Engineering
University of Houston

In Partial Fulfillment
of the Requirements for the Degree
Doctor of Philosophy
in Mechanical Engineering

by
Tanushree Sinha

August 2014

Abstract

Nanotwinned metals have opened up exciting avenues for the design of high-strength, high-ductility materials owing to the extraordinary properties of twin boundaries. This dissertation presents insights into the deformation mechanisms governing the high temperature response and fracture behavior of nanotwinned face-centered-cubic (fcc) metals using molecular dynamics simulations. The aim of our atomistic modeling is to elucidate the role of coherent twin boundaries (CTB) in the interaction with dislocations (thus mediating strength and hardening) and in inhibiting crack propagation (thus contributing to toughness).

Our simulations reveal an intriguing transition in the behavior of CTBs at higher temperatures as the deformation mechanism changes from shear-coupled normal motion to deformation twinning, an occurrence that has not been reported before in fcc metals. This anomalous response of twin boundaries at high temperatures is studied for different fcc metals and analyzed based on the energetics of the competing mechanisms.

Our simulations of pre-existing cracks along CTBs reveal that CTBs in nanotwinned structures exhibit alternating intrinsic brittleness and intrinsic ductility. This is a startling consequence of the directional anisotropy of an atomically sharp crack along a twin boundary that favors cleavage in one direction and dislocation emission from the crack tip in the opposite direction owing to the effect of the crystallographic orientations in the adjoining twins. These results shed light on the previously held notion that twin boundaries are inherently brittle, and can also explain the brittle versus ductile behavior of CTBs reported in recent literature.

We also investigate the effect of twin boundary spacing, and sample thickness on the crack-propagation in twinned nanopillars. The simulations show that

CTBs serve as effective barriers for dislocation motion and restrict the plasticity in the vicinity of the crack tip. We finally extend our study of crack propagation to polycrystalline nanotwinned structures. We observe multiple mechanisms such as dislocation-twin interactions, twin migration, and dislocation nucleation from grain boundaries that govern the ductile response of a pre-existing crack.

The findings reported in this dissertation demonstrate remarkable properties of twin boundaries and open further avenues for the design of novel nanotwinned structures for next-generation structural applications.

Table of Contents

Acknowledgements	vi
Abstract	ix
Table of Contents	xi
List of Figures	xiv
List of Tables	xvii
Chapter 1 Introduction	1
1.1 Motivation	1
1.2 Dissertation Outline	3
1.3 Computational Modeling	4
1.3.1 Atomistic Approach - Molecular Dynamics	5
1.4 Literature Review	9
1.4.1 Properties of Nanostructured Materials	10
1.4.2 Behavior of Nanotwinned Metals	16
1.4.3 Fracture in Nanotwinned FCC Metals	25
Chapter 2 Anomalous Deformation Twinning in FCC Metals at High Tem- peratures	30
2.1 Introduction	30
2.2 Methodology	31
2.3 Results	32
2.3.1 Response at Low and Intermediate Temperatures	32
2.3.2 Response at High Temperatures	34
2.3.3 Response of Various FCC Metals	37
2.4 Discussion	39
2.5 Conclusion	43
Chapter 3 Alternating Brittle and Ductile Response of Twin boundaries in Nanotwinned Structures	47

3.1	Introduction	47
3.2	Methodology	48
3.3	Results & Discussion	49
3.3.1	Response of Bicrystal	49
3.3.2	Response of Nanotwinned Pillar	53
3.3.3	Response of Blunt Cracks	56
3.4	Conclusion	61
Chapter 4 Crack Propagation in Twinned Nanopillars		65
4.1	Introduction	65
4.2	Methodology	65
4.3	Results	67
4.3.1	Single Crystal - 0TB	67
4.3.2	Twinned Sample - 4TB	67
4.4	Discussion	69
4.4.1	Effect of Sample Thickness	69
4.4.2	Effect of Twin Boundaries	75
4.4.3	Effect of Twin-Spacing	79
4.4.4	Effect of Different FCC Metals	79
4.5	Conclusion	81
Chapter 5 Fracture Response of Nanotwinned Polycrystalline Copper with Columnar Grains		83
5.1	Introduction	83
5.2	Methodology	83
5.3	Results & Discussion	86
5.3.1	Effect of Twin Spacing	86
5.3.2	Effect of a Cracked TB	92
5.3.3	Effect of Crack Orientation	95

5.4 Conclusion	99
Chapter 6 Summary and Future Directions	101
6.0.1 Conclusions	101
6.0.2 Limitations and Future Work	104
References	106

List of Figures

Figure 1.1	Synthesis of Nanostructures	11
Figure 1.2	Stress-strain plots for Cu for various grain sizes	12
Figure 1.3	Hardness versus grain size plots for Cu and Pd	14
Figure 1.4	Stress-strain plots for Cu for various grain sizes	15
Figure 1.5	TEM Images of twinned and untwinned Cu	17
Figure 1.6	Tensile response of nanotwinned Cu at different strain-rates and twin-density	18
Figure 1.7	Effect of twin-spacing on rate-sensitivity and activation volume .	19
Figure 1.8	Effectiveness of TBs on mechanical properties of pure Cu	20
Figure 1.9	Critical twin-thickness for maximum strength in Cu	22
Figure 1.10	Electrical resistivity of Cu as a function of temperature	24
Figure 1.11	Comparison of crack propagation in nanostructured Cu	26
Figure 1.12	Comparison of fracture toughness curves for nanostructured Cu	27
Figure 1.13	TEM images during crack propagation in nanotwinned Ag	28
Figure 1.14	Failure modes in nanotwinned bicrystals	29
Figure 2.1	Shear stress-strain response at various temperatures for bicrystals	32
Figure 2.2	The normal displacement of the CTB with time at 0 K	34
Figure 2.3	Position of the CTB at different strains for 0 K	35
Figure 2.4	Position of the CTB at different strains for 1200 K	36
Figure 2.5	Schematic representation of twin motion and twin formation . .	37
Figure 2.6	Stress-strain plots for different fcc metals at $\sim 0.7 T_m$	38
Figure 2.7	Energy curves for different mechanisms in fcc metals	43
Figure 2.8	Strain rate response of bicrystals at $T = 300$ K and 1200 K	45
Figure 3.1	Crystallographic orientation and atomistic images of samples . .	48
Figure 3.2	Left and right crack-tips on a + CTB	50
Figure 3.3	Evolution of left and right cracks on a + CTB in a bicrystal	50

Figure 3.4	System and local stress versus strain curves for bicrystal	52
Figure 3.5	Left crack-tips on + and - CTBs	53
Figure 3.6	Evolution of a left crack on + and - CTBs	54
Figure 3.7	Dislocation reactions occurring at different crack tips	55
Figure 3.8	Deformation in a nanopillar with crack on a + CTB	57
Figure 3.9	Deformation in a nanopillar with crack on a - CTB	58
Figure 3.10	Evolution of a blunt crack along different CTB	59
Figure 3.11	System and local stress curves for nanotwinned samples	60
Figure 3.12	Deformation in a nanopillar with blunt crack on a + CTB	62
Figure 3.13	Deformation in a nanopillar with blunt crack on a - CTB	63
Figure 4.1	Crystallographic orientation of a nanopillar with 4 TBs	66
Figure 4.2	Deformation in a 7nm thick 0TB sample	68
Figure 4.3	Deformation in a 7nm thick 4TB sample with $\lambda = 6\text{nm}$	69
Figure 4.4	Deformation in 0TB samples for different thicknesses	71
Figure 4.5	Stress-strain curves of 0TB samples with different thicknesses	72
Figure 4.6	Deformation in 4TB samples with $\lambda = 6\text{nm}$ for different thicknesses	73
Figure 4.7	Stress-strain curves of 4TB samples with $\lambda = 8\text{nm}$ for different thicknesses	74
Figure 4.8	Stress-strain curves of 4TB samples with $\lambda = 6\text{nm}$ for different thicknesses	75
Figure 4.9	Stress-strain curves for the 7nm thick 0TB and 4TB samples	77
Figure 4.10	Stress-strain curves for 10 nm thick 0TB and 4TB samples	78
Figure 4.11	Stress-strain curves for 14 nm thick 0TB and 4TB samples	78
Figure 4.12	Stress-strain response of 18 nm thick 0TB and 4TB samples with different thicknesses	79
Figure 4.13	Deformation in 10nm thick 4TB samples for different λ	80

Figure 4.14	Deformation in 12nm thick 4TB samples of Al and Ag	81
Figure 5.1	Relaxed twinned and untwinned polycrystalline digital samples	84
Figure 5.2	Stress-strain curves for untwinned and twinned polycrystals . .	86
Figure 5.3	Deformation of untwinned sample with a horizontal crack	88
Figure 5.4	Deformation of pre-cracked twinned sample with $\lambda = 5$ nm . . .	90
Figure 5.5	Deformation of pre-cracked twinned sample with $\lambda = 3$ nm . . .	91
Figure 5.6	TB migration and annihilation process in a twinned sample . . .	92
Figure 5.7	Deformation of twinned sample with $\lambda = 3$ nm with a horizontal crack along a TB	93
Figure 5.8	Brittle and ductile crack-tips on a TB	94
Figure 5.9	Stress-strain curves of a twinned samples of $\lambda = 3$ nm with different horizontal cracks	95
Figure 5.10	A relaxed twinned polycrystal with a vertical crack	95
Figure 5.11	Stress-strain curves of untwinned samples with different crack orientations	96
Figure 5.12	Stress-strain curves of a twinned samples of $\lambda = 5$ nm with different crack orientations	96
Figure 5.13	Deformation of untwinned and twinned polycrystals with a ver- tical crack	98
Figure 5.14	Stress-strain curves of untwinned and twinned polycrystals with a vertical crack	99

List of Tables

Table 2.1	Shear moduli, stacking fault energies and β of various fcc metals	42
Table 3.1	Response of an atomically sharp crack-tip based on CTB and crack type	53
Table 4.1	Variation of YS and UTS with thickness of 0TB samples	70
Table 4.2	Variation of YS and UTS with thickness of 4TB samples with $\lambda = 8\text{nm}$	74
Table 4.3	Variation of YS and UTS with thickness of 4TB samples with $\lambda = 6\text{nm}$	75
Table 4.4	Comparision of YS of the 0TB and 4TB samples	77
Table 4.5	Comparision of UTS of the 0TB and 4TB samples	77
Table 5.1	YS and UTS for the untwinned and twinned polycrystals	87

CHAPTER 1 INTRODUCTION

1.1 Motivation

The study of the mechanical properties of materials at the nano and sub-micron scales is motivated by the drive towards miniaturization in engineering and technology, and the need for novel materials to facilitate the application of nanotechnology in electronics, thermoelectrics, photonics, mechanical systems, and life sciences, to name a few. As the critical size feature of modern devices continue to shrink, extensive research is focused on the development and implementation of next-generation interconnects in order to incorporate increasingly small feature sizes with high performance and reliability in a cost-effective manner. Advances in the design of nanostructured materials are also being explored for next-generation structural applications in defense, energy, and biomedical industry. Once the characteristic size of materials reaches nanoscale, the mechanical properties change drastically and the classical mechanisms that dictate the deformation of bulk materials cease to hold and atomistic insights to predict the response of the nanostructured materials become vital.

Gleiter [1] made the visionary observation that metals and alloys, if made nanocrystalline, would possess a number of highly attractive properties as compared to their fine grained, or conventional microcrystalline counterparts. Following this, the nineties witnessed an intensity of research on nanocrystalline metals owing to their ultra-high strength compared to the conventional polycrystalline metals. However, as advances led to further insight into the governing deformation mechanisms, they also revealed a number of issues that seriously restrict the utility of the enhanced properties achievable by nanostructuring. The early enthusiasm was met with severe disappointment due to their brittle nature

and loss of structural stability as discussed in section 1.4.1. One of the major issues that severely impacted the practical application of nanocrystalline metals is that their ductility is typically limited to a few percent, and reduces further with decreasing grain size. Furthermore, it is well established that when grain sizes fall below 100 nm, there is a radical transition in the deformation mechanisms as grain boundary mediated processes, such as defect nucleation from GBs and GB sliding, become dominant. Among other consequences, this leads to undesirable grain instability as indicated by stress-induced grain growth, which ultimately results in the loss of strength, and possibly other benefits of nanocrystallinity.

A particularly intriguing development that has drawn focused attention in the past decade or so is the research on the attractive properties of nanotwinned face-centered-cubic (fcc) metals, which has provided compelling evidence that nanotwinned structures may be the optimal motifs for the design of both high-strength high-ductility materials. Nanotwinned Cu has been studied and processed and what is reported are an array of truly excellent properties, including high strength, substantial ductility, and high strain rate sensitivity. Significant progress is also made concerning the mechanistic modeling of deformation processes in nanotwinned fcc metals, and these lead to quite specific proposed pathways for further understanding of the mechanisms involved and for truly novel material development. However, these advances also reveal a number of issues concerning nanocrystalline and nanotwinned materials that, unless resolved, will seriously restrict the utility of some of the more enhanced properties achievable by nanostructuring. Some of these issues are pertaining to grain size stability and anomaly in the fracture response of twin boundaries. Although structural instability is a critical issue that limits the benefits of nanostructures, it remains relatively unaddressed so far in the context of nanotwinned metals, especially at high temperatures. Some recent works observe the intrinsic brittle behavior of

coherent twin boundaries in both experiments and simulations, but a systematic study of the geometric constraints that lead to the intrinsically brittle or intrinsically ductile behavior of twin boundaries is not reported.

The main objective of our research is to focus on resolving some of these critical issues in nanotwinned fcc metals especially involving grain stability and fracture, as well as further exploring their sensitivity to temperature, twin boundary spacing, and sample dimensions. It provides insights into the fracture mechanisms within nanotwinned metals and investigates the role of twin boundaries and size-effects in their brittle versus ductile behavior, a subject not investigated quantitatively to date. These studies involve analyzing the underlying atomistic deformation mechanisms governing the observed behaviors of nanostructured fcc metals using molecular dynamics simulation technique. Atomistic simulations are employed to simulate the deformation and crack propagation mechanisms in nanotwinned fcc metals. Dislocation characterization techniques are used to thoroughly investigate the underlying deformation mechanisms, identify the dislocation reactions and elucidate the relationship between these mechanisms with the observed properties. Materials modeled and tested through simulations include the fcc metals Cu, Ag, Al, and Pd, covering a range of stacking fault energies and elastic moduli.

1.2 Dissertation Outline

This dissertation is organized into 6 chapters. Chapter 1 provides an introduction and motivation for this dissertation along with an overview of the atomistic modeling approach employed in this research work. It also presents a review of the literature that focuses on studying the properties of nanostructured metals through experiments as well as computational and theoretical modeling. In Chapter 2, we investigate the high temperature stability of coherent twin boundaries in

different fcc metals. Anomalous deformation twinning is observed at high temperatures and is explained in terms of the temperature sensitivity of the different competing mechanisms. Chapter 3 provides insights into the propagation of pre-existing edge cracks along coherent twin boundaries and reveals an alternating brittle and ductile behavior of twin boundaries elucidated with respect to the effect of the crystallographic orientations in the adjoining twins. Chapter 4 further explores the role of twin boundaries in the deformation and fracture mechanisms in a nanotwinned pillar with a pre-existing edge crack. Chapter 5 extends the analysis of the fracture response of nanotwinned metals to polycrystalline samples, comprising of columnar hexagonal grains, containing an elliptical crack. Finally, Chapter 6 concludes this dissertation by summarizing the highlights and limitations of the work and presenting some avenues for future investigations.

1.3 Computational Modeling

One of the primary motives for computer simulation is the ability to gain atomistic insight into complex physical systems and processes that are inaccessible through experiments. Although experimental investigation of nanoscale materials are now possible with advanced techniques and design of sophisticated equipments for synthesis, metallurgical and physical characterizations, and property analyses, various computational techniques enable predictive capabilities for a quantitative understanding of the microstructure and its relation to the properties of nanostructured materials. Material properties are highly dependent on various phenomena occurring at different length as well as time scales. At the atomic scales, the effects of large collections of defects including grain boundaries, dislocation pile-ups at the grain boundaries, and other microstructural elements are significant, while at an engineering scale, contributions arising from macroscopic stresses and/or temperature gradients become profound and govern macroscopic

material properties [2]. There are several computational modeling schemes and the appropriate choice depends on the type of problem and scale of the physical phenomena under consideration.

1.3.1 Atomistic Approach - Molecular Dynamics

Molecular dynamics directly models the atoms and therefore directly incorporates the atomic length and time scales of the crystal directly into the computation. Individual atoms interact through forces defined by interatomic potential functions. These potential functions are phenomenological approximations, derived from insights obtained from quantum mechanical simulations of small systems. Fully atomistic simulation schemes are essential to elucidate the atomic scale phenomena occurring at the nanometer scale. Defects such as dislocations, their core structure, and mechanisms of their nucleation and interaction with other defects have direct influence on the macroscopic material behavior. The effect of these defects cannot be captured completely through conventional theoretical modeling and computer simulations based on continuum approaches. Therefore, those models must be used in conjunction with atomistic models to characterize materials behavior [3, 4].

While molecular dynamics is very attractive, it is not without its own limitations. One of the major drawbacks of molecular dynamics is associated with time scales. Since the method captures the trajectory of individual atoms and their thermal excitations, the time step size is a few percent of the period of the atomic vibration. In practice, a typical molecular dynamics time step is 1 fs. All current molecular dynamics calculations therefore occur at extremely high strain rates that are generally inaccessible experimentally. The other limitation with molecular dynamics is also one of its strengths, the intrinsic length scale. Atomistic modeling cannot be used to simulate entire systems on the micrometer scale,

because of the limitations of both processing speed and data storage capacity of computers. Even with the largest computers available today, the largest sample that may be simulated efficiently is at a length scale well below the typical grain size of a few hundred nanometers [5], which makes direct comparisons to macroscopic experiments impossible. To overcome this limitation, the field of multi-scale materials modeling have emerged, whereby atomistic modeling is coupled with larger scale continuum models to quantify the performance and behavior of materials across all relevant length and time scales [2].

In spite of these constraints, molecular dynamics is very capable of providing important insights into the behavior of nanoscale materials. The focus of this dissertation is to gain an understanding of the atomic scale behavior of nanocrystalline materials. Due to the fine microstructure of these materials, a fully atomistic treatment is considered to be both realistic and feasible for our research.

Molecular dynamics attempts to simulate the "true" dynamics of atoms while also preserving Boltzmann's statistics [6]. The classical equation of motion can be written as [7]

$$m \frac{d^2 \mathbf{r}_i}{dt^2} = - \frac{\partial V(\{\mathbf{r}_i\})}{\partial \mathbf{r}_i}, \quad (1.1)$$

which is simply the Newton's second law $\mathbf{f}_i = m\mathbf{a}_i$, where $\mathbf{f}_i = -\frac{\partial V(\{\mathbf{r}_i\})}{\partial \mathbf{r}_i}$ is the force on atom i and $\mathbf{a}_i = \frac{d^2 \mathbf{r}_i}{dt^2}$ is its acceleration. Molecular dynamics, at its heart, is simply the numerical integration of equation (1.1).

Time integration of this system of equations captures the trajectory of all atoms in the system with time and permits atomistic simulation of complex problems involving billions of atoms and a simulation period on the order of nanoseconds [8].

The theoretical basis of most atomistic simulation methods is the fundamental law of classical statistical mechanics – Boltzmann's law [9]. This states

that, when the system is in thermal equilibrium at temperature T , the probability density of finding the system near a specific point $\{\mathbf{r}_i, \mathbf{p}_i\}$ in the phase space is $f(\{\mathbf{r}_i, \mathbf{p}_i\})$,

$$f(\{\mathbf{r}_i, \mathbf{p}_i\}) = \frac{1}{Z} \exp \left[-\frac{H(\{\mathbf{r}_i, \mathbf{p}_i\})}{k_B T} \right], \quad (1.2)$$

where

$$Z = \int \prod_{i=1}^N d\mathbf{r}_i d\mathbf{p}_i \exp \left[-\frac{H(\{\mathbf{r}_i, \mathbf{p}_i\})}{k_B T} \right]. \quad (1.3)$$

Here, $k_B = 8.6173 \times 10^{-5}$ eV/K is the Boltzmann's constant. Equation (1.2) is the famous Boltzmann's distribution for classical particles at thermal equilibrium and Z is called the partition function. Z ensures the proper normalization of the probability density f .

An important concept in statistical mechanics is the statistical ensemble of systems. When a very large number of replicas of the system is considered, each with N atoms and described by the same Hamiltonian, each system's state is represented by a point $\{\mathbf{r}_i, \mathbf{p}_i\}$ in the $6N$ -dimensional phase space. An ensemble is the collection of all these replicas. When the replicas are distributed according to Boltzmann's distribution, i.e., equation (1.2), the ensemble is called canonical. Boltzmann's law makes it possible to express macroscopic quantities of the system at thermal equilibrium as a statistical average of microscopic functions over the canonical ensemble. These microscopic functions can be obtained by solving classical equations of motion as in molecular dynamics (MD).

Velocity Verlet Algorithm

Several algorithms for numerical integration of ordinary differential equations are widely used in MD simulations [7]. Among them, the Verlet algorithm is one of the simplest and most stable. One of the variants of Verlet algorithm is the velocity Verlet algorithm which is employed in LAMMPS [10], the MD simulation code used in this work. This numerical integration scheme involves the

following:

$$\mathbf{r}_i(t + \Delta t) = \mathbf{r}_i(t) + \mathbf{v}_i(t) \Delta t + \mathbf{a}_i(t) \frac{\Delta t^2}{2}, \quad (1.4)$$

$$\mathbf{a}_i(t + \Delta t) = -\frac{1}{m} \frac{\partial V(\{\mathbf{r}_i(t + \Delta t)\})}{\partial \mathbf{r}_i(t + \Delta t)}, \text{ and} \quad (1.5)$$

$$\mathbf{v}_i(t + \Delta t) = \mathbf{v}_i(t) + [\mathbf{a}_i(t) + \mathbf{a}_i(t + \Delta t)] \frac{\Delta t}{2}. \quad (1.6)$$

The initial conditions for the velocity Verlet algorithm are $\{r_i(0), v_i(0)\}$.

We note that the Newton's equations of motion conserve the total energy and consequently we require the numerical integration method to also conserve energy. Among the many integrators developed for solving ordinary differential equations, the Verlet algorithms preserve the energy quite well over long time scales [11]. Since the aim of MD is to capture macroscopic long time-scale response, these methods provide an optimal balance between accuracy and computational efficiency for atomistic simulations.

Embedded-Atom Method (EAM) Interatomic Potential

The interatomic potential used for the atomistic modeling in our research work is the embedded-atom method (EAM) potential originally developed by Daw and Baskes[12, 13]. The EAM potential is a simple, computationally efficient, and widely used interatomic potential for metals [14, 7]. The potential energy based on this method is of the form

$$V = \sum_a F(\rho_a) + \frac{1}{2} \sum_a \sum_b \phi(r_{ab}), \quad (1.7)$$

where $\phi(r_{ab})$ is a pairwise potential representing the interaction energy between atom a and its neighbor b [7] and $F(\rho_a)$ is the embedding function for atom a which depends on the electron density at site a due to all its neighbors. The EAM potential typically considers up to second nearest neighbor interactions for

achieving computational efficiency. The EAM potentials used in this work have been fitted to quantum mechanical and experimental data and yield very accurate results for modeling mechanical properties in metals. Hence they have been commonly used by researchers for studying the underlying atomistic deformation mechanisms in these material.

Visualization

The data from MD simulations used for visualizing the defect structures are simply the coordinates of all the atoms of the system. In order to study the deformation mechanisms, it is necessary to filter out the uninteresting atoms that are not associated with the defects directly. These "uninteresting" atoms would be the ones that are still in perfect crystal structure with respect to their surrounding atoms. To identify the location and character of the nucleated defects, and study the nucleation and evolution process of the defects, two visualization techniques, namely centrosymmetry parameter [15] and common neighbor analysis [16], are used in this present work. AtomEye [17] and OVITO [18] are the two visualization software that are used.

1.4 Literature Review

Material behavior is size-scale dependent. Once the characteristic size of materials reaches nanoscale, the mechanical properties change drastically and the classical mechanisms that dictate the deformation of bulk materials cease to hold. This chapter presents a thorough review of the research works that have been conducted over last several years focusing on the unique behaviors exhibited by nanostructured materials. Further enhancement of properties by introducing nanoscale twins inside the grains is one of the major topics of this review. It includes a presentation of the deformation behavior of various fcc nanotwinned

structures from both the experimental and atomistic simulation perspectives, as well as the analytical models developed so far to explain the observed behavior.

1.4.1 Properties of Nanostructured Materials

Nanocrystalline metals are defined as those with a range of grain sizes finer than 100 nm. The many benefits of nanocrystallinity include, *inter alia*, ultra-high yield strength, superior fatigue and wear resistance, and possibly superplastic formability at low temperatures and/or high strain rates. Some of these superior properties are attributed to the fact that the grain boundaries (GBs) arrest the lattice dislocation motion, thereby making plastic deformation difficult at smaller grain sizes, thus exhibiting the Hall-Petch strengthening characteristic of their coarse-grained counterparts.

Synthesis

Nanocrystalline materials can be synthesized either by consolidating small clusters or breaking down the polycrystalline bulk material into crystalline units with dimensions of nanometers. These approaches have been classified into bottom-up and top-down. In the bottom-up approach we have to arrange the nanostructure atom-by-atom, layer-by-layer. In the top-down approach we start with the bulk material and break down the micro-structure into a nanostructure. The principal synthesis methods [4] are: Inert gas condensation [1, 19, 20], Mechanical alloying [21, 22, 23], Electrodeposition [24, 25, 26], Crystallization from amorphous material [27], Severe plastic deformation [28], Cryomilling [29, 30], Plasma synthesis, Chemical vapor deposition, Pulse electron deposition, Sputtering [31], Physical vapor deposition, Spark erosion [32].

A great deal of the early work on mechanical properties of nanocrystalline materials used the inert gas condensation technique [1]. Some of the shortcom-

ings are the possibility of contamination of powders, porosity due to insufficient consolidation, and imperfect bonding between particles, since most of the early work used cold consolidation. Nevertheless, the results obtained using specimens prepared by this method led the foundation of our understanding [19, 33, 20]. Figure 1.1(a) shows the bright field image TEM micrograph of TiO₂ nanoparticles prepared by this technique.

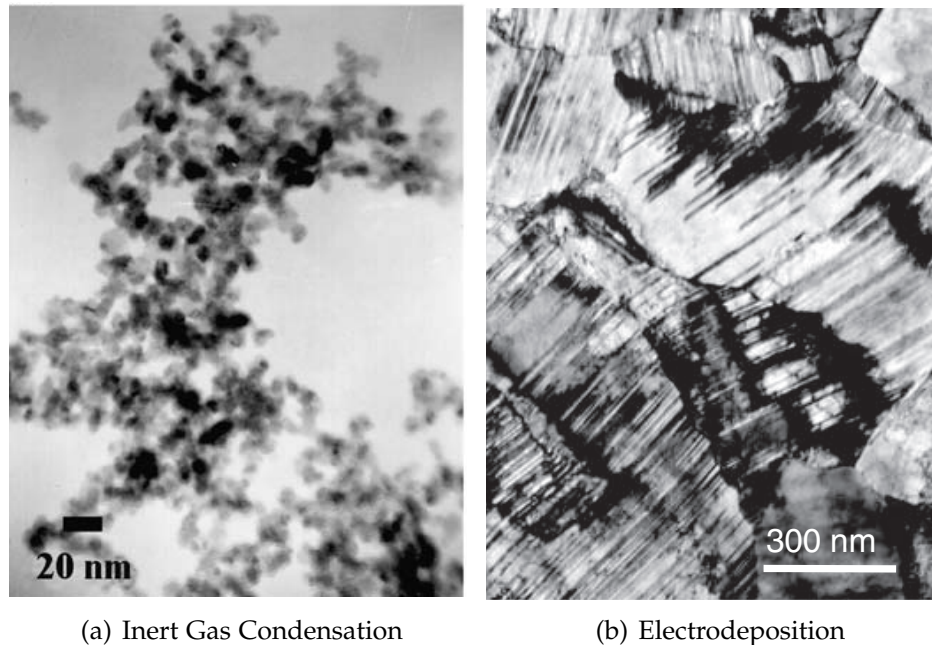


Figure 1.1: (a) TEM micrograph of TiO₂ nanoparticles prepared by inert gas condensation [20]. (b) TEM images of Cu with nanotwins prepared by electrodeposition [34].

The electrodeposition technique has significant advantages over other methods for synthesizing nanocrystalline materials: (1) potential of synthesizing large variety of nanograin materials – pure metals, alloys and composite systems with grain sizes as small as 20 nm, (2) low investment, (3) high production rates, (4) few size and shape limitations, and (5) high probability of transferring this technology to existing electroplating and electroforming industries. Several researchers have used electrodeposition method to produce highly twinned structures for experi-

mental analysis [25, 35, 26]. Figure 1.1(b) shows the TEM image of a nanotwinned Cu prepared by this method.

Strength

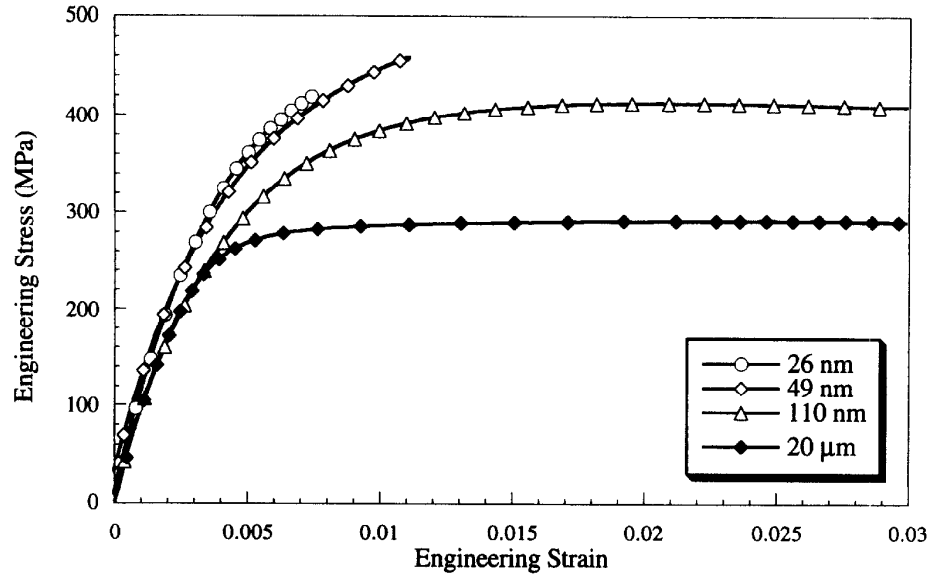


Figure 1.2: Stress-strain plots for Cu for various grain sizes [36].

Grain size is known to have a significant effect on the mechanical behavior of materials, in particular, on the yield stress. The dependence of yield stress on grain size in metals is well established in the conventional polycrystalline range (micrometer and larger sized grains). The yield strength of polycrystalline materials increases with decreasing grain size, as described by the well-known Hall-Petch relation [37, 38, 39, 40]

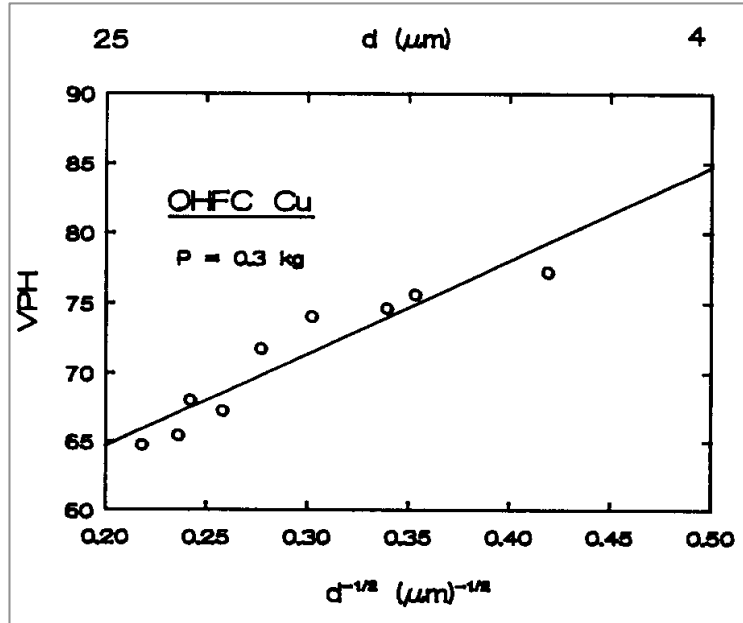
$$\sigma_0 = \sigma_i + kD^{-1/2}, \quad (1.8)$$

where σ_0 is the yield stress, σ_i is the "friction stress" representing the overall resistance of the crystal lattice to dislocation motion, k is the "locking parameter" which measures the relative hardening contribution of the grain boundaries, and D is the grain diameter. The strengthening originates from the fact that grain

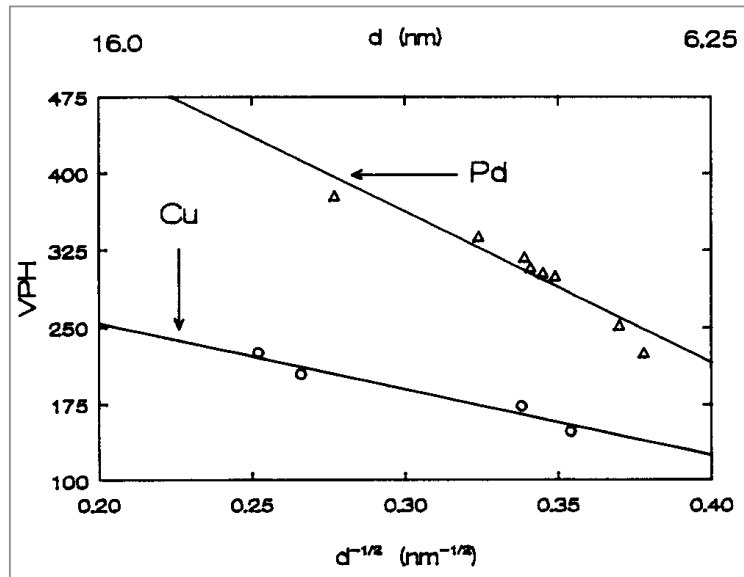
boundaries block the lattice dislocation motion, thereby making plastic deformation more difficult at smaller grain sizes. Weertman and coworkers [36] observed that nanocrystalline Cu and Pd samples were remarkably stronger than their coarse-grained counterpart. The stress-strain plot observed by them has been given in Figure 1.2 which clearly shows an increase in strength as the grain size reduced till 26 nm as predicted by the Hall-Petch relation. We note that as the grain size decreases below 26 nm, an inverse Hall-Petch relation is followed.

Chokshi et al. [41] were the first to report the negative Hall-Petch effect by performing measurements on nanocrystalline Cu and Pd samples. Figure 1.3 presents their results. They attributed this negative trend to diffusional creep in nanocrystalline samples at room temperature analogous to grain-boundary sliding in conventionally-grained samples at high temperature. There have been reports of a similar trend in the Hall-Petch relationship from other sources [42, 43].

As the grain size decreases below a certain critical size, the dominating deformation mechanism changes from lattice dislocation activities to other mechanisms such as grain boundary-related processes, and softening behavior (rather than strengthening) is expected [44, 45]. Such a softening phenomenon has been demonstrated by atomistic simulations, and a critical grain size of maximum strength has been predicted [4, 36]. In pure metals, an impediment to determining the grain size that yields the highest strength is the practical difficulty of obtaining stable nanostructures with extremely small structural domains (on the order of several nanometers). The driving force for growth of nanosized grains in pure metals, originating from the high excess energy of numerous grain boundaries, becomes so large that grain growth may take place easily even at ambient temperature or below.



(a) Coarse-grained Cu



(b) Nanocrystalline Cu and Pd

Figure 1.3: (a) Hall-Petch relation in coarse-grained Cu. (b) Inverse Hall-Petch relation in nanocrystalline Cu and Pd. [41]

Ductility

In the conventional grain size regime, usually a reduction in grain size leads to an increase in ductility. Thus one should expect a ductility increase as the grain

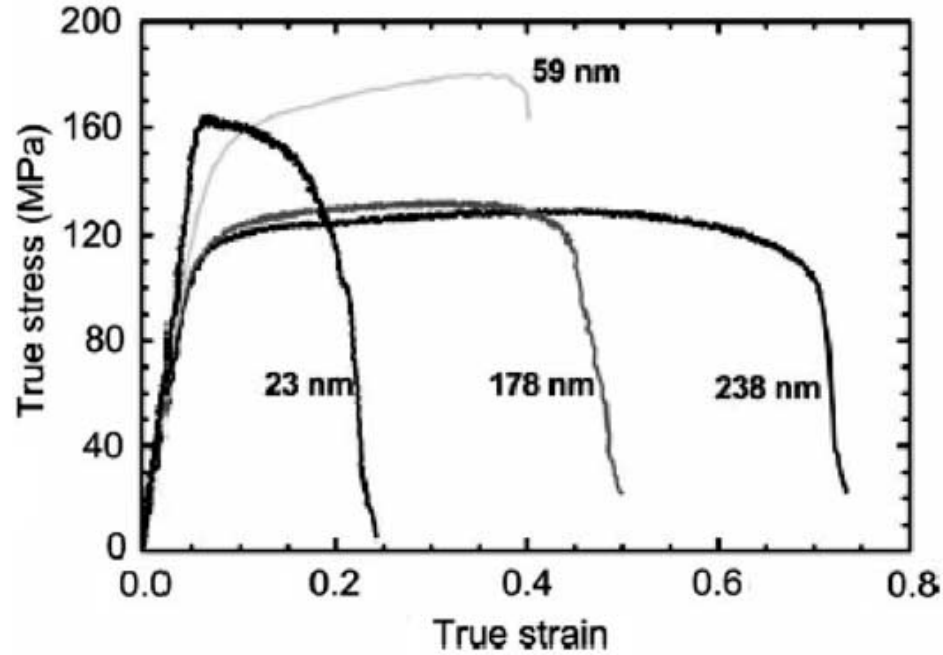


Figure 1.4: Reduction of ductility as grain size is reduced for ball milled Zn tested at a constant strain rate of 10^{-4} - 10^{-3} s^{-1} at room temperature [46].

size is reduced to nanoscale. However, nanocrystalline materials exhibit poor ductility compared to coarse-grained materials [35, 47]. Figure 1.4 shows the mechanical response of nanocrystalline zinc samples with different grain sizes. There is a significant drop in ductility as the grain size goes down from 238 nm to 23 nm. Zhang et al. [46, 48] suggested that the reduction of elongation with the reduction of grain size could be an inherent property of nanocrystalline materials given that there is no porosity and bonding was complete during synthesis. Most nanocrystalline materials experience plastic instability or a concentration of large deformation in one region that results in a crack formation and an early failure or necking in tension [49, 50]. Due to their size nanocrystalline grains fail to efficiently store the dislocations, leading to the low ductility of nc materials [49, 51].

Fracture Response

The greatly enhanced strength that comes about by ultrafine and nanoscale grain refinement has generally been accompanied by losses in ductility and toughness [52, 53]. For example, Karimpoor et al. [54] have shown a 4-fold decrease in impact toughness of nanocrystalline Co with grain sizes in the 18 nm range. Crack growth rates may also be accelerated in nanocrystalline fcc metals due to the "smoother" nature of the crack path [55]). Studies by Li and Ebrahimi [56, 57] and Ovid'ko and coworkers [58, 59], have shown that nanocrystalline metals exhibit a ductile-to-brittle transition with decreasing grain size. A size-effect controlled ductile-brittle transition has is reported by Peng et al. [60] in single crystal Cu nanowires with varying diameters. The tensile results show a transition from ductile to brittle behavior as the diameter decreases to 261 nm. Similar experiments were conducted by Lu et al. [61] on sub-20 nm single crystal nanowires without a direct correlation between the size and the ductile-brittle modes. However, with the help of simulations they described the deformation mechanisms for the two fracture modes. Nano-structured metals, in particular Ti, processed via severe plastic deformation [62], however, show little losses in toughness and may even display somewhat enhanced impact toughness at low temperatures; the grain sizes of these materials are rarely below 60-100 nm, but yet qualify as nanocrystalline. Thus ductility and fracture toughness are an issue with traditional nanostructuring both fcc and bcc metals.

1.4.2 Behavior of Nanotwinned Metals

Intense research on nanotwinned metals began with the work of Lu et al. [25] aimed at designing a novel pulsed electrodeposition technique for nanostructuring in face-centered-cubic (fcc) metals by introduction of coherent twin boundaries (CTBs or TBs) within ultra-fine crystalline metals having a grain size (d) of

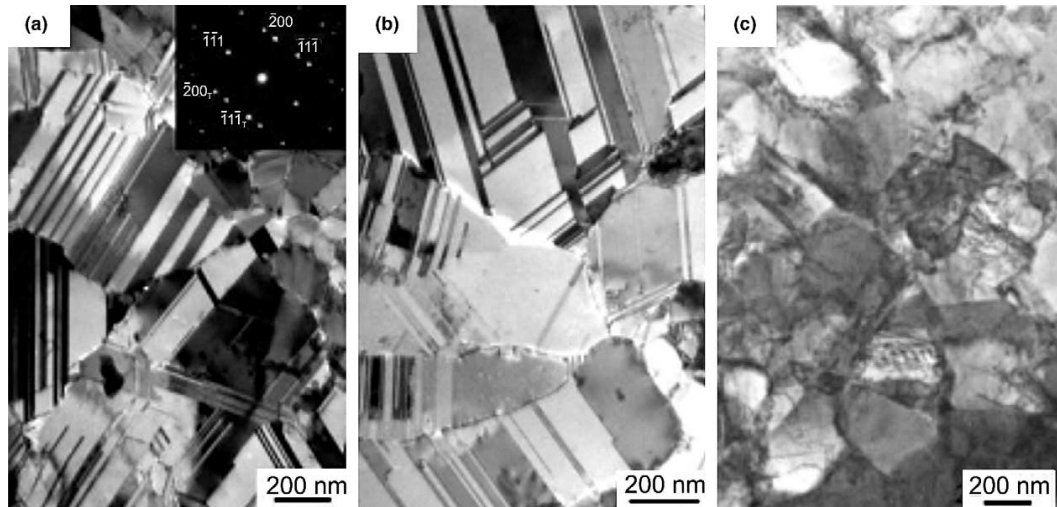


Figure 1.5: TEM microstructure of the as-processed (a) Cu with a higher twin density, (b) Cu with a lower twin density, and (c) ultrafine-crystalline Cu essentially without twins [25].

a few hundred nanometers depicted in Figure 1.5. The twin lamella thickness within each grain ranges between 20-100 nm. These are known as nanotwinned structures and have shown extraordinary properties of ultra-high yield strength as well as ductility, high strain rate sensitivity, and electrical conductivity, excelling their nanocrystalline counterparts, as discussed below. This has stimulated significant interest in nanotwinned fcc metals, and has made them the subject of extensive experimental and theoretical investigations.

Strengthening metals by means of adding twins has been attributed to the glide dislocation interaction with the TBs. Experimental investigations [25, 52, 35, 63] reveal that the presence of twins hinders free dislocation movement and causes dislocation pile-ups at the TBs improving the strength of the nanotwinned sample. When the twin lamellae are thick, a large number of dislocations assemble together in the pile-up and produce a stress concentration at the TBs. Thus, less applied stress is required for slip transmission across the TBs enhancing ductility. However, for thin lamellae, only one or two dislocations may gather at the pile-up and hence, extremely high external stress is needed for dislocation

transmission across the TBs. In this sense, the TBs behave more like the GBs in strengthening of materials at the nanoscale.

Strength, Ductility, and Strain-Rate Sensitivity

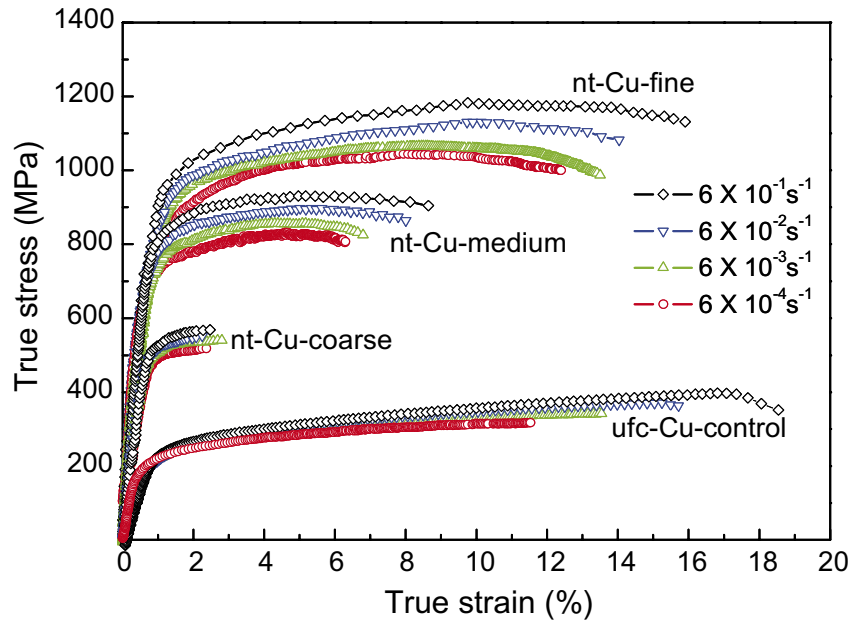


Figure 1.6: Comparison of tensile stress-strain curves for different nanotwinned and ultrafine crystalline Cu specimens tested at various strain-rates and twin-density [64].

Lu and co-workers [63, 35, 34, 65, 66, 67] have demonstrated remarkable strength-ductility properties of Cu containing grains in the size range of 200-500 nm in diameter that contained twins with lamella thickness (λ) in the range of 15-100 nm. This is illustrated in Figure 1.6. An equally intriguing feature of such a nanotwinned fcc metal is its very high sensitivity to strain rate as evidenced in the work of Lu and co-workers [25, 68, 52, 69] that is presented in Figure 1.7.

As noted by Lu et al. [68], the size-dependence of both strength and rate sensitivity appears to scale as $\lambda^{-1/2}$ where λ is the twin lamella thickness, that is, with a Hall-Petch type relation. Moreover, unlike nanocrystalline metals the ductility of nanotwinned fcc Cu remained quite substantial even with twin lamella

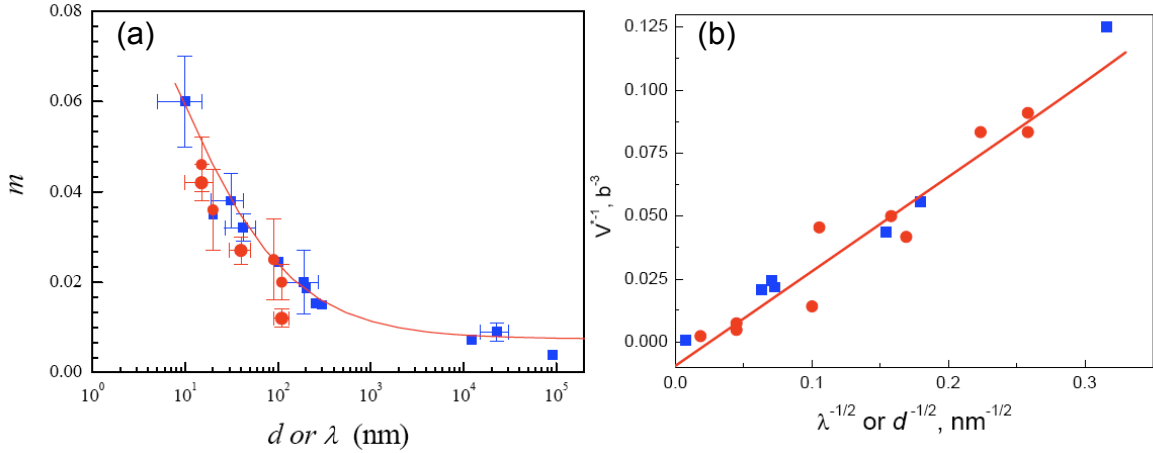


Figure 1.7: Effect of twin lamellar thickness (λ) on (a) rate-sensitivity and (b) activation volume [68].

thickness in the range of 15-20 nm and with flow stress levels in the GPa range evidenced in Figure 1.6. For fcc nanocrystalline metals, as opposed to nanotwinned metals, grain refinement processed through the micrometer to nanometer size scales results in an increase in the strain rate sensitivity index, m , by nearly an order of magnitude, and a concomitant decrease in activation volume, v , by nearly two orders of magnitude [70, 71]. Whereas rate sensitivity is mediated by intra-grain interactions via forest hardening when grain sizes are in the micrometer range [71], it is believed that grain boundary mediated processes control rate dependence in the nanocrystalline range [72]. On this basis, Asaro and Suresh [72] first analyzed the rate dependence and its dependence on nc grain size and demonstrated that rate sensitivity rapidly increased as the grain size decreased much below, say 100 nm. In particular, they predicted activation volumes in the range $5-10b^3$ with grain sizes in the 10-20 nm range, consistent with experiment. In nanotwinned fcc metals, on the other hand, the rate controlling mechanisms appear to be mediated by dislocation-twin interactions [73, 74, 68]. The particular benefits of twin boundaries in contributing strength, strain hardening, and strain rate sensitivity was further explored by Kulkarni et al. [75] via atomistic simu-

lation. The tilt boundaries studied by Kulkarni et al. [75] likewise underwent a coupled normal-shear motion as described by Cahn et al. [76], but tended to lose strength with the first increment of shear unlike twin boundaries that sustained their structure and high strength.

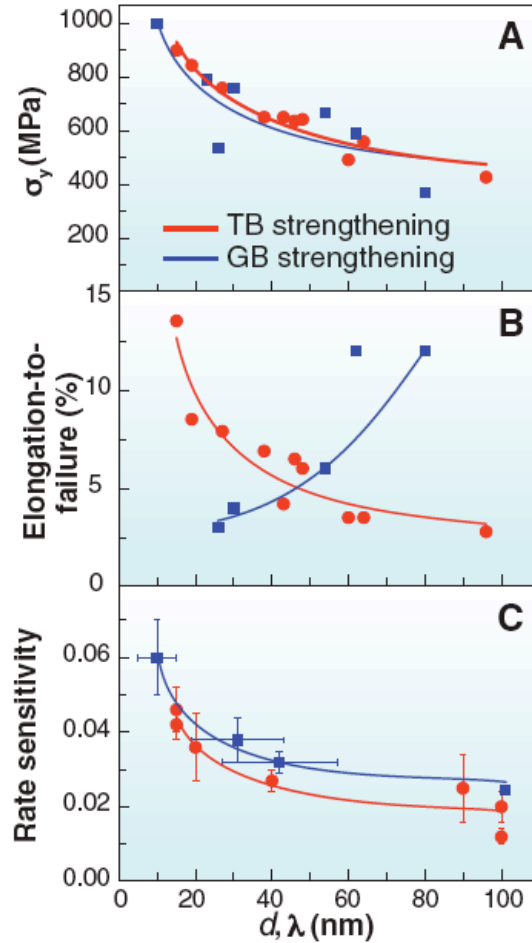


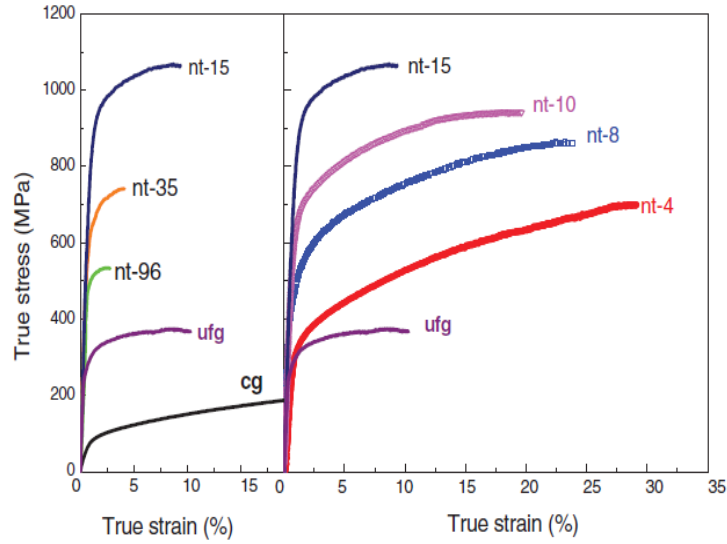
Figure 1.8: The effectiveness of TBs in influencing strength (σ_y , ductility, and rate sensitivity (m) with that of GBs for pure Cu as a function of (λ) or (d) [65].

The numerous studies performed till date provide compelling evidence for the extraordinary properties of nanotwinned metals as compared to their nanocrystalline and fine-grained counterparts [65]. Some of their remarkable properties revealed through extensive experimental studies and mechanistic modeling include ultra-high yield strength, enhanced ductility, and high strain rate sensitivity

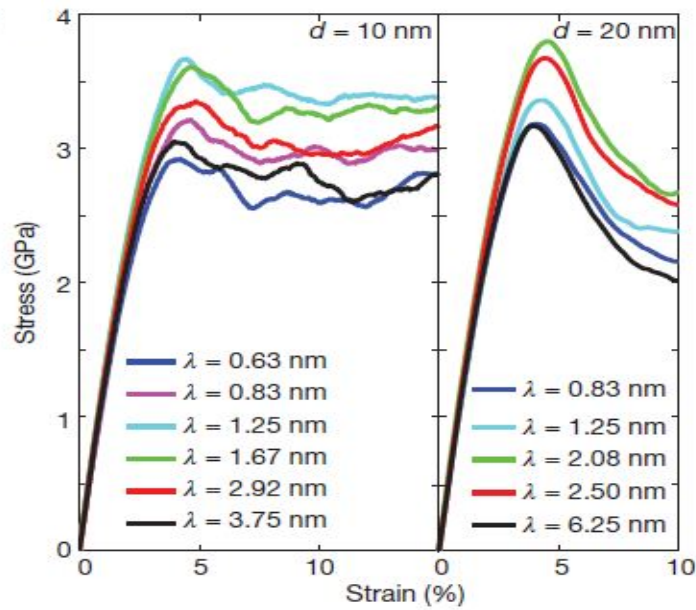
[63, 77, 52, 78, 79, 74, 73] as presented in Figure 1.8, which show the experimental results obtained by Lu et al. [65] that compare the effectiveness of TBs in influencing mechanical properties with that of GBs for pure Cu. The very high shear strength of twin boundaries compared to most grain boundaries and are also effective barriers to dislocation motion. This leads to a strengthening mechanism similar to that of the GBs. However, a unique feature of the coherent twin boundaries is that the twin planes are also slip planes for fcc metals which enables them to accommodate large plastic strains by absorption of dislocations thus enhancing ductility. In addition, recent studies also show that nanotwinned metals are quite stable under deformation.

Critical Twin Spacing - Softening

The extensive research conducted in the last decade on nanotwinned materials brought researchers to the view-point that coherent twin boundaries, per se, indeed provided an optimal motif for imparting high strength and stability. However, in 2009 Lu et al. [34] showed that when the twin lamella thickness is reduced below approximately 15 nm the strength of nanotwinned Cu falls dramatically, thus raising additional intriguing questions regarding the stability of nanotwinned structures. They report that the strength increases with decrease in twin spacing reaching a maximum at the critical spacing of 15 nm, followed by a softening at smaller values that is accompanied by enhanced strain hardening and tensile ductility. This is illustrated in Figure 1.9(a) that compares the stress-strain response of nanotwinned Cu samples with varying twin thickness (in nm) with ultra-fine-grained (grain-size of 500 nm) and coarse-grained Cu (grain-size of 10 μm). The strongest twin thickness originates from a transition in the yielding mechanism from the slip transfer across twin boundaries to the activity of preexisting easy dislocation sources.



(a) Critical twin-thickness for maximum strength



(b) Variation of critical twin-spacing with grain-size

Figure 1.9: (a) Tensile stress-strain curves for nano-twinned Cu samples [34]. (b) Simulated stress-strain curves for nano-twinned Cu with different values of twin-boundary spacing for two grain sizes [80].

This softening behavior of nanotwinned metals at high twin density is also reported by other researchers [81, 82, 80]. While Li and Ghoniem [81] claim 4 nm to be a critical twin thickness for maximum strength in nanotwinned Cu, Shan et

al. [82] propose 15 nm as the critical twin spacing in the pulsed-electrodeposited Cu. But all these work agree on the transition in deformation mechanism to be the primary reason for an optimal twin lamella spacing. Soon after Li et al. [80] showed through simulations that the critical twin-boundary spacing, for nanotwinned fcc metals, depends on grain sizes: the smaller the grain size, the smaller the critical twin-boundary spacing, and the higher the maximum strength of the material. Figure 1.9(b) illustrates their results and shows the critical twin spacing λ for two grain-sizes, d , equal to 10 nm and 20 nm. Recently, Marchenko and Zhang [83] emphasized that the enhancement of the properties is apparently sensitive to the distance between (TB) and grain boundary (GB) and so, it exhibits a maximum at an intermediate distance, while it decreases when TBs are far away or very close to GBs. This implies that the volume between TB and GB plays an important role on the plasticity of nanocrystalline copper. Their result also suggests that in order to strengthen a nanotwinned polycrystalline copper, it is not necessary to grow many coherent twins within one grain by reducing the twin thickness; alternatively, variation of the location of twin distance to grain boundary could achieve a similar strengthening effect within a nanosized grain.

Electrical Conductivity

Nanocrystalline samples with enhanced strength usually exhibit inferior electrical conductivity. However, an interesting observation has been revealed by Lu et al. [63], which shows that the electrical resistivity of nanotwinned Cu sample is much less than that of the nanocrystalline Cu without twins, and very close to that of the coarse-grained Cu specimen over a wide temperature range, as shown in Figure 1.10. The authors argue that conventional strengthening approaches, such as grain boundary refining, solid solution alloying, plastic straining etc., are based on adding various kinds of defects that increase the scattering of conduct-

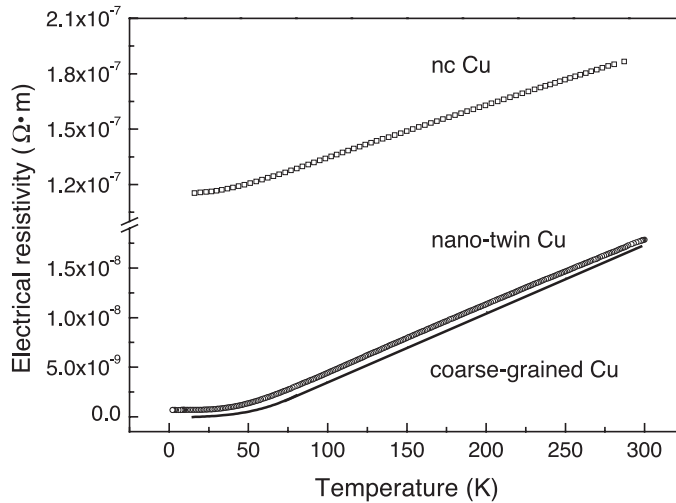


Figure 1.10: Electrical resistivity of various Cu samples as a function of temperature [63].

ing electrons at the defects, thereby making high electrical conductivity and high mechanical strength two contradictory properties of metals. However, the twin boundaries not only act in the same way as the GBs to strengthen the metals (by hindering dislocation movement) but also to minimize the scattering of conducting electrons. Therefore, metals containing high density of TBs exhibit higher strength without significant loss of electrical conductivity [63].

Thermal Stability

Although such structural instability is a critical issue that limits the benefits of nanostructuring, it has remained relatively unaddressed so far in the context of nanotwinned metals, especially at high temperatures. Recent studies by Shute et al. [31] and Saldana et al. [84] show the enhanced stability of nanotwinned Cu at cryogenic and ambient temperatures. The experimental studies of Lu et al. [34] performed at room temperature, also reveal that there exists a critical twin lamella thickness below which there is a decline in the strength (and possibly other properties) of the nanotwinned structure due to twin-twin interactions. These observations have been confirmed by the simulations of Kulkarni and Asaro [85] and

Li et al. [80]. Investigating the mechanical response of coherent twin boundaries at low temperatures, Sansoz and Molinari [86] and Kulkarni et al. [75] observe that coherent twin boundaries exhibit a very high shear strength compared to most grain boundaries, being highly symmetric, low energy interfaces and undergo normal motion coupled to shear. On the other hand, the atomistic study by Li and Ghoniem [81] reveals a competition between deformation twinning and twin migration when the coherent twin boundary is subjected to different kinds of loading at room temperature. Very limited research has been dedicated thus far on the study the high temperature response of twin-boundaries. Zhang et al. [87] report excellent thermal stability of sputtered nanotwinned structures. They attribute the exceptional thermal stability to the low energy of a twin boundary as compared to a high-angle grain boundary.

1.4.3 Fracture in Nanotwinned FCC Metals

As discussed in section 1.4.1, ductility and fracture toughness are an issue with nanocrystalline metals. Recent experimental and computational studies have investigated the failure mechanisms in nanotwinned materials [89, 90, 91, 92, 93, 94, 95]. Several studies reveal an improved fracture resistance of nanotwinned structures due primarily to the interaction of coherent twin boundaries with cracks and dislocations nucleating from crack tips [88, 96, 97, 90, 98]. Twin boundaries imparts a higher fracture toughness to nanotwinned grains as compared to a nanocrystalline grain and reduction in the twin spacing exhibits further increase in the toughness values [88, 97, 96]. Zhou et al. [88] computed the values of fracture toughness by recording the propagation of the crack tip during mode-I loading of the digital samples presented in Figure 1.11. Dislocation activities are highlighted by the white arrows. Figure 1.12 shows the comparison of the fracture toughness curves for three nanocrystalline samples with grain size of 20 nm

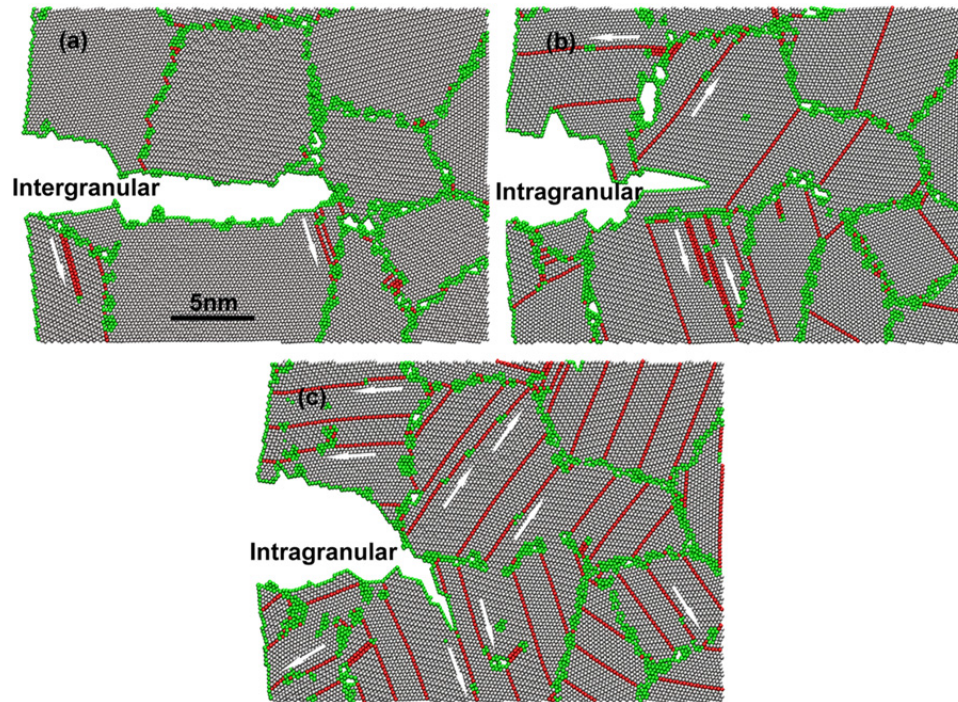


Figure 1.11: Near-crack tip snapshots illustrating crack propagation in (a) twin-free nanocrystalline, twinned samples with λ equal to (b) 5 nm and (c) 2 nm [88].

- untwinned sample (GB-20 nc-20) and twinned samples with twin-width 5 nm (GB-20 nt-5) and 2 nm (GB-20 nt-2).

Qin et al. [53, 99] attribute the enhancement in fracture toughness to the presence of twin bundles which aids in the formation of "deep dimples" [53, 99, 89, 100, 101]; the formation of extended and deep dimples is a process mediated by finite local plastic deformation, i.e., dissipation, which contributes to the total energy of fracture. Molecular dynamics simulations exhibit massive activation of partial dislocations and glide on the CTBs when the crack tip is drawing near, enhancing the fracture resistance of nano-grained copper [97]. In addition, the daughter cracks along the neighboring twin boundaries also provides efficient shielding to the mother crack [97]. Another simulation suggests that the dislocations accumulated along the twin boundaries ahead of the crack tip provide enough strain hardening to result in more uniform plastic deformation, conse-

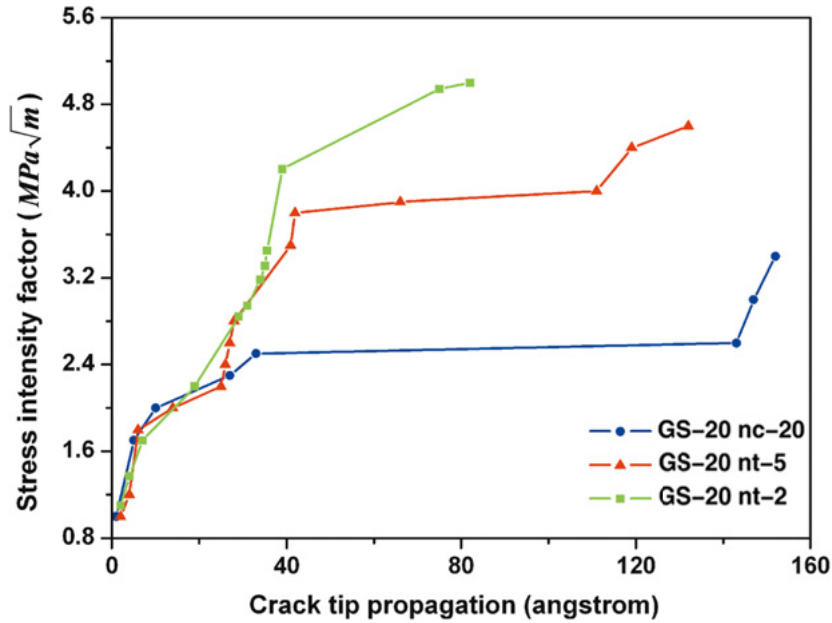


Figure 1.12: Fracture toughness as a function of propagation of the crack tip for the nanocrystalline and nanotwinned samples under mode-I fracture [88, 97].

quently toughening the material [102, 103].

Ductile-to-Brittle Transition

A recent experimental study presents an interesting ductile-to-brittle transition in Au nanowires with decreasing twin spacing on the order of a few angstroms [91]. They attribute it to the transition from heterogeneous dislocation nucleation from free surfaces at large TB spacing to homogeneous nucleation along twin boundaries at small twin lamella which shows "brittle-like" behavior. The experiments conducted by Qu et al. [104] [105] on Cu and Cu-Al alloys reveal that TBs, in Cu and Cu-Al alloys with low Al content, impart strength and resist fatigue cracking along the TB while a decrease in SF energy caused by an increase in Al content, develops fatigue cracks along the TBs making them weaker. The distance of a crack tip from a twin boundary has also been shown to play a role in the brittle versus ductile behavior of nanotwinned metals [93]. A series of HRTEM

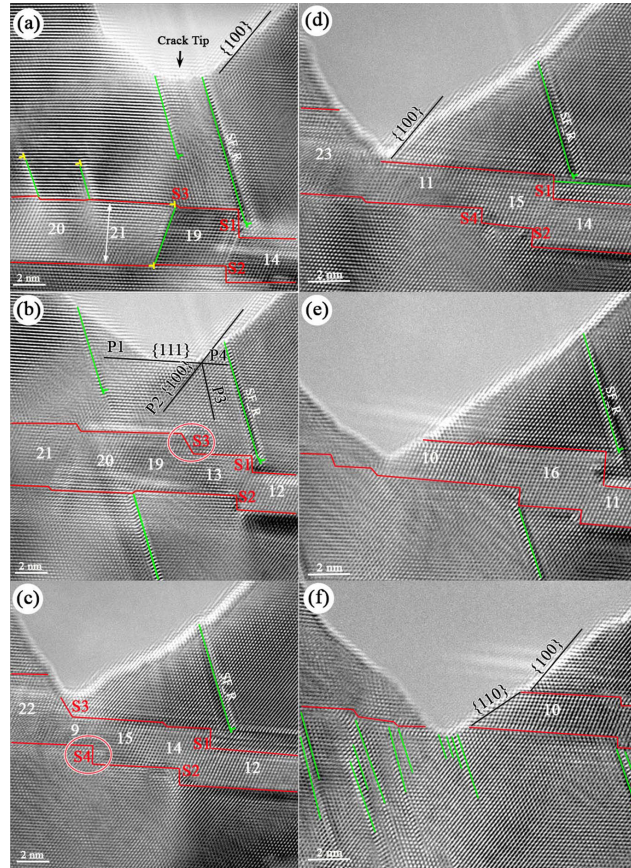


Figure 1.13: In situ HRTEM images during the (a)-(c) crack propagation in the matrix and (d)-(f) penetration of the crack across the twin boundaries. [93].

images in Figure 1.13 reveal the dynamic processes of the crack penetrating the CTBs, which involve plastic deformation modes, crack path deflection and crack tip blunting in a nanotwinned Ag sample.

Another work observes opposite behavior in twinned Cu nanowires with angstrom-scale twins. They observe a brittle-to-ductile transition with decreasing twin spacing and provide a theoretical estimate for the critical twin size to be around 3 nm [92]. According to this work, the twin boundaries are found to have an intrinsic tendency for cleavage in the twin-boundary plane [106] which, for very small twin lamella, is dominated by dislocation nucleation at nearby twin boundaries leading to plastic behavior. Crack cleaving by decohesion along a

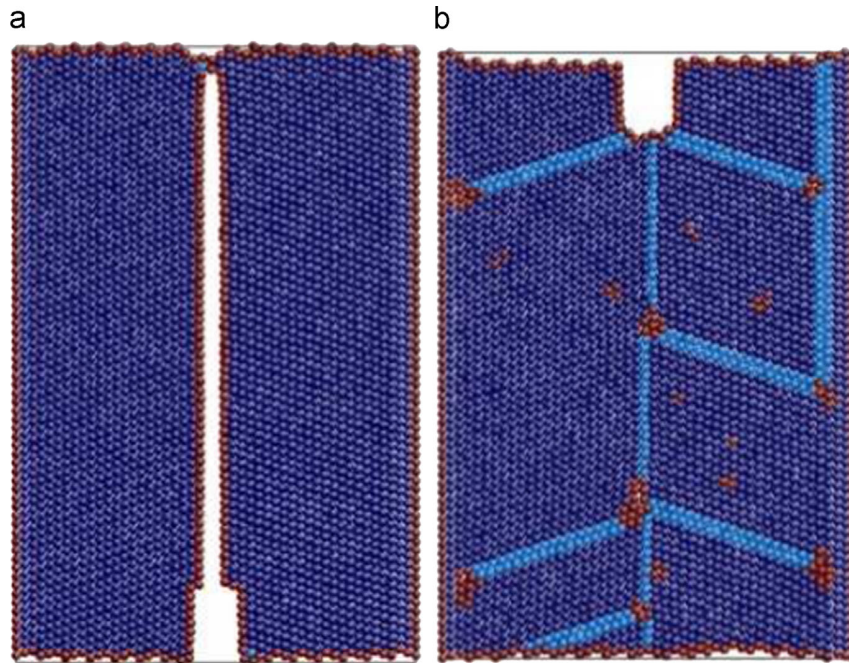


Figure 1.14: Effect of location on the deformation and failure modes in a bicrystal with a pre-existing (a) lower crack (b) upper crack [94].

twin boundary is also observed by Sun et al. [94] recently. They attribute the brittle behavior of the TB to the very small thickness (few lattice spacing) of the twinned nano-film. However, either increasing the thickness by one lattice spacing or changing location of the crack on the thin sample renders it ductile as can be seen in Figure 1.14. These studies taken together suggest that various competing mechanisms, sample size effects, crystallographic orientation and material properties govern the overall fracture response of nanotwinned structures.

CHAPTER 2 ANOMALOUS DEFORMATION

TWINNING IN FCC METALS AT HIGH TEMPERATURES

2.1 Introduction

Nanotwinned structures have shown strong promise as optimal motifs for strength, ductility and grain stability in fcc metals—in sharp contrast to their nano-grained counterparts where gains in strength are disappointingly offset by loss of ductility. However, their high temperature stability has remained relatively unaddressed. As a prelude to addressing the question of the high temperature strength and stability of nanotwinned metals, we investigated the high temperature response of coherent twin boundaries (CTBs) by way of atomistic modeling. To this end, we performed molecular dynamics simulations of shearing of bicrystal specimen containing a CTB. The runs were performed for various fcc metals over a range of temperatures. At low and intermediate temperatures, the twin boundaries exhibit normal motion coupled to shear deformation as expected. However, our simulations at higher temperatures (above 0.5-0.7 T_m), reveal considerable deformation twinning, an occurrence that has not been observed before in fcc metals. Although the origins of this intriguing behavior are not yet clear to us, we discuss a possible conjecture by addressing the following questions: (i) Why is the high temperature response of some fcc metals different? (ii) Why do we observe a transition from twin migration to stacking fault nucleation and subsequent twin formation at high temperatures?

2.2 Methodology

The response of CTBs to shear deformation at a range of temperatures was studied by way of molecular dynamics simulations using LAMMPS [10]. The simulations were performed in the canonical (NVT) ensemble using the Nosé-Hoover thermostat [107]. The effect of the thermal expansion was incorporated by expanding the simulation cell uniformly, prior to the MD simulation, according to the thermal expansion factor at the desired temperature. The thermal expansion was determined a priori through separate MD simulations on a periodic cell in the NPT ensemble. The fcc metals studied herein include Cu, Pd, Ag and Al. Our choice of materials is based on the fact that these four metals differ widely in some of the relevant material parameters thus covering a range of elastic moduli, stacking fault energies as well as twinnability. The embedded atom (EAM) interatomic potentials used in this work are those developed by Liu et al. [108] for Al, Mishin and co-workers for Cu [109] and Ag [110], and Voter and Chen [111] for Pd. Our digital specimen were bicrystals of size $80 \times 80 \times 120 \text{ \AA}$ with a coherent twin boundary (CTB) located at the center and normal to the Z-axis as shown in Figure 2.1. The simulation cells containing 50,176 atoms, were aligned along the $[1\bar{1}0]$, $[11\bar{2}]$ and $[111]$ crystallographic directions with periodic boundary conditions applied in the X- and Y- directions. A few layers of atoms at the top and bottom of the bicrystal were treated as rigid slabs and did not participate in the MD runs. The shear was then applied by displacing the top slab along the $[11\bar{2}]$ direction with a constant velocity of 0.01 \AA ps^{-1} while the bottom slab was held fixed. Thus, the strain rate in our simulations was on the order of 10^8 s^{-1} which is typical for MD calculations. The defect structures were extracted using the centro-symmetry parameter [15] and were visualized using AtomEye [17].

Our idealized bicrystal simulations enable us to understand the interplay between the three modes of deformation associated with the twin or the slip

plane, namely, TB motion, slip, and deformation twinning. We define the three modes as follows. TB motion refers to the apparent motion of the TB normal to its plane, that is, along the $[111]$ direction, when subjected to shear along the $[112]$ direction (Figure 2.5(a)). Slip refers to the formation of an intrinsic stacking fault (Figure 2.5(b), Step I). Deformation twinning refers to the formation of a pair of CTBs under deformation. This is a two step process as illustrated in Figure 2.5(b). The observations of the shear tests are summarized and discussed in the following sections.

2.3 Results

2.3.1 Response at Low and Intermediate Temperatures

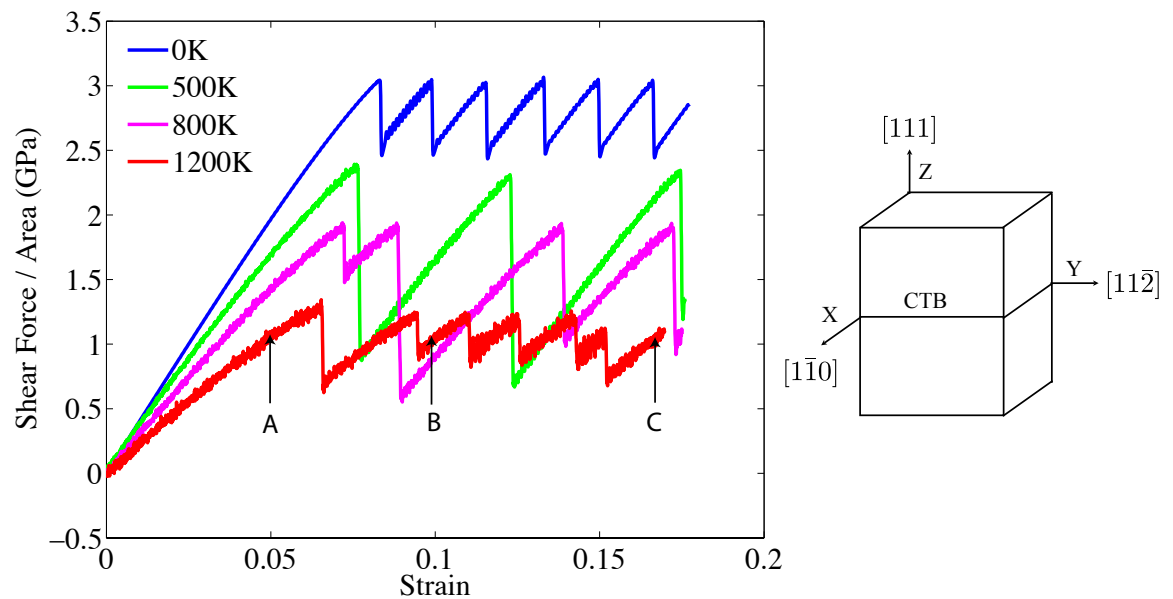


Figure 2.1: Shear stress versus strain plots for Cu bicrystals at various temperatures and the crystallographic orientation of the bicrystals.

The shear stress versus strain curves for Cu bicrystals at different tempera-

tures are plotted in Figure 2.1. The atomic structures at A, B, and C are shown in Figure 2.4. The stress increases linearly as the bicrystal deforms elastically until it reaches a critical value when the CTB moves normal to the twin plane. With increasing temperature, we note an expected trend of softening due to the effect of thermal expansion, and reduced shear strength owing to the increase in the thermal energy content in the system. At 0 K, the CTB exhibits normal motion with a high shear strength of about 3 GPa, as reported by Kulkarni et al. previously [75]. Each drop in the curve corresponds to the motion of the CTB by one lattice plane in the [111] direction. Figure 2.3 shows a sequence of positions of the CTB at strain values of 5% (A) and 18% (B) separated by a distance of about 14 Å or 7 atomic layers. At higher temperatures ranging from 300 K to 800 K, the shear stress displays a similar stick-slip behavior, but with drops much larger than in the 0 K case which correspond to the normal displacement of the CTB through multiple lattice planes simultaneously. This difference is attributed to the thermal fluctuations that provide the excess energy to overcome the activation barrier for twin migration at lower stresses.

These general observations are consistent with earlier MD simulations [76, 86] on a series of symmetrical tilt boundaries over a range of temperatures. We note that at the temperatures considered here, we do not observe any sliding or spontaneous CTB motion, unlike some GBs considered by Cahn et al. [76] which begin to exhibit spontaneous normal motion at about 800 K. In the absence of sliding, the ideal coupling relation between the applied shear and the shear induced by the normal motion can be defined as [76]

$$\kappa = \frac{v_{\parallel}}{v_n}, \quad (2.1)$$

where v_n is the normal velocity and v_{\parallel} is the applied shear velocity. Our calculation of κ for a CTB at different temperatures from 0 K to 800 K confirms the observations of Cahn et al. that κ remains almost constant with temperature and

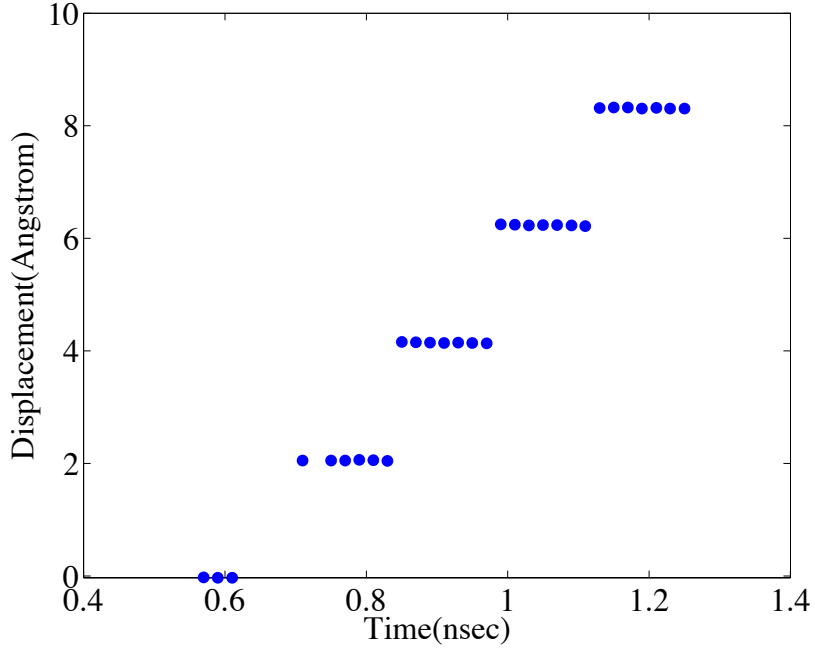


Figure 2.2: The normal displacement of the CTB with time in the shear simulation of a Cu bicrystal at 0 K.

thus behaves like a geometric factor. Figure 2.2 illustrates the CTB displacement during the shear simulation. Using this plot, the κ for CTB motion is found to be about 0.72.

2.3.2 Response at High Temperatures

In this section, we present the results for the shear deformation of Cu bicrystals at temperatures ranging from 800 K to 1200 K ($\sim 0.9 T_m$ with $T_m \sim 1357$ K). As seen in Figure 2.1, the stress versus strain curve at 1200 K also shows a stick-slip behavior although the height of the drops is less uniform. Figure 2.4 illustrates the associated evolution of the bicrystal structure with increasing shear strain. The crystallographic orientation and the initial location of the CTB with respect to the top and bottom surfaces is shown in A. The sequence of images show the process of twinning (B, C) and the eventual annihilation of closely spaced, oppo-

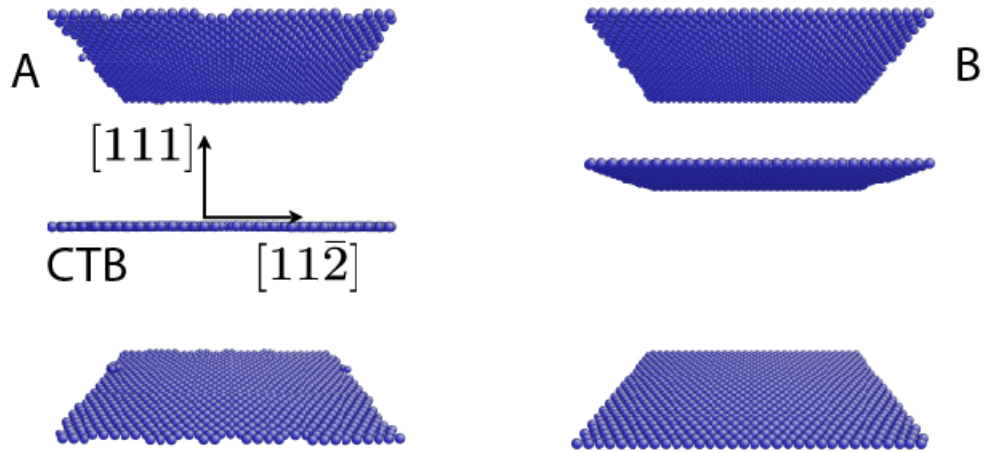


Figure 2.3: The position of the CTB at A) 5% (initial position), and B) 18% shear strain during shear deformation at $T = 0$ K.

sitely oriented CTBs (D). Image B, taken at about 9% strain, shows two additional CTBs separated by a lattice plane in the upper crystal which indicates the formation of the first new twin. Continued deformation twinning is observed with increasing strain as shown in image C which consists of two new pairs of CTBs in the upper crystal. On further shearing, oppositely oriented CTBs (indicated by arrows) move closer and eventually annihilate after approaching a critical separation. This is evident from image D taken at 24% strain. After the annihilation of CTBs, the process of twinning is repeated as the simulation continues.

These results show that there is a transition in the response to shear from coupled CTB motion to formation of twins at higher temperatures. Our simulations at intermediate temperatures predict the transition temperature for Cu to be about $0.65 T_m$ (~ 850 K). No twinning is observed till 800 K. At 900 K, twinning is first observed at 15% strain. With further increase in temperature, twinning becomes predominant with almost negligible normal motion of the original CTB. As mentioned above, closely spaced oppositely-oriented CTBs are found to be more susceptible to normal motion under shear followed by subsequent annihilation.

Using the ABCABC... stacking sequence in the [111] direction fcc metals,

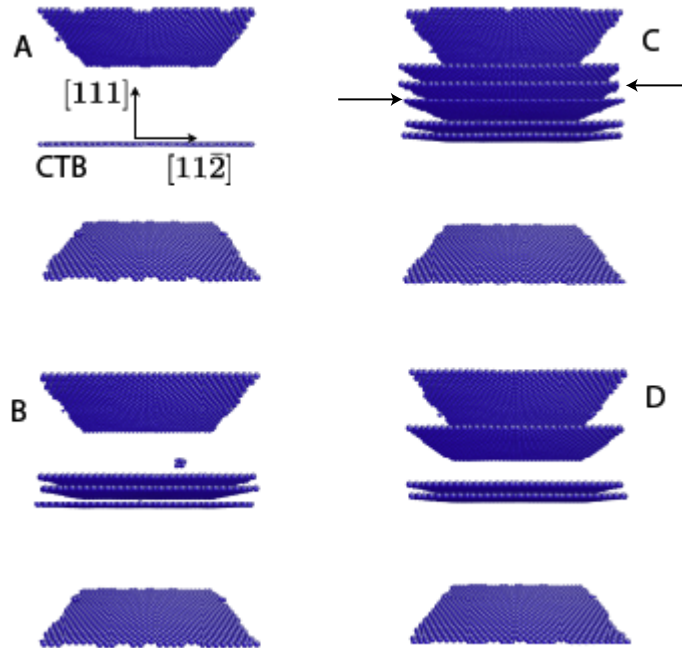


Figure 2.4: The atomic structures at different strains A) 1%, B) 9%, C) 18% D) 24% at $T=1200$ K during shear deformation.

Figure 2.5 depicts the process of normal motion and that of twin formation under shear along the $[11\bar{2}]$ direction. The red line marks a CTB as the stacking sequences along $[111]$ on either side of a red line are in reverse order (or mirror images). The green box shows a two-layer intrinsic stacking fault. Twin migration occurs through the emission of a partial dislocation on a plane adjacent to the existing CTB. Twinning proceeds with the creation of a micro-twin as observed in earlier works [112, 81, 113, 114]. It is a two-step process which involves the nucleation of two partial dislocations on successive $[111]$ planes. The emission of a partial can be depicted by a sliding process. To illustrate this, consider Figure 2.5(a) in which the atomic layer B (immediately above the CTB layer C) slides along $\langle 112 \rangle$ direction to the only other possible position, i.e., A (marked by the dashed arrow). All the layers above shift accordingly. The net result of this sliding is the (apparent) motion of the CTB by one lattice plane as depicted in Figure

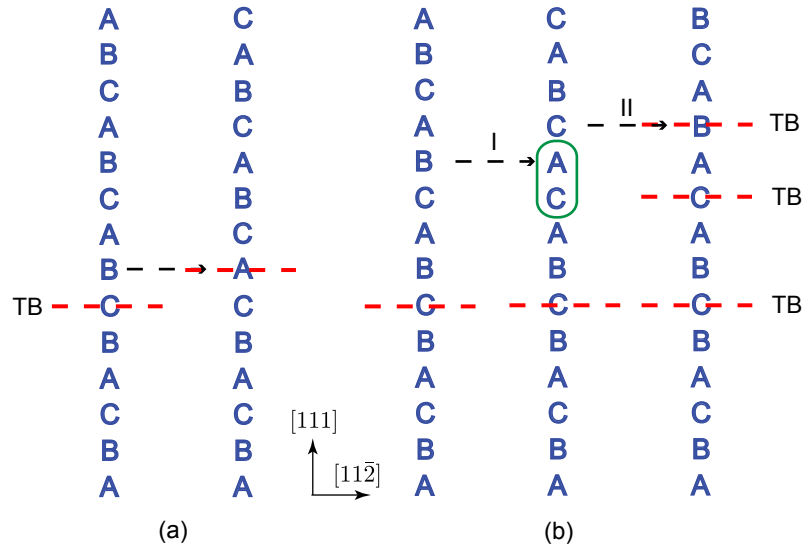


Figure 2.5: Schematic representation of (a) twin motion, and (b) twin formation in a bicrystal with a CTB.

2.5(a). In Figure 2.5(b), this sliding process, when initiated at a random layer in the upper (perfect) crystal, leads to the formation of an intrinsic stacking fault marked by step I. Repeating the sliding process starting one layer above (step II) results in two new CTBs marked by red lines. Both these processes can also be simulated using MD to obtain the generalized planar fault curves and the twin migration curves in order to estimate the associated activation energies for stacking fault nucleation, twin formation and twin migration in different fcc metals [115].

2.3.3 Response of Various FCC Metals

The transition temperature is investigated further by performing similar shear simulations on a few other fcc metals, namely, Pd, Ag and Al. The melting temperatures are taken to be 1828 K for Pd, 1235 K for Ag, and 933 K for Al. Figure 2.6 compares the stress-strain response for these metals at $0.7 T_m$ which corresponds to about 1000 K for Cu, 1300 K for Pd, 900 K for Ag, and 700 K for

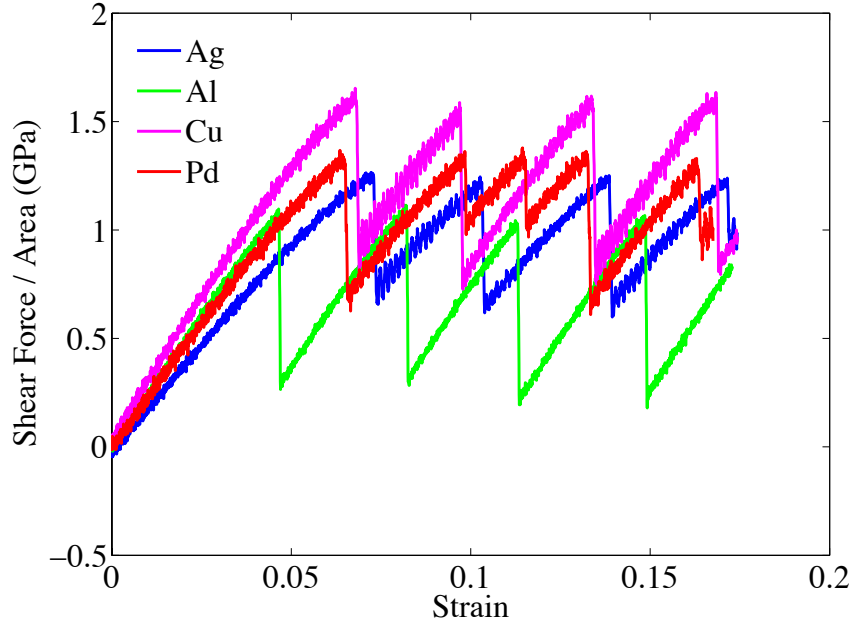


Figure 2.6: Shear stress versus strain plots for bicrystals of Ag, Al, Cu and Pd at $\sim 0.7 T_m$.

Al. The deformation mechanism at low and medium temperatures is found to be coupled normal motion in all the cases. However, the transition to twinning at high temperatures and the associated transition temperature is observed to vary in different metals as described below.

Pd displays a response very similar to that of Cu with a transition temperature of about $0.65 T_m$ (~ 1250 K for Pd). At 1300 K, twinning is first observed at 15% strain which is in agreement with our Cu simulations described earlier. In the case of Ag, twin formation becomes the dominant mode of deformation at a much lower transition temperature of about $0.5 T_m$ (~ 600 K for Ag). In sharp contrast, Al shows no transition at all even up to temperatures as high as $0.86 T_m$ (~ 800 K for Al) and continues to exhibit twin migration. Thus, in Figure 2.6, the load drops correspond to twin migration for Al and deformation twinning for Cu, Pd and Ag.

2.4 Discussion

Our simulations reveal an intriguing temperature dependence of the behavior of twin boundaries which is not expected based on earlier studies. We now seek to analyze these results based on the energetics of these competing mechanisms and discuss a possible conjecture for the anomalous response of twin boundaries at high temperatures by addressing the following questions: (i) Why is the high temperature response of some fcc metals different? (ii) Why do we observe a transition from twin motion (Figure 2.5(a)) to stacking fault nucleation (Step I, Figure 2.5(b)) at high temperatures? (iii) Why does twin formation (Step II, Figure 2.5(b)) occur before or instead of subsequent stacking fault nucleation?

It is well-established through studies on single and polycrystalline metals that dislocation-mediated slip and deformation twinning are the primary mechanisms of deformation at temperatures below which individual atoms become mobile and that the latter is observed at subambient temperatures and/or high strain rates while slip is the dominant deformation mode at higher temperatures [116, 112]. In contrast, our simulations, although performed at high strain rates, show deformation twinning to be the dominant mechanism at high temperatures (above 0.5-0.7 T_m). No twinning is observed at low temperatures where the deformation is governed by TB motion. To the best of the authors' knowledge, this has not been observed before in pure fcc metals although a similar behavior has been observed by Yapici et al. [117] in their experimental study on Ti-6Al-4V. They attribute this unexpected high temperature twinning to the high levels of stress and strains generated during their experiments. Consistent with these studies, our molecular dynamics simulations are also performed under high stresses and high strain rates.

Furthermore, comparing our results with the work of Cahn et al. [76], we note that they only observe normal GB motion and GB sliding at all tempera-

tures. This is due to the fact that they apply the shear on the GB plane in their bicrystal simulations. Thus, the critical stress for GB motion or sliding is reached before the critical resolved shear stress on one of the slip planes can lead to slip or twinning. Since we apply the shear on the [111] plane, our bicrystal simulations involve two competing mechanisms, namely, slip or deformation twinning and twin migration. Thus, our simulations solely compare the shear stress on the slip plane required to nucleate a twin or move an existing twin boundary and its dependence on temperature. This is also a major difference from most prior studies on twinning which were performed on single and polycrystalline specimen and consequently, the major deformation modes were slip, deformation twinning, and ultimately grain-boundary mediated processes at high temperatures. In fact, we believe that a part of the reason for the anomalous deformation twinning we observe is the high shear stresses generated in our idealized simulations in addition to the absence of other high temperature deformation modes which are available in realistic nano- or poly-crystalline specimen.

We first address the different responses of various fcc metals at high temperature based on our earlier work (Kulkarni and Asaro [85]) on dislocation-twin interaction in different fcc metals and that of Bernstein and Tadmor [118] on the twinnability of fcc metals. Both studies use the Peierls framework for dislocation emission from a crack tip introduced by Rice [119]. Based on the predictions of Bernstein and Tadmor [118], the fcc metals can be sorted according to their tendency to twin as

$$\text{Pt} < \text{Al} < \text{Ir} < \text{Au} < \text{Cu} < \text{Pd} < \text{Pb} < \text{Ag}.$$

This trend is in agreement with the increasing values of the dimensionless parameters, β and β_t defined as

$$\beta = 1 - \gamma_{\text{sf}}/\gamma_{\text{us}}; \quad \beta_t = 1 - \gamma_{\text{sf}}/\gamma_{\text{ut}}$$

and computed by Kulkarni and Asaro [85] for Al, Cu, Pd and Ag, where γ_{sf} is the stacking fault energy, γ_{us} is the unstable stacking fault energy, and γ_{ut} is the unstable twinning energy. Taken together with our results for high temperature simulations, we conclude that metals which have greater twinnability (or higher β_t) also exhibit a greater tendency towards deformation twinning at higher temperatures. Consequently, Cu and Pd which have intermediate but similar β_t show similar transition temperatures ($\sim 0.7 T_m$) whereas Ag which has the highest twinnability starts to show profuse deformation twinning at a lower transition temperature ($\sim 0.5 T_m$). In contrast, Al has the lowest twinnability and does not exhibit twinning at any temperature. This response of Al is well-known [118, 112] and usually attributed to its high stacking fault energy, except for recent simulations and experimental observations of deformation twinning in nanocrystalline Al at ambient temperatures [120, 121].

In order to address questions (i) and (ii), we compare our bicrystal simulations with identical shear tests performed on single crystals of the same dimensions [122]. We observe that single crystal Cu exhibits twin formation according to the mechanism illustrated in Figure 2.5(b), with more twinning observed at 1200 K as compared to 0 K. The stress-strain curve shows a saw-tooth behavior. The first peak in the shear stress drops from 3.5 GPa at 0 K to 1.3 GPa at 1200 K ($\sim 0.9 T_m$). For Al, the first peak drops from 2.6 GPa at 0 K to 1.4 GPa at 800 K ($\sim 0.9 T_m$). We note that these peaks correspond to the critical stress for the homogeneous nucleation of an intrinsic stacking fault. The subsequent peaks are smaller than the first and correspond to the stress required to form a twin according to step II in Figure 2.5(b).

Based on our simulations, we are unable to provide a clear rationale for the transition from twin migration to deformation twinning at higher temperatures. However, based on the following reasoning, we conjecture that the transition pos-

sibly occurs due to the difference in the temperature sensitivity of the process of twin migration and that of nucleation of a stacking fault. Figure 2.1 shows the temperature dependence of TB motion in Cu from 0 K to 800 K (the mechanism in the plot for 1200 K is deformation twinning). The shear strength at 0 K is about 3 GPa. Since the peak stress versus temperature follows a linear relation as seen in our simulations, we estimate that the critical stress for TB motion at 1200 K would be about 1.5 GPa. Comparing this with the single crystal results above, we observe that the stress for homogeneous nucleation of a stacking fault is slightly more sensitive to temperature and becomes comparable or even lower than the stress for twin migration at high temperatures (possibly beyond $0.7 T_m$, the estimated transition temperature for Cu). In contrast, for Al, the peak stress for TB motion drops from 1.5 GPa at 0 K to 1 GPa at 800 K, which is always lower than the stress required for stacking fault nucleation, and is consequently preferred at all temperatures. This provides a possible speculation for the transition from twin motion to twin formation for certain fcc metals at higher temperatures.

Table 2.1: Shear moduli, stacking fault energies and the parameter β for various fcc metals [85].

	Al	Pd	Cu	Ag
μ (GPa)	28	41	40	31
γ_{sf} (mJ m ⁻²)	135-200	175-180	35-78	16-22
β	0-0.23	0.32-0.34	0.51-0.83	0.88-0.99
β_t	0.03-0.35	0.49-0.51	0.67-0.85	0.79-0.85

We now attempt to understand why we observe deformation twinning instead of dislocation or stacking fault nucleation only. To this end, we refer to the data compiled by Kulkarni and Asaro (Table 1, [85]) that is presented in Table 2.1 and note that the values of β are very close to those of β_t for metals like Cu, Pd and Ag. In other words, their γ_{us} and γ_{ut} are comparable. This is also indicated by the generalized stacking fault curves obtained by Swygenhoven et al. [115, 112] which show γ_{us} and γ_{ut} to be almost the same for Cu. We plot the

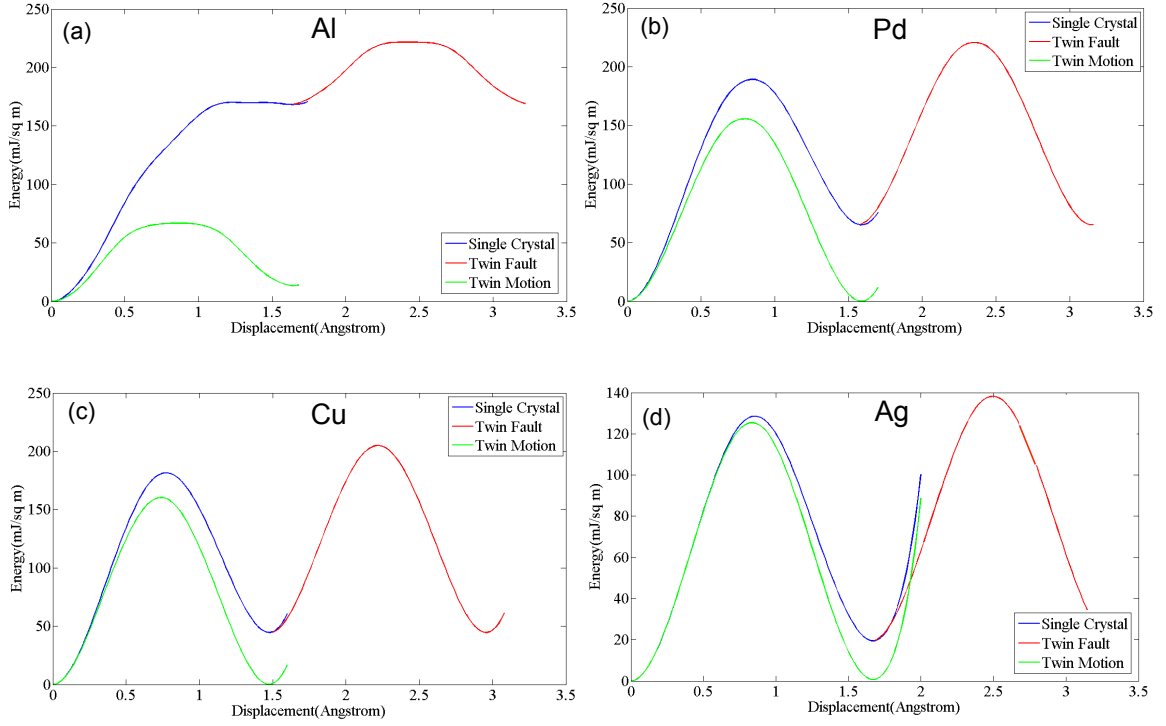


Figure 2.7: Twin migration, stacking-fault formation and twin formation energy curves for (a) Al, (b) Pd, (c) Cu, and (d) Ag.

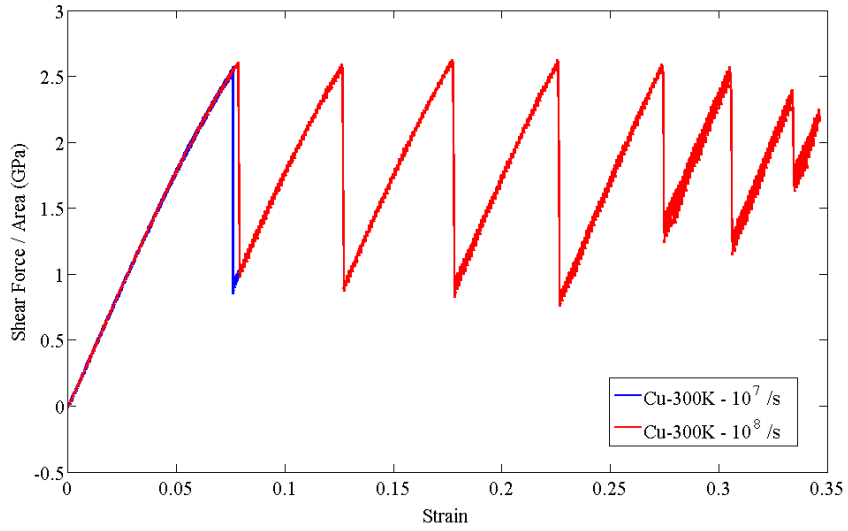
stacking fault formation (blue), twinning fault formation (red), and twin migration (green) energy curves for different fcc metals in Figure 2.7. This implies that after an intrinsic stacking fault is created by homogeneous nucleation in a metal like Cu, it is energetically more favorable to move the two atomic layers of the stacking fault apart to create a deformation twin ($\gamma_{ut}-\gamma_{sf}$) than to create a new stacking fault by homogeneous nucleation (γ_{us}) or to migrate an existing twin (γ_{tm}). Once a new twin is created, the system now has multiple twin boundaries and the subsequent shear deformation depends again on the competition between twin motion and stacking fault nucleation.

2.5 Conclusion

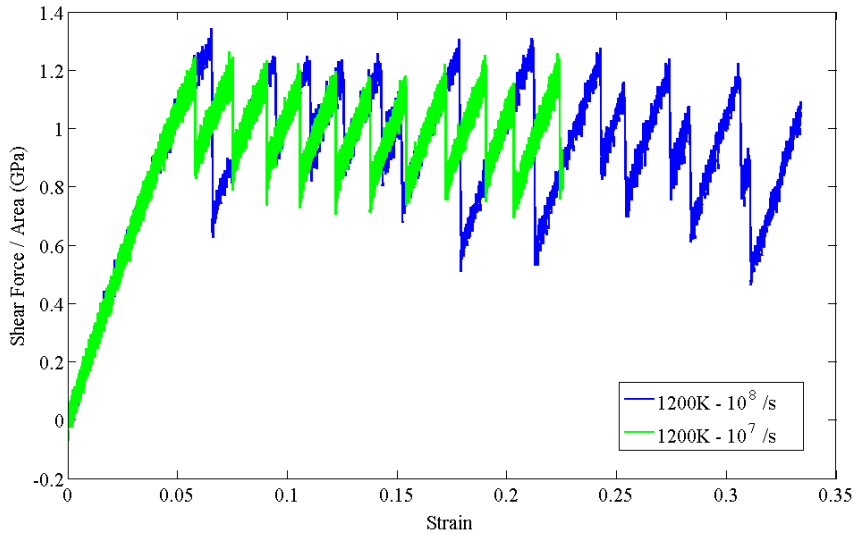
Our simulations reveal an intriguing transition in the behavior of twin bound-

aries in fcc metals at higher temperatures as the mechanism changes from normal motion to deformation twinning. The response is studied for different fcc metals and we conclude that it correlates well with the twinnability of the material. We also speculate that in the metals which exhibit the transition, it occurs due to the different temperature sensitivity of the competing mechanisms, namely, twin migration and homogeneous nucleation of a stacking fault.

We would like to note that finite temperature molecular dynamics simulations are limited by high strain rates. To address this question within the limits of MD, we also performed identical shear simulations for Cu at 300 K and 1200 K at strain rates that vary by a factor of 10, namely 10^8 and 10^7 s⁻¹. Figure 2.8 presents the shear stress versus strain curves for Cu at the two different strain-rates at 300 K and 1200 K. At 1200 K, we do observe a slight strain-rate dependence as twin migration is also observed along with a slightly reduced tendency for twin formation at the slower strain rate as compared to our observation of predominant twinning with no twin migration at the higher strain rate. The corresponding shear strain response is shown in Figure 2.8(b). No noticeable strain-rate dependence is observed at 300 K as depicted in Figure 2.8(a). A complete study of the strain-rate dependence is beyond the scope of MD. Using free-energy minimization methods and calculating the free energy barrier for twin motion and twin formation in fcc metals at finite temperature could provide further insight into the strain-rate dependence of this response of twin boundaries. An interesting direction for future work is to investigate the dependence on load versus displacement controlled conditions. It would also be useful to study the entropic effects of these competing mechanisms based on the recent work of Ryu et al. [123]. Our simulations do indicate that the behavior of nanotwinned metals should depend on the interplay between slip, twin migration and mechanical twinning as the major modes of deformation. They also indicate that CTBs may maintain their stability



(a) 300 K



(b) 1200 K

Figure 2.8: Shear stress versus strain plots at two strain rates, 10^8 and 10^7 s^{-1} , for Cu bicrystals at $T =$ (a) 300 K and (b) 1200 K.

with regards to twin migration even at high temperatures as twinning becomes preferable and the existing CTBs remain unaltered. Thus, it would be quite insightful to further investigate the response of realistic nanotwinned structures at high temperatures based on the competition between these mechanisms as well

as GB mediated processes which become dominant at higher temperatures. Although not discussed in detail as part of this paper, we also observe annihilation of oppositely-oriented CTBs which come closer than a critical separation. Taken together, these responses of twin boundaries observed in our simulations may have an interesting effect on the structural stability of nanotwinned fcc metals and hence, provide possible avenues for future investigations.

CHAPTER 3 ALTERNATING BRITTLE AND DUCTILE RESPONSE OF TWIN BOUNDARIES IN NANOTWINNED STRUCTURES

3.1 Introduction

Molecular dynamics simulations reveal that coherent twin boundaries (CTBs) in nanotwinned structures exhibit alternating intrinsic brittleness and ductility. This is a startling consequence of the directional anisotropy of an atomically sharp crack along a twin boundary that favors cleavage in one direction and dislocation emission from the crack tip in the opposite direction. It is further observed that a blunt crack exhibits ductility in all cases albeit with distinct deformation mechanisms associated with intrinsically brittle and ductile twin boundaries.

In the present work, we investigate the propagation of pre-existing cracks along CTBs to elucidate the fracture response of twin boundaries owing to the effect of the crystallographic orientations in the adjoining twins. We note that although some recent works have observed the intrinsic brittle behavior of CTBs in both experiments and simulations, a systematic study of the geometric constraints that lead to the intrinsically brittle or intrinsically ductile behavior of CTBs has not been reported. Interestingly, our study reveals that CTBs exhibit alternating brittle and ductile behavior that can play a critical role in the twin-spacing dependent transition between brittle and ductile behavior of nanotwinned metals observed recently.

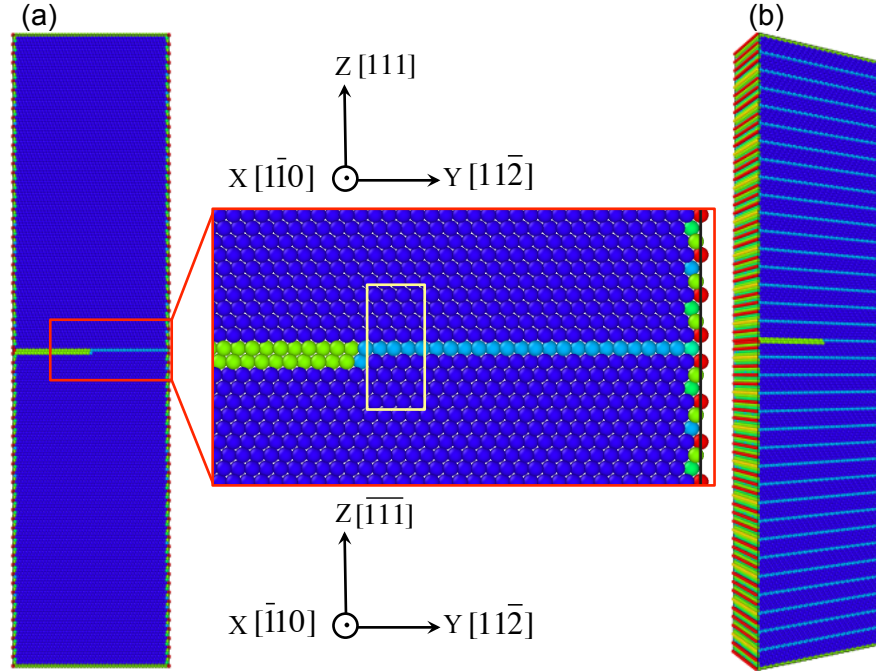


Figure 3.1: Crystallographic orientation of the specimen used in the simulations. Atomistic image of a (a) bicrystalline specimen, (b) nanotwinned specimen with twin spacing of 1.25 nm.

3.2 Methodology

Simulations were performed on bicrystals and nanotwinned specimen using the embedded-atom-method (EAM) potential for copper developed by Mishin et al. [109]. The specimen were aligned along the $[1\bar{1}0]$, $[11\bar{2}]$ and $[111]$ crystallographic directions with periodic boundary conditions applied only in the $[1\bar{1}0]$ direction (Figure 3.1). Each specimen consisted of about 161,000 atoms with dimensions of $4\text{nm} \times 10\text{nm} \times 40\text{nm}$ and contained a pre-existing edge crack. The crack was made atomically sharp by defining a few layers of atoms above and below the CTB as atoms of different types and excluding their interaction. The crack was located on a CTB plane with the crack front along the $[1\bar{1}0]$ direction and its length was half the width of the specimen. As shown in Figure 3.2(a), the grain above the CTB in the bicrystal has the original orientation and is denoted by "M" as the matrix, while the grain below the CTB is denoted by "T" as the

twin or the mirror image. For the sake of convenience, we refer to such a CTB as positive (+). The red lines mark the projections of the $\{111\}$ planes in the matrix and the twin. The dotted lines indicate the extensions of the red lines into the adjoining grain, which are not $\{111\}$ planes due to mirror symmetry about the CTB plane. The atoms on the crack are shown in green, the hcp (CTB) atoms are shown in light blue, and the fcc atoms are shown in dark blue color. In nanotwinned specimen, a CTB with twin orientation above and matrix orientation below is referred to as negative (-) as shown in Figure 3.5. The specimen were generated by incorporating the thermal expansion in the lattice spacing at 300 K and then equilibrating for 50 ps under the NPT ensemble using the Nosé-Hoover thermostat [107]. The tensile loading was applied under the NVT ensemble by moving the top few layers of atoms at a constant velocity of 0.02 Å/ps while keeping the bottom few layers of atoms fixed (see [124] for details). The applied strain rate was $4.75 \times 10^7 \text{ s}^{-1}$. All simulations were performed using LAMMPS [10], and the atomistic structures were visualized based on the centro-symmetry parameter using OVITO [18].

3.3 Results & Discussion

3.3.1 Response of Bicrystal

Figures 3.3(a) and 3.3(b) show the evolution of the cracks along positive and negative $[11\bar{2}]$ directions respectively in a bicrystal under mode I loading. Atoms are displayed according to the centrosymmetry parameter. Atoms in perfect fcc structure are not shown. The left crack is brittle and the right crack is ductile. The comparison of the tensile stress-strain curves for the bicrystals with the left and right cracks are presented in Figure 3.4(a). The red curve shows brittle behavior and corresponds to the crack directed along $[11\bar{2}]$ (left crack). The blue curve

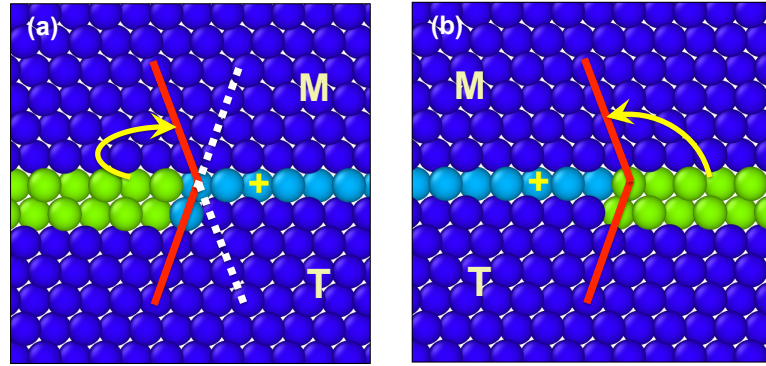


Figure 3.2: (a) Crack located on a + CTB with matrix "M" orientation above and twin "T" orientation below. (b) Crack located on the same + CTB but with its direction reversed.

shows ductile behavior and corresponds to the crack directed along $[\bar{1}\bar{1}2]$ (right crack). The local virial stress-strain curves are also shown in Figure 3.4(b). The local stress was obtained as the virial stress calculated for the region enclosed by the yellow box in Figure 3.1(a). This region has a dimension of $9 \text{ nm} \times 19 \text{ nm}$ in the Y- and Z-directions respectively with about 626 atoms.

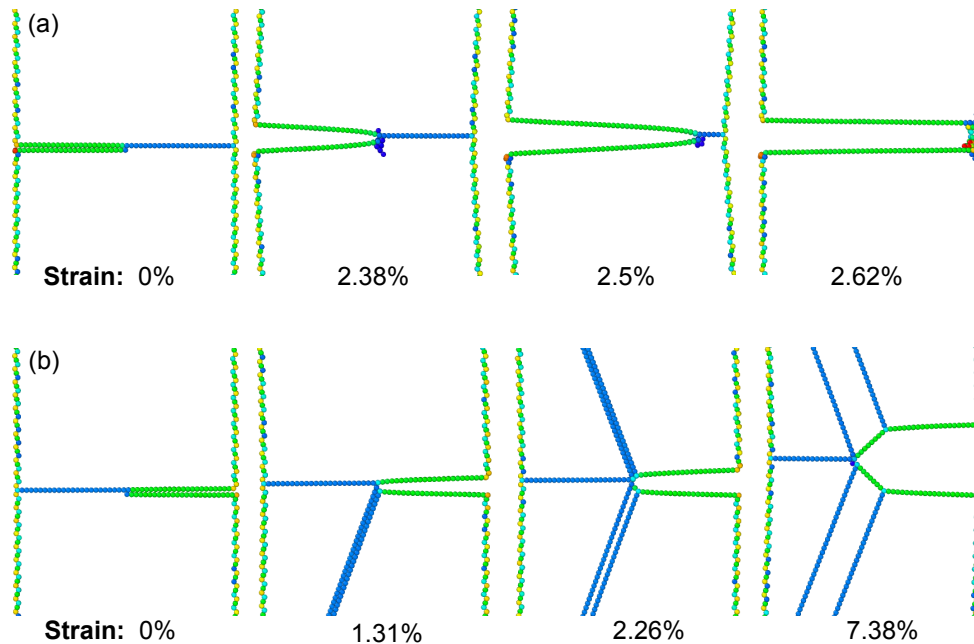
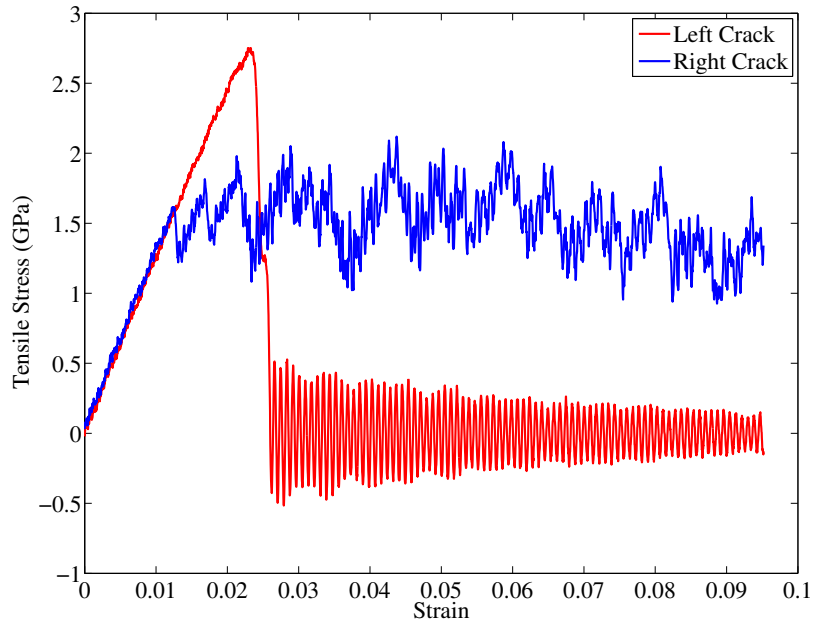


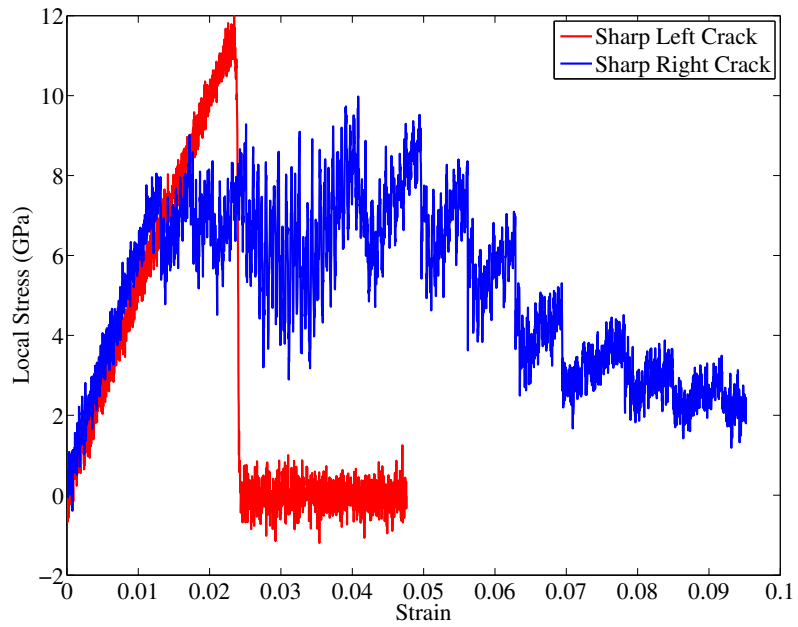
Figure 3.3: Close-up view showing the evolution of the (a) left and (b) right crack along a + CTB in a bicrystal under mode I loading.

When the crack is directed along the positive Y-direction (the crack is on the left), it propagates via cleavage along the CTB. However, when the direction of the crack is reversed (the crack is on the right), it favors dislocation emission from the crack tip. This sharp contrast has been discussed previously by Cheng et al. [106]. They attribute it to the directional anisotropy resulting from the different crystallographic orientation of the matrix and the twin, illustrated in Figure 3.2. The red lines mark the projections of the $\{111\}$ planes in the matrix and the twin. The dotted lines indicate the extensions of the red lines into the adjoining grain, which are no longer $\{111\}$ planes due to mirror reflection about the CTB plane.

Based on the classical model by Rice for dislocation nucleation at a atomically sharp crack tip [119], it is much more energetically favorable to emit partial dislocations in the "forward" direction shown in Figure 3.2(b) than the "backward" direction shown in Figure 3.2(a). This is because the leading partial in the forward direction has a pure edge character, whereas a leading partial in the backward direction would have a large screw component which is energetically less viable under mode I loading [125, 106]. Based on Griffith's theory of fracture, Cheng et al. [106], further show that the energy release rate for brittle cleavage along a CTB in Cu lies between the energetic costs for dislocation nucleation in the backward and forward directions. As a consequence, the left crack shows the formation of an embryonic dislocation at the crack tip that becomes energetically too expensive and the crack ultimately propagates by decohesion (Figure 3.3(a)). The right crack evolves by emitting $\{111\}\langle 112 \rangle$ Shockley partials in the adjacent twins leaving behind stacking fault ribbons, which is the signature of incipient plasticity in ductile fcc metals [126, 89, 94]. After these partials hit the free surface, twinning partial nucleate from the crack tip on adjacent planes causing the crack tip to blunt (Figure 3.3(b)).



(a) System Tensile Stress vs. Strain



(b) Local Virial Stress vs. Strain

Figure 3.4: System and local stress versus strain curves for bicrystal with left and right sharp crack located on a CTB subjected to mode I loading.

Table 3.1: Response of an atomically sharp crack-tip based on the nature of the CTB and the direction of the crack.

CTB Type	Crack Direction	Crack-tip Response
+	$[11\bar{2}]$	Brittle
+	$[\bar{1}12]$	Ductile
-	$[11\bar{2}]$	Ductile
-	$[\bar{1}12]$	Brittle

3.3.2 Response of Nanotwinned Pillar

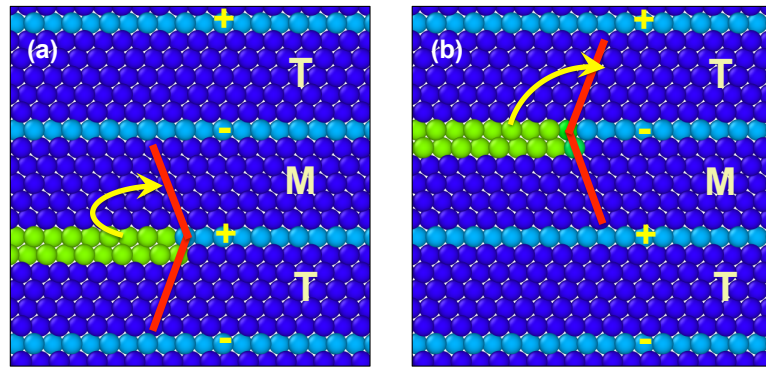


Figure 3.5: (a) Crack located on a + CTB with matrix "M" orientation above and twin "T" orientation below. (b) Crack located on a - CTB with twin "T" orientation above and matrix "M" orientation below.

What would be the implication of such anisotropy on the crack propagation along different CTBs in nanotwinned structures? To address this question, we consider cracks on adjacent CTBs in a nanotwinned specimen and examine the crystal structure at each crack tip. As illustrated in Figure 3.5, the $\{111\}$ slip planes (red lines that mark the projections of the $\{111\}$ planes) are energetically unfavorable when the crack is on a positive CTB and hence we expect the crack to favor decohesion. When the crack is on a negative CTB, the $\{111\}$ planes serve as favored slip planes for the emission of partial dislocations and hence we expect to see plasticity. In order to verify this prediction, we performed simulations on nanotwinned specimen containing multiple parallel CTBs with twin lamella

thickness of about 1.25 nm and a pre-existing crack along a CTB (shown in Figure 3.1(b)). Figure 3.6 shows the evolution of the pre-existing cracks along different CTBs under mode I loading. Atoms are displayed according to the centrosymmetry parameter. Atoms in perfect fcc structure are not shown. As expected, the crack directed along the positive Y-direction on a positive CTB shows brittle propagation similar to the bicrystal case whereas the same crack positioned on an adjacent negative CTB shows dislocation nucleation.

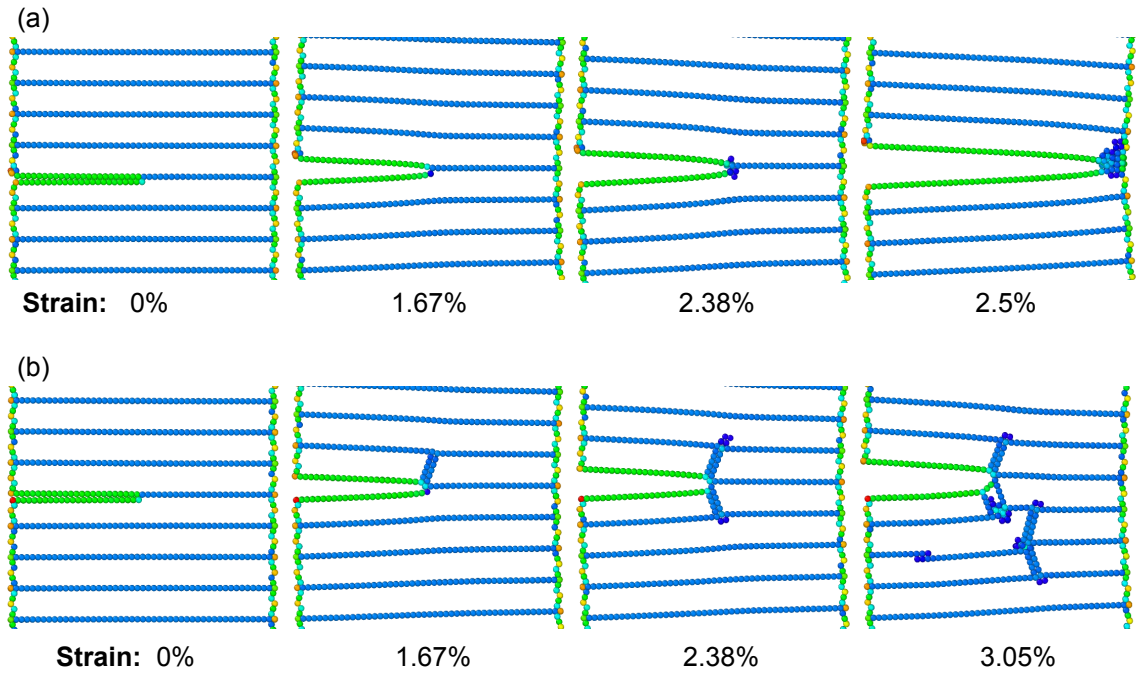


Figure 3.6: Evolution of a left crack along (a) + CTB and (b) - CTB in a nanotwinned specimen under mode I loading.

Figure 3.6 shows that plasticity initiates with the nucleation of the leading Shockley partial from the crack tip leaving behind a stacking fault ribbon. The leading partial impinges upon the adjacent CTB and undergoes the following dislocation reaction which is also illustrated in figures 3.7(c) and 3.7(d),

$$\underbrace{\frac{1}{6}(11\bar{1})[\bar{1}2\bar{1}]}_{\text{leading partial}} = \underbrace{\frac{1}{6}(111)[2\bar{1}\bar{1}]}_{\text{DSC partial}} + \underbrace{\frac{1}{6}(001)[\bar{1}\bar{1}0]}_{\text{stair-rod dislocation}} . \quad (3.1)$$

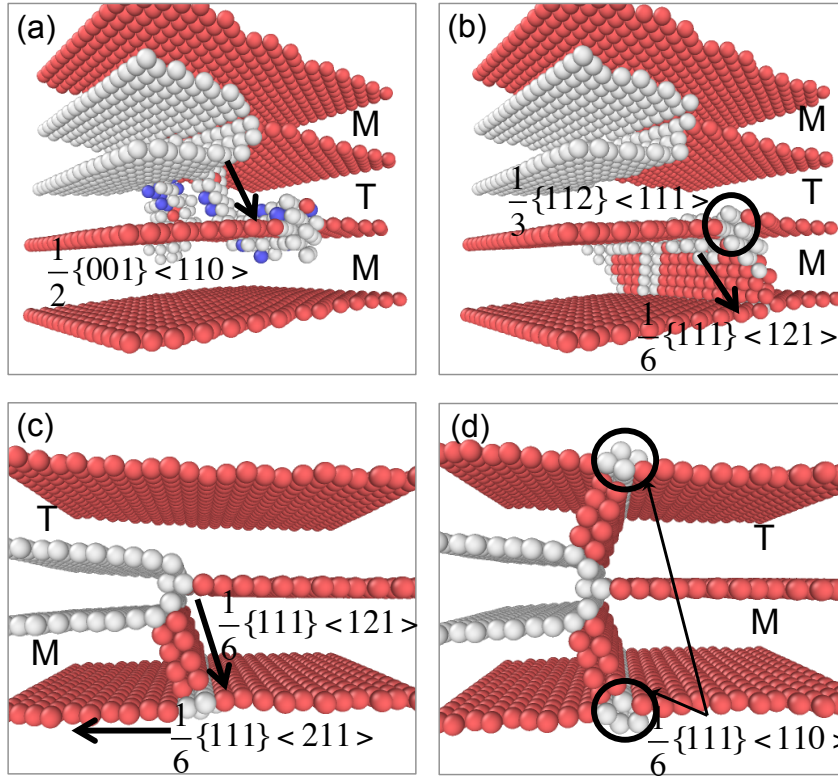


Figure 3.7: Comparison of the dislocation reactions occurring at the (a), (b) brittle crack tip and (c), (d) ductile crack tip.

The dissociation leaves a glissile displacement shift complete (DSC) partial dislocation on the twin plane and a stair-rod dislocation pinned at the twin-slip intersection. This results in the formation of a Lomer-Cottrell lock, which is an important strain hardening mechanism [39, 127], and has been observed in several prior atomistic simulations on nanotwinned metals (see for example [126, 79]). The strain hardening is also evident in the stress-strain curve for the atomically sharp ductile crack along a CTB as seen in Figure 3.11(a) (blue curve). We emphasize that this strain hardening stage is missing in case of the ductile crack in a bicrystal due to the absence of Lomer-Cottrell barriers and the associated dislocation-CTB interactions. The lack of the strain hardening stage can be seen in the strain-strain curve in Figure 3.4(a) (blue curve). The snapshots for the complete deformation under mode I loading of a nanotwinned pillar with the

crack on a positive CTB and a negative CTB are illustrated in figures 3.8 and 3.9 respectively.

Thus, more generally, we conclude that for the same type of CTB (+ or -), a left and right crack will show opposite characteristics. Keeping the crack direction constant, a positive and negative CTB would also show contrasting response. In other words, alternating CTBs exhibit intrinsic brittleness and ductility which is a rather interesting consequence of the directional anisotropy of fracture along CTBs discussed. These results are compiled in Table 3.1. A series of simulations on nanotwinned specimen with varying twin lamella thickness ranging from 0.6 nm to 5 nm were performed to confirm that this behavior of atomically sharp cracks along CTBs was independent of the CTB spacing.

3.3.3 Response of Blunt Cracks

In order to investigate whether this brittle-ductile response of alternate CTBs is not just an artifact of the atomically sharp crack, we also repeated these simulations for a slightly blunt crack that was created by removing a half-layer of atoms. As shown in Figure 3.10, the crack on a negative CTB continues to deform via emission of partial dislocations in the upper and lower grains due to activation of the two favorable slip systems. However, the crack on a positive CTB is no longer perfectly brittle but exhibits dislocation emission, unlike the atomically sharp crack discussed above. Thus, introducing just one atomic layer of blunting, the tendency of the crack-tip transitions from cleavage to emission of dislocations. This is consistent with the observation of Schiøtz et al. [128] that blunting a crack tip even by an atomic layer can cause a brittle-to-ductile transition by making it easier to emit a dislocation and thereby, increasing the microscopic crack tip toughness. Nonetheless, it is evident from the defect structures (Figures 3.10(a) and 3.10(b)) and the distinct stress-strain curves (Figure 3.11) that although both

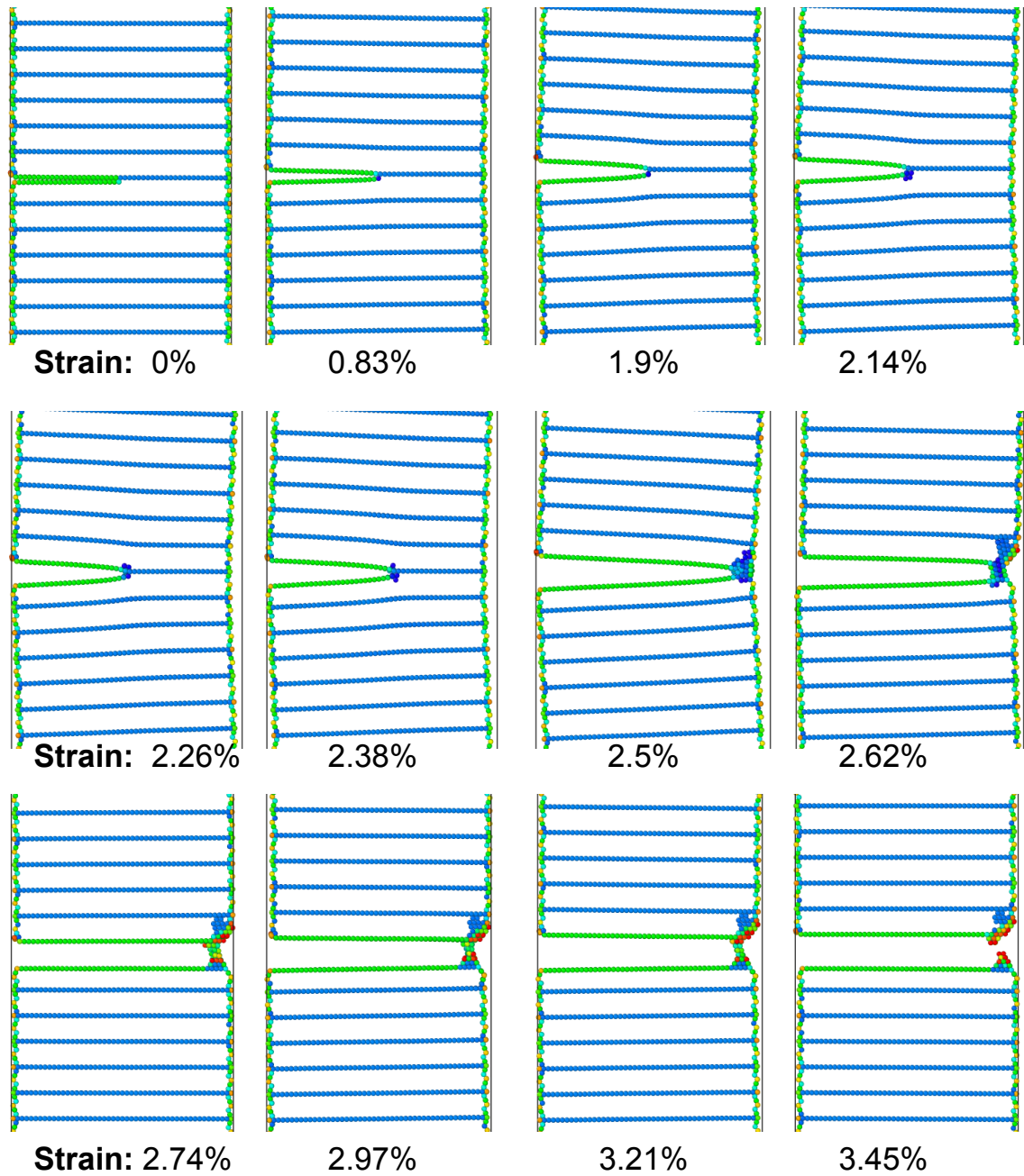


Figure 3.8: Deformation in a nanotwinned specimen, with a crack along a + CTB, under mode I loading.

specimen with blunt cracks exhibit plasticity now, the deformation mechanisms are drastically different. Due to the suppression of the favorable $\{111\}$ slip planes at the intrinsically brittle crack tip, a perfect $\frac{1}{2}(001) \langle \bar{1}\bar{1}0 \rangle$ dislocation is nucleated first. After impinging on the adjacent CTB, it is subsequently transmitted

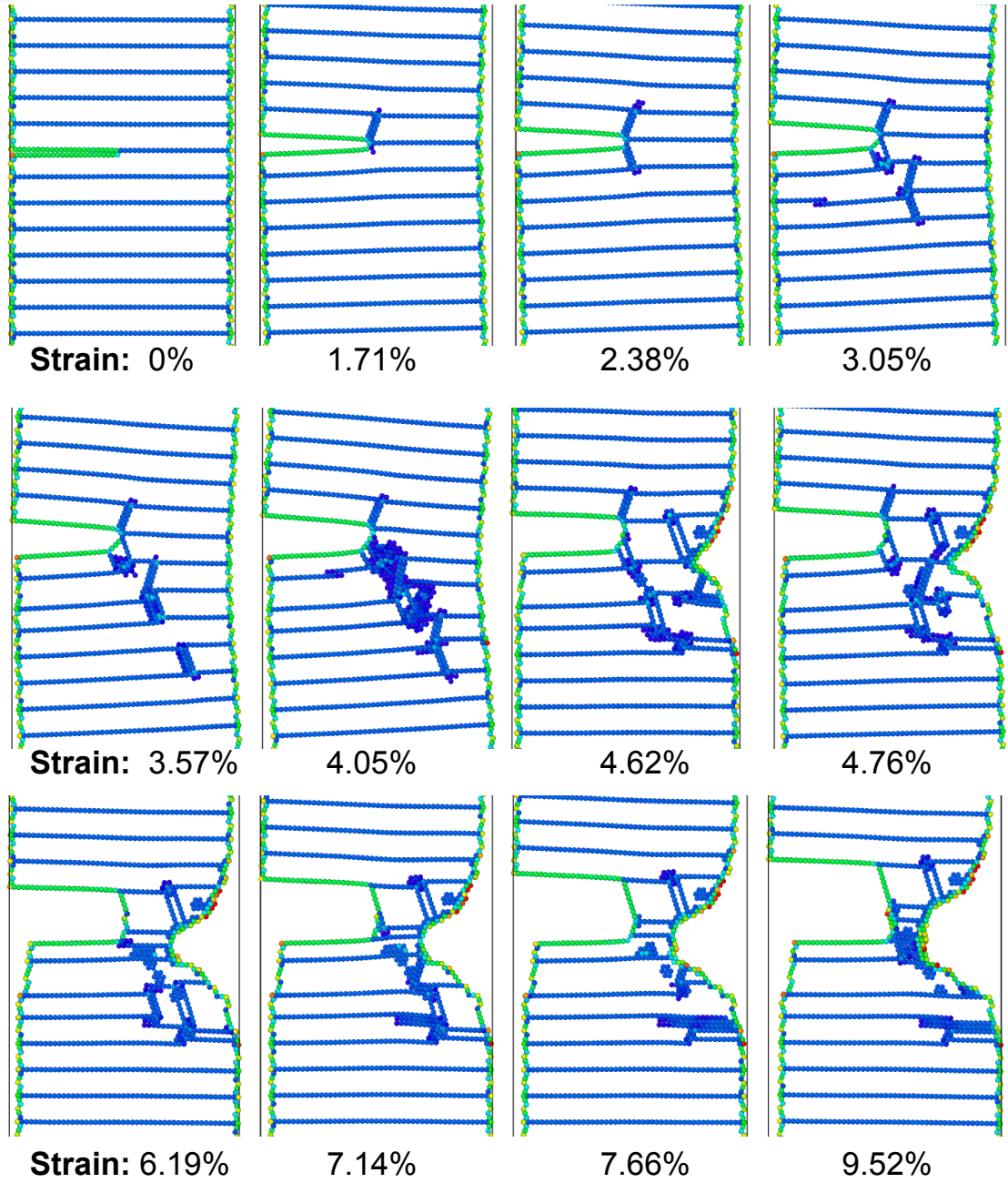


Figure 3.9: Deformation in a nanotwinned specimen, with a crack along a - CTB, under mode I loading.

into the adjacent twin as a Shockley partial, leaving a Frank partial at the twin-slip intersection. The dissociation is shown by the reaction,

$$\underbrace{\frac{1}{2}(001) \langle \bar{1}\bar{1}0 \rangle}_{\text{Unit dislocation}} = \underbrace{\frac{1}{6}(\bar{1}\bar{1}\bar{1}) \langle 1\bar{2}\bar{1} \rangle}_{\text{Shockley partial}} + \underbrace{\frac{1}{3}(112) \langle 11\bar{1} \rangle}_{\text{Frank partial}}, \quad (3.2)$$

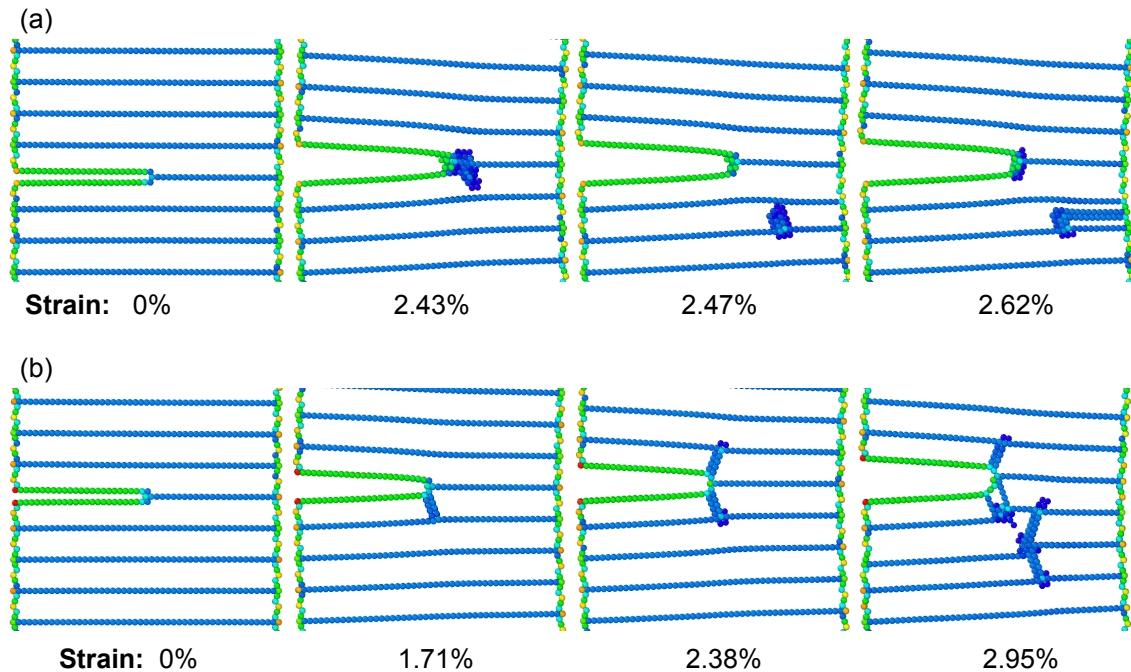
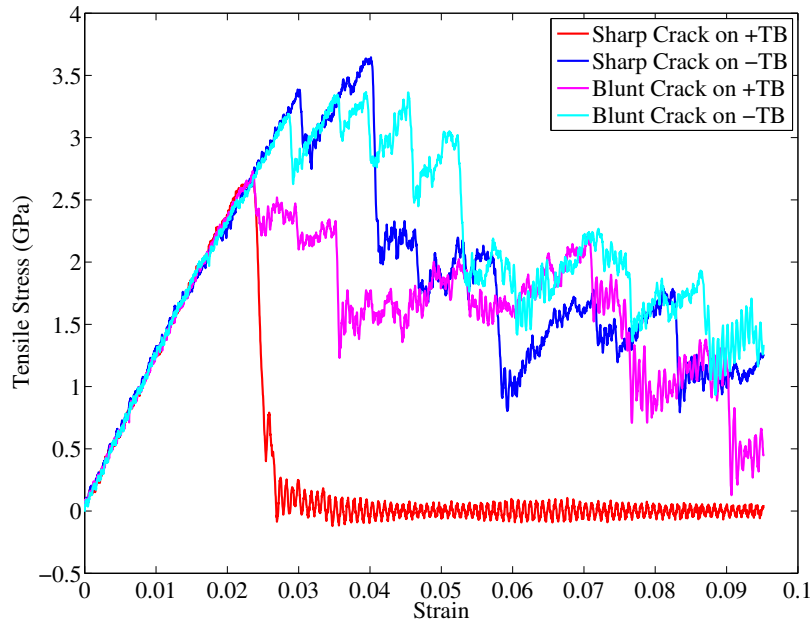


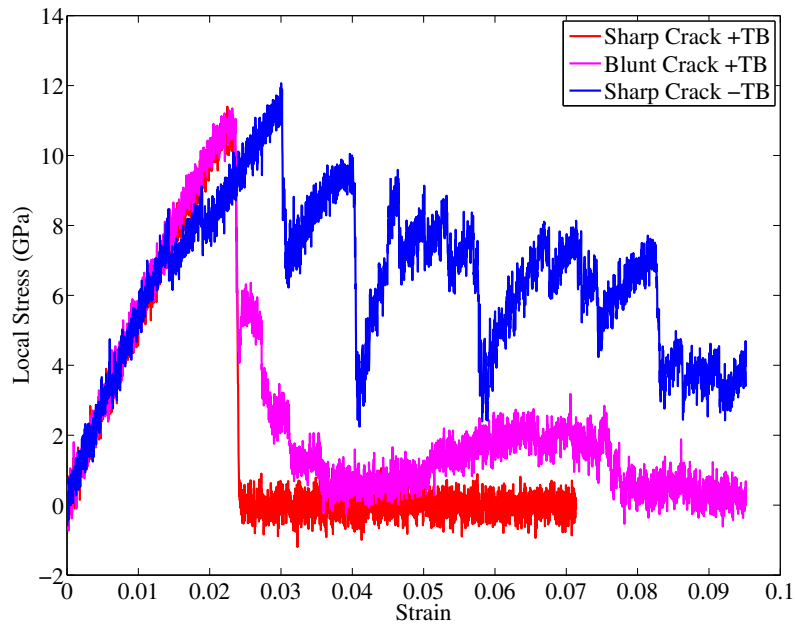
Figure 3.10: Evolution of a blunt crack along a (a) + CTB and (b) - CTB in a nanotwinned specimen under mode I loading. The two cases, although ductile, show very different deformation mechanisms.

which is also discussed in [129, 126, 94], and illustrated in figures 3.7(a) and 3.7(b). In Figure 3.7, the atoms are colored using common neighbor analysis. Red indicates hcp atoms, blue indicates bcc atoms. Figures 3.7 (a) and (b) show a perfect dislocation emitted from the intrinsically brittle crack tip (crack on positive CTB) which is transmitted into the adjacent twin as a Shockley partial, leaving a Frank partial at the twin-slip intersection. Figures 3.7 (c) and (d) show a Shockley partial emitted from the intrinsically ductile crack tip (crack on negative CTB) which interacts with the CTB to form a twin partial (or DSC partial) and a stair-rod dislocation at the twin-slip intersection.

Figure 3.11 reveals that the stress-strain curve for the intrinsically ductile (-) CTB shows significant strain hardening for both sharp as well as blunt cracks with the ultimate strength being about 3.6 GPa. This is almost 1.5 GPa higher than the yield strength for these specimen. It is also interesting to note that



(a) System Tensile Stress vs. Strain



(b) Local Virial Stress vs. Strain

Figure 3.11: System and local stress versus strain curves for nanotwinned specimens with sharp and blunt cracks on positive and negative CTBs.

although the blunting changes the response of the intrinsically brittle (+) CTB from cleavage to dislocation emission, there is hardly any change in the yield strength (about 2.6 GPa) and no strain hardening is observed. Thus, compared to the emission of Shockley partials observed at a typical ductile crack tip, this dislocation nucleation process is still energetically prohibitive and occurs only due to the suppression of the favored slip systems. Figure 3.11(b) compares the evolution of the local stresses for the different cases. As expected, the stress concentration at the crack tip on the intrinsically ductile CTB is quite lower than the intrinsically brittle CTB. Moreover, comparing the local stress at the sharp and blunt crack tip on the intrinsically brittle CTB shows indiscernible difference in stress concentration. Taken together, we conclude that the blunting process leads to a surprisingly modest change in the stress concentration albeit sufficient to drive the brittle-to-ductile transition. Although our blunt crack is still only a single layer thick, the same observation was made by Schiøtz and coworkers [128, 125] on comparing sharp and blunter (wedge-shaped) cracks. The snapshots for the complete deformation under mode I loading of a nanotwinned pillar with a blunt crack on a positive CTB and a negative CTB are illustrated in figures 3.12 and 3.13 respectively.

3.4 Conclusion

In conclusion, our atomistic simulations reveal that CTBs in nanotwinned structures exhibit alternating intrinsic brittleness and intrinsic ductility. Since most of the research till date has focussed on the overall response of nanotwinned specimen, this intriguing characteristic of alternating CTBs has not been addressed before. Despite Cu being a ductile material, the brittle response essentially stems from the suppression of energetically favored slip planes for dislocation emission. This is consistent with earlier predictions that cleavage could

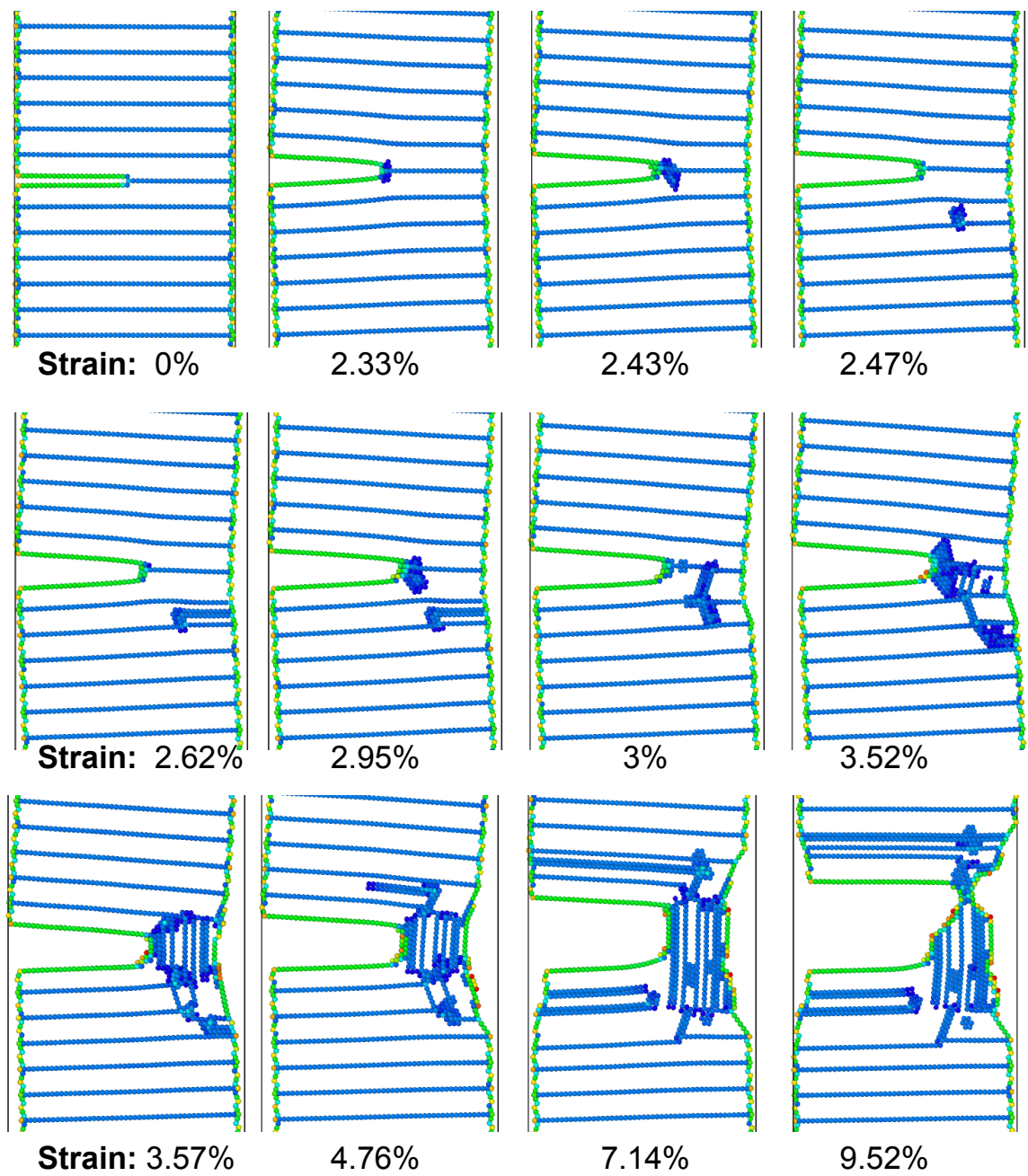


Figure 3.12: Deformation in a nanotwinned specimen, with a left blunt crack along a + CTB in under mode I loading.

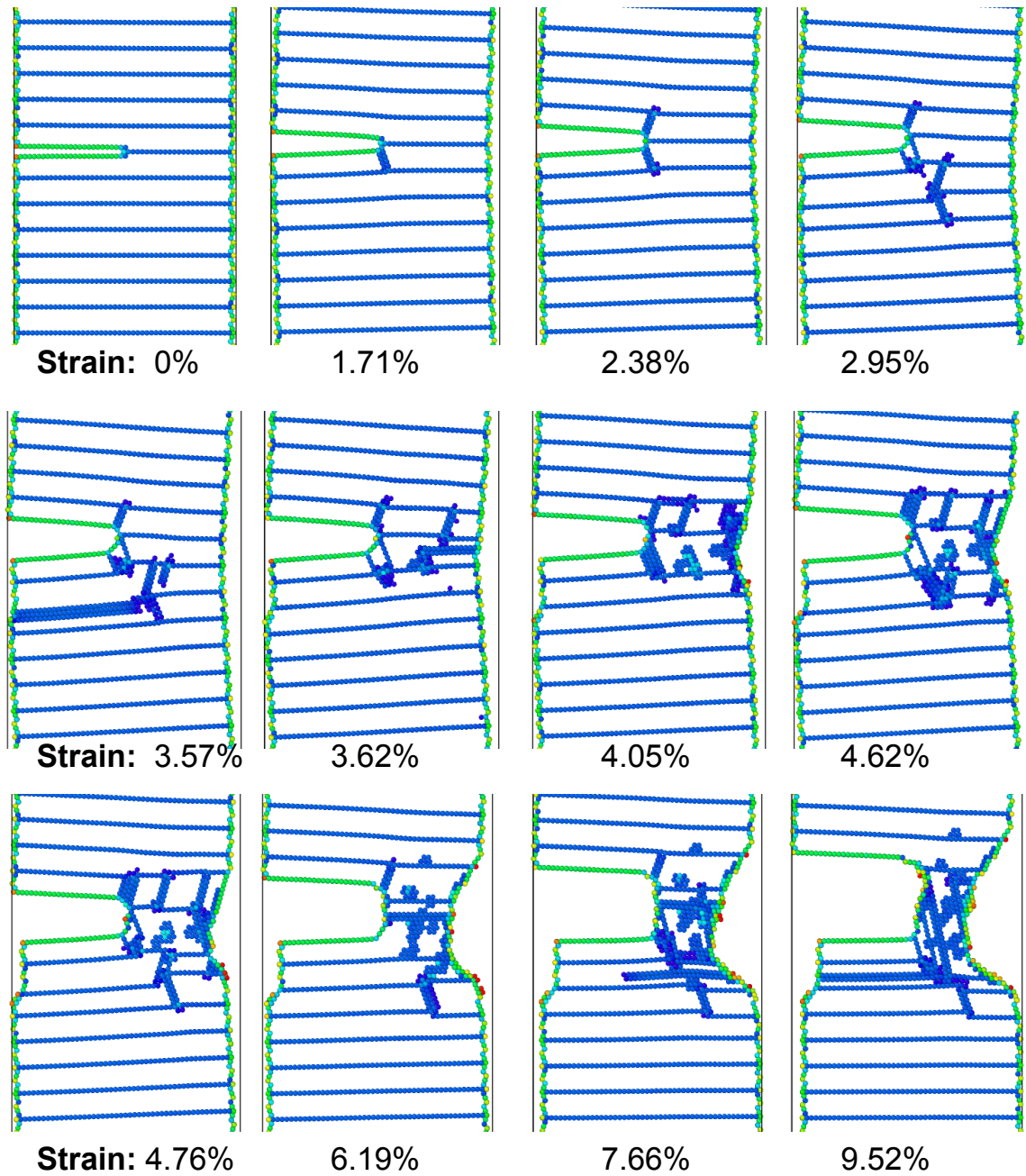


Figure 3.13: Deformation in a nanotwinned specimen, with a left blunt crack along a - CTB in under mode I loading.

be made to occur at interfaces in layered ductile materials via dislocation confinement [130]. Our findings can throw light on some of the intriguing studies of the brittle versus ductile response of nanotwinned metals reported in recent literature. For instance, the brittle fracture observed in the simulations by Jang

et al. (Figure S13 in [92]) for nanotwinned specimen with 4.3 nm TB spacing, is found to occur on a positive CTB which is indeed intrinsically brittle according to our study. Similarly, the intragranular fracture along a CTB observed by Zhou and Qu (Figure 3 in [88]) also occurs along a positive CTB. Our results could also explain the surprising brittle-like deformation of the crack-tip near alternating CTBs observed by Liu et al. [93]. It bears emphasis that the contrasting behavior of alternating CTBs may often be dominated by other competing mechanisms. We have already discussed the transition from brittle cleavage to a more ductile response by blunting a sharp crack on an intrinsically brittle CTB. It was also observed in some of our simulations (not discussed here) that removing the periodicity in the $[1\bar{1}0]$ direction used in this work allows the activation of other $\{111\}$ slip systems, again leading to a ductile response from any crack along a CTB. We have also observed that reducing the length of the crack can also manifest other plasticity mechanisms via dislocation nucleation along the CTB planes, which is in agreement with the simulations of Jang et al. [92]. We performed similar simulations on other fcc metals and found Ag and Pd to exhibit the same alternating response as Cu. However, Al did not show brittle cleavage even from atomically sharp cracks as Shockley partials were emitted from neighboring CTB resulting in a ductile deformation. Thus, it would be insightful to carry out further examination of the crack response of different fcc metals such as Al, Au, Ag, and Pd to cover a range of stacking fault energies, surface energies, and unstable stacking fault energies. These parameters are known to play a vital role in crack propagation versus dislocation emission from a crack tip [106, 119]. Thus, the effects of the crack-length, material properties, and temperature are important avenues that warrant further experimental and computational investigations.

CHAPTER 4 CRACK PROPAGATION IN TWINNED NANOPILLARS

4.1 Introduction

In this chapter, we investigate the role of twin boundaries and the effect of twin-spacing (λ), and sample thickness on the deformation mechanisms of twinned nanopillars with a pre-existing crack in fcc metals. An interesting observation is that the plasticity around the crack tip is restricted within just two twin lamellae in the case of all twinned nanopillars containing four coherent twin boundaries (TB) studied here. Along with the expected size and twin-spacing effects, we also observe a critical aspect ratio below which the plastic deformation is no longer localized within two twin lamella.

4.2 Methodology

Molecular dynamics was used to simulate the tensile test performed at 50 K on copper samples, with and without coherent twin boundaries (CTB), containing a pre-existing crack. The samples were aligned along the $[1\bar{1}0]$, $[11\bar{2}]$ and $[111]$ crystallographic directions with periodic boundary conditions applied only in the X- direction. For both the single crystals as well as the nanotwinned pillars, four thicknesses (7 nm, 10 nm, 14 nm and 18 nm) in the Y-direction were tested, while the thickness in the X-direction was held constant at 4 nm. An aspect ratio ($\frac{height_{z-dir}}{thickness_{y-dir}}$) of 4 was maintained for all the specimens. This value of aspect ratio ensured that the fixed boundaries did not affect the dislocation activity or lead to spurious hardening effects especially in the single crystals. The different sizes of the samples are 4 nm \times 7 nm \times 28 nm, 4 nm \times 10 nm \times 40 nm, 4 nm \times 14 nm \times 56 nm

and $4 \text{ nm} \times 18 \text{ nm} \times 72 \text{ nm}$.

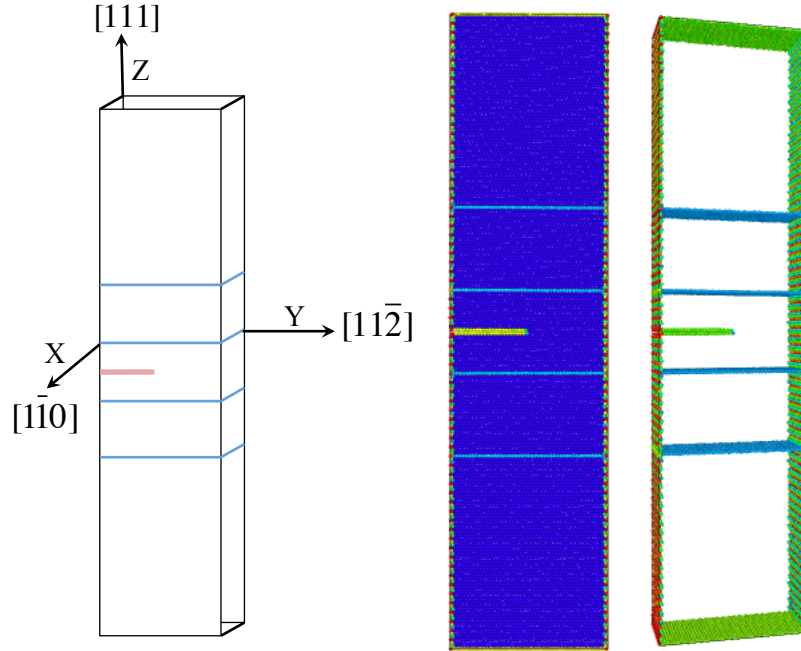


Figure 4.1: (a) Crystallographic orientation of a nanopillar. Ovito images show (b) all atoms (b) atoms with non-zero centrosymmetry.

All the samples had an atomically sharp edge crack along the Y-direction positioned at the center of the sample as shown in Figure 4.1. The pre-existing crack length was always maintained at half the thickness of the specimen at the beginning of the simulation. Twinned nanopillars consisting of three different values of twin boundary spacings (λ), specifically, 8 nm, 6 nm, and 4 nm, were used for comparison. Each nanopillar contained four coherent twin boundaries (CTB) near the center of the specimen, two above and two below the crack.

Tensile simulation under mode I loading was performed by applying a constant velocity to a few atomic layers at the top while a few layers at the bottom were held fixed. We note that this resulted in a slight difference in the strain rates ranging from 7×10^7 /sec to 2×10^7 /sec for sample thickness 7 nm and 18 nm respectively. The tensile loading for all the samples was simulated for 2 nanoseconds (ns), which rendered a different end value of strain for different

thicknesses - 14.9% for 7 nm, 9.6% for 10 nm, 7.2% for 14 nm and 6.3% for 18 nm. The embedded atom method (EAM) interatomic potentials used in this work were those developed by Mishin and co-workers for Cu [109] and Ag [110] and Liu et al. [108] for Al. OVITO [18] was used for visualization of the atomistic structures and stress distributions. Defect structures were viewed by using the centro-symmetry parameter.

4.3 Results

4.3.1 Single Crystal - 0TB

Figure 4.2 shows snapshots of the defect structures of the $4\text{nm} \times 7\text{nm} \times 28\text{nm}$ single crystal specimen at different time-intervals and their corresponding strains. The single crystals with different thicknesses also show a very similar deformation pattern for all the sizes as illustrated in Figure 4.4. An intrinsic stacking fault (SF) first nucleates from the crack tip along a $\{111\}$ slip plane. As the leading partial reaches the free surface, a twin partial $[126]$ nucleates from the crack tip on an adjacent slip plane. This transforms the intrinsic SF into an extrinsic SF (two TBs separated by a layer of atoms). The distance between these two TBs keeps increasing causing the crack to blunt. Eventually, another intrinsic SF nucleates from the crack tip in the plane of the crack and the leading partial exits from the free surface as seen in Figure 4.2.

4.3.2 Twinned Sample - 4TB

Figure 4.3 shows snapshots of the defect structures of the $4\text{ nm} \times 7\text{ nm} \times 28\text{ nm}$ twinned (4TB) sample with $\lambda = 6\text{nm}$ at different time-intervals and their corresponding strains. The defect structures for the remaining twinned nanopillars with $\lambda = 6\text{ nm}$ at different time-intervals and strains are shown in Figure 4.6 for

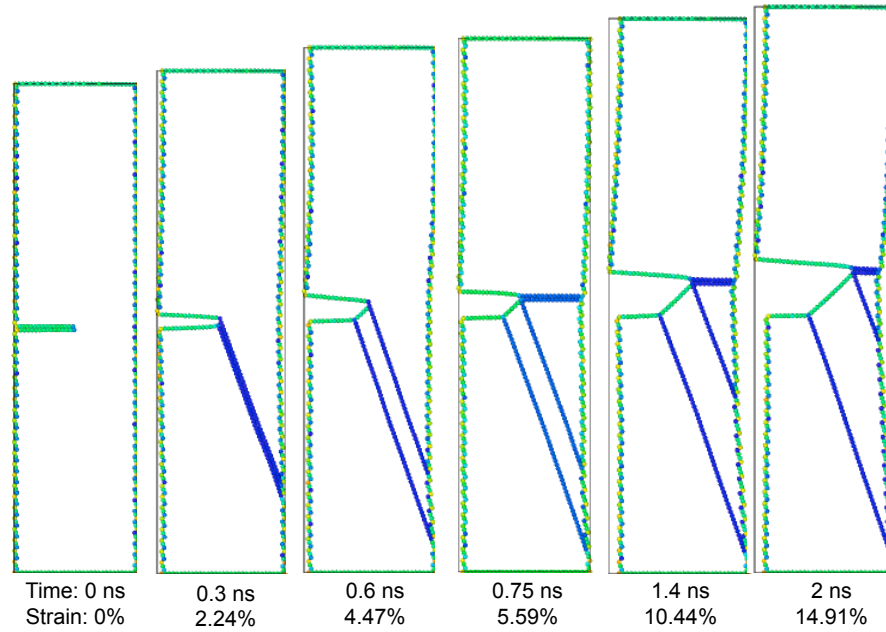


Figure 4.2: Defect structures at different time intervals for the 7nm thick single crystal (0TB) sample.

varying thicknesses. Their size-effect has been discussed in details in section 4.4.1. The deformation behavior for both the twin spacings ($\lambda = 8$ nm and 6 nm) follows similar mechanism. The deformation in the twinned samples also initiates with an intrinsic SF nucleating from the crack tip like in the single crystalline case, but is now intercepted at the CTB before reaching the free surface. This causes a drastic difference in the deformation mechanism. The intersection of the SF and the TB results in the formation of a stair rod dislocation, as shown in equation (3.1), which is an important hardening mechanism. As the tensile loading increases, we observe nucleation of dislocations from the SF-TB intersections, which eventually interact with the free surface and the adjacent TB. Blunting of the crack continues after the nucleation of the twin partial adjacent to the initial intrinsic SF but its propagation is checked by the dislocation pile-up ahead of the crack tip. The path of the twin partial from the SF is no longer smooth as it was in the single crystal and we see significant strain hardening. As the strain increases, the dislocations

in the adjacent twin spacing (adjacent to the one containing the crack) annihilate and eventually disappear leaving only the center twin lamellae with dislocations ultimately making it look similar to the deformation in the single crystal.

In these twinned samples with 4 CTBs, an interesting phenomenon is observed. The dislocation activity seems to be restricted only within two consecutive twin lamellae, the one containing the crack and the other right below it. This behavior is observed irrespective of the sample thicknesses or the sizes of the twin spacing $\lambda = 8$ nm, 6 nm and 4 nm. This observation renders TBs as an effective tool for containing the plasticity in a nanopillar and thereby strengthening it.

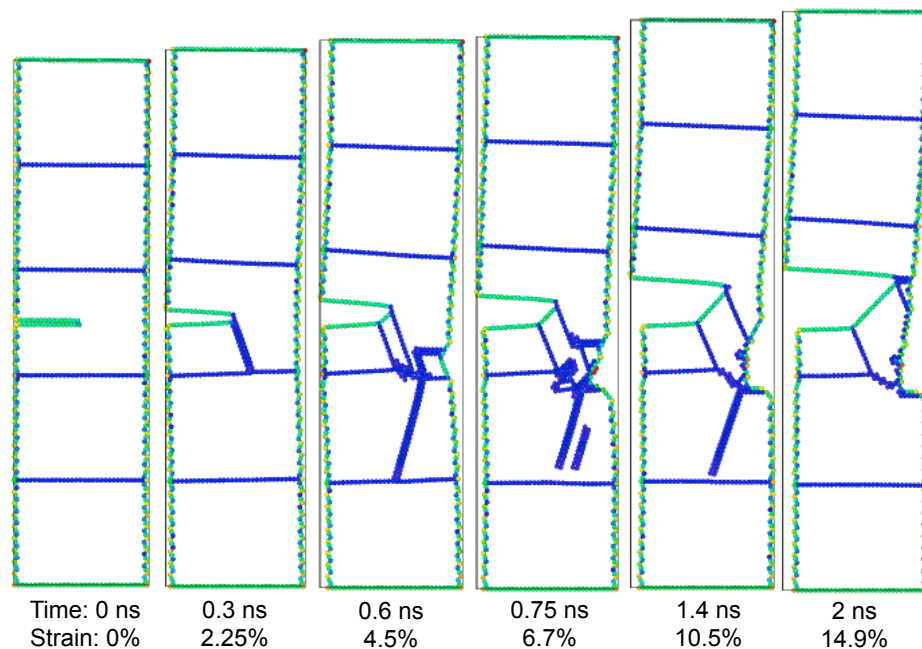


Figure 4.3: Defect structures at different time intervals for the 7 nm thick nanotwinned (4TB) sample with $\lambda = 6$ nm.

4.4 Discussion

4.4.1 Effect of Sample Thickness

As mentioned earlier, Figure 4.4 shows the snapshot of the defect structures

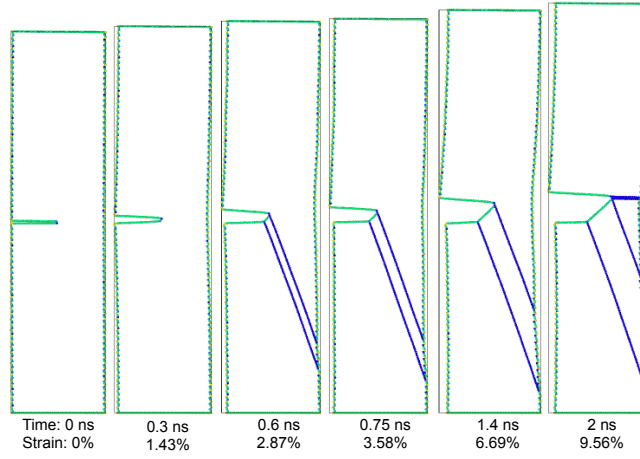
for the single crystals with thickness 10nm, 14nm, and 18nm respectively. It is observed that the thickness does not result in any significant difference in the deformation mechanism. However, we note that the horizontal SF is formed at about 5.59% strain (0.75ns) for the 7 nm sample, 9.32% strain (1.95ns) for the sample 10 nm, and 6.47% (1.8ns) for the 14 nm specimen. It is not seen till 6.3% strain (2ns) for the 18 nm sample. Thus, it is favored at a lower strain with decreasing sample thickness, as the free surface gets closer to the crack tip. This is due to the fact that dislocations are attracted to a free surface which has been explained based on linear elasticity [127].

Figure 4.5 shows the stress-strain curves for single crystal samples with varying sizes. The first drop on the curve corresponds to the nucleation of an intrinsic SF from the crack tip and its growth downwards till it reaches the free surface. Both the yield strengths (YS) and the ultimate tensile strengths (UTS) can be seen in the Figure and are tabulated in 4.1 for convenient comparison. We observe a clear size-effect with respect to the strength of the samples. The YS and UTS are both observed to increase as the thickness decreases, the effect being more pronounced in smaller samples.

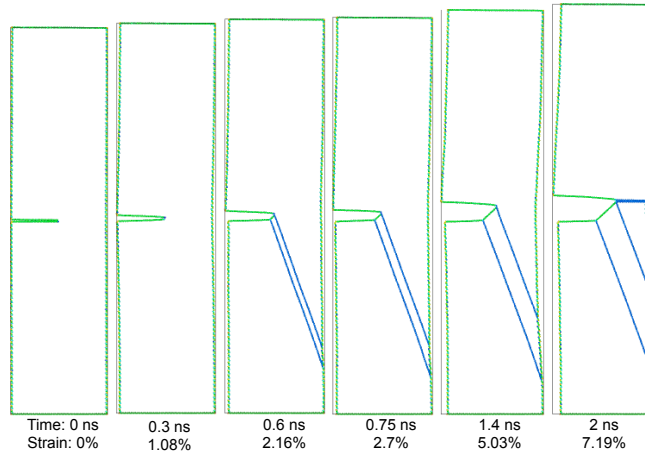
Table 4.1: Comparison of YS and UTS for different thicknesses of the untwinned (0TB) samples.

Thickness\Stress	YS (GPa)	UTS (GPa)
7nm	2.84	3.13
10nm	2.253	2.48
14nm	1.976	2.17
18nm	1.947	2.283

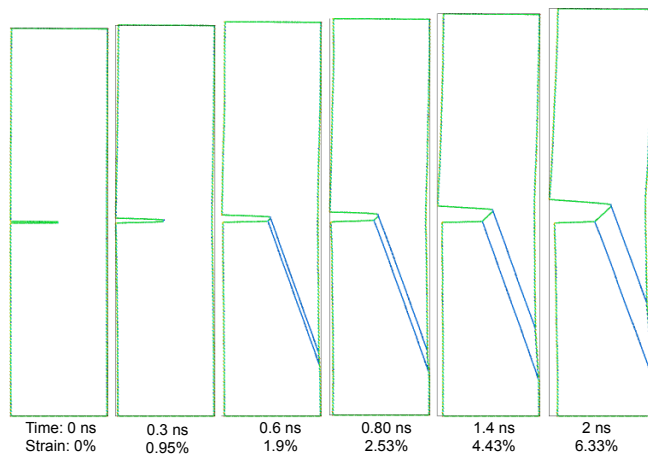
This is consistent with the literature, both experimental and theoretical, on size effects in nanopillars [131, 132, 133, 134]. In these studies, the size-effect on the yield stress or critical stress required for dislocation nucleation is attributed to the constrained volume offered by the thinner specimens, which makes it harder for the dislocations to nucleate. Moreover, according to the Griffith's criterion



(a) Single crystal with thickness 10nm



(b) Single crystal with thickness 14nm



(c) Single crystal with thickness 18nm

Figure 4.4: Defect structures at different strains/time-intervals for the single crystal (OTB) of varying thicknesses.

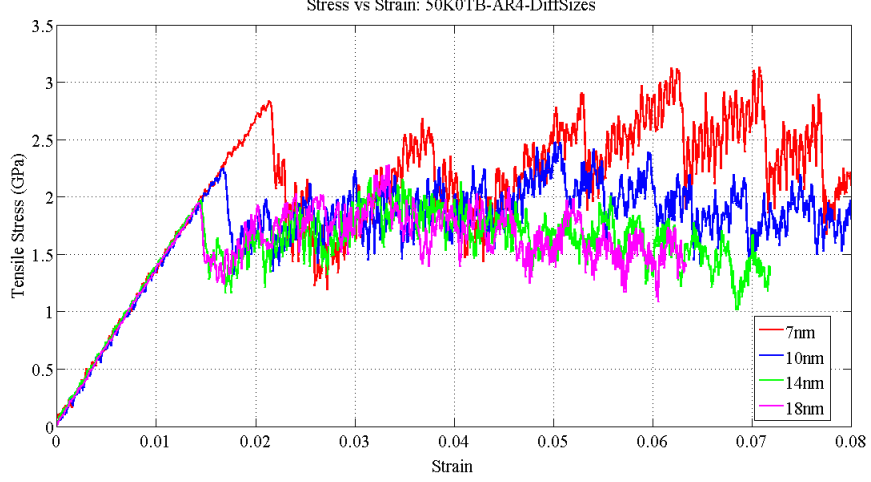


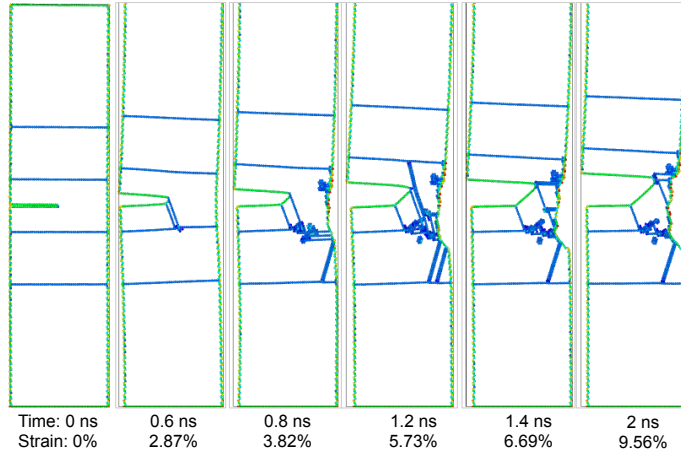
Figure 4.5: Stress-strain curves of the untwinned samples (0TB) with different thicknesses.

for brittle fracture, the stress intensity factor K for a sharp elliptical crack in an infinitely wide plate, is defined as

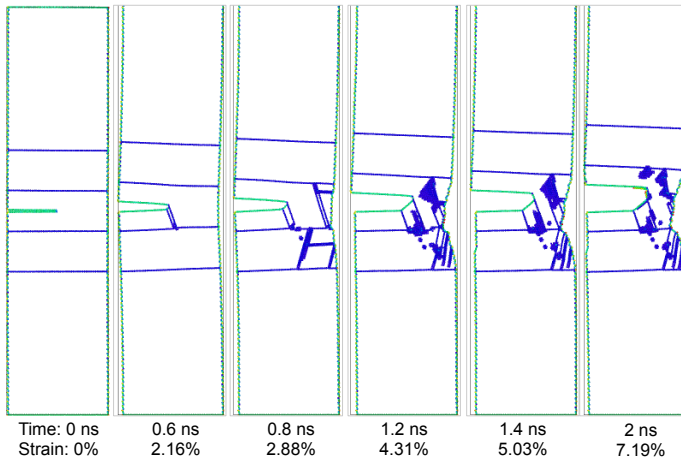
$$K = \sigma\sqrt{\pi a}, \quad (4.1)$$

where σ is the applied stress and a is the crack length [39]. Thus, as the thickness of the nanopillar decreases, the stress concentration at the crack tip decreases (crack length is half the thickness), which requires higher stress for the pre-existing crack to propagate. This explains the size-effect of the YS observed here. We also note that although the UTS increases with decreasing size, there is negligible hardening observed in the stress-strain curve for most specimens except the 7 nm specimen.

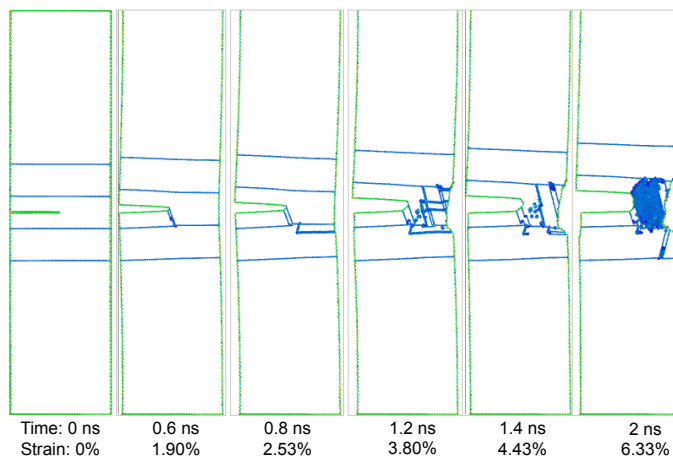
Figure 4.6 shows the defect structures for the twinned nanopillars with $\lambda = 6$ nm at different time-intervals and strains for varying thicknesses. It should be noted that for all thickness, the deformation in the nanotwinned pillar is contained within two twin lamellae as mentioned before. For $\lambda = 6$ nm, as the thickness increases, the activation of secondary slip systems seem to be favored possibly due to higher localized stresses due to dislocation pile-up. The secondary



(a) Nanopillar with thickness 10nm



(b) Nanopillar with thickness 14nm



(c) Nanopillar with thickness 18nm

Figure 4.6: Defect structures at different strains/time-intervals for the nan-otwinned sample (4TB with $\lambda = 6\text{nm}$) for varying thicknesses.

slip system does not appear in the thinner sample (7 nm), while it activates at a strain of 3.34% (0.07 ns) for 10 nm, at 3.95% (1.1 ns) for 14 nm, and at 5.07% (1.6 ns) for the 18 nm nanotwinned sample. It is also seen at 5.03% strain for 14 nm thick sample with $\lambda = 8$ nm. It isn't observed for the other specimens.

Figures 4.7 and 4.8 show the stress-strain curves for varying thicknesses of the twinned samples with 8 nm and 6 nm twin spacing respectively. The values of the YS and UTS are also tabulated in Table 4.2 and Table 4.3 for the twinned samples with $\lambda = 8$ nm and $\lambda = 6$ nm respectively. For the same reasons discussed above, the twinned nanopillars show a size dependence of the YS very similar to that exhibited by the single crystal as is evident from their stress-strain curves.

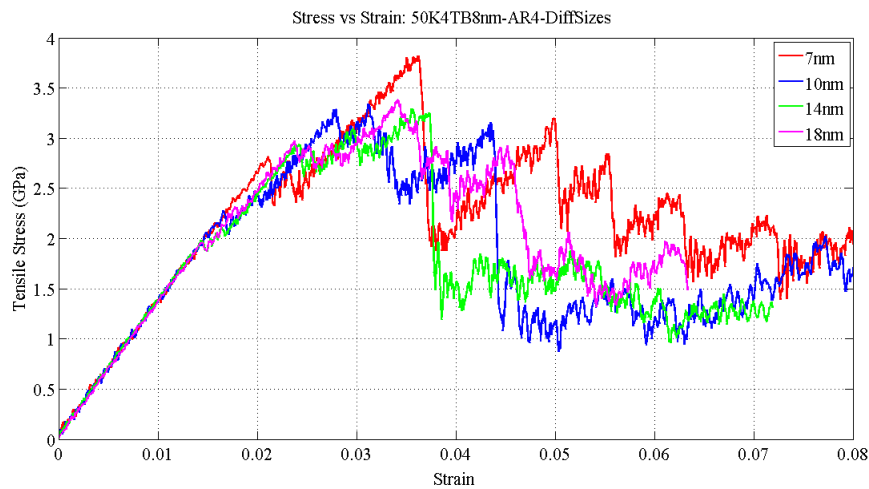


Figure 4.7: Stress-strain curves for the twinned sample (4TB) with $\lambda = 8$ nm for different thicknesses.

Table 4.2: Comparison of YS and UTS for different thicknesses of the twinned (4 TB) samples with $\lambda = 8$ nm.

Thickness\Stress	YS (GPa)	UTS (GPa)
7nm	2.818	3.820
10nm	2.278	3.341
14nm	1.983	3.291
18nm	1.961	3.381

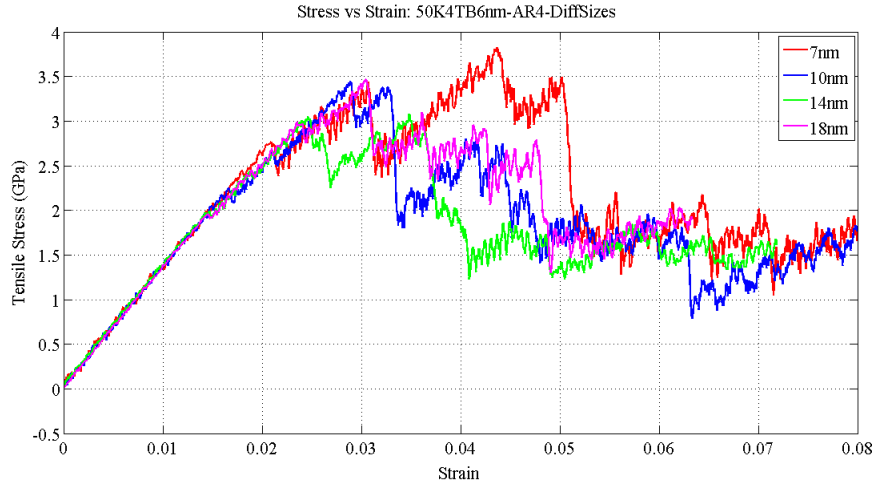


Figure 4.8: Stress-strain curves for the twinned sample (4TB) with $\lambda = 6\text{nm}$ for different thicknesses.

Table 4.3: Comparison of YS and UTS for different thicknesses of the twinned (4TB) samples with $\lambda = 6\text{nm}$.

Thickness \ Stress	YS (GPa)	UTS (GPa)
7nm	2.763	3.823
10nm	2.254	3.45
14nm	1.99	3.082
18nm	1.957	3.466
21nm	1.665	3.453

We also observe that the UTS increases noticeably only for the 7 nm case, and decreases for the 14 nm thick sample, whereas it remains more or less constant for the other cases. Although the atomistic underpinning for this observation is not yet clear to us, we speculate that there must be a critical thickness either between 10 nm and 14 nm or between 14 nm and 18 nm at which there occurs a difference in the strain hardening as the thickness increases. This is observed in both the single crystal as well as the nanotwinned samples with 14 nm thickness. It would be insightful to perform more simulations with varying sample thickness to probe this variation in the UTS.

4.4.2 Effect of Twin Boundaries

Figures 4.9 through 4.12 show the comparison of the stress-strain curves for

the same thickness of untwinned samples and twinned samples with different twin boundary spacing. The values of the YS and UTS are tabulated in Table 4.4 and Table 4.5 respectively for the sake of comparison.

We first note that the twinned samples exhibit significant hardening as compared to the corresponding single crystal sample for the same thickness. The increase in UTS is attributed to this enhanced strain hardening in the twinned samples due to the presence of TBs which act as effective barriers for dislocation motion as described in section 4.3.2. This hardening is consistent with the Hall-Petch relation [39] given by the equation (1.8). Hall [37] and Petch [38] explained that the strength in polycrystals increases with decreasing size of the grain. As the grains become smaller, the increased density of grain boundaries serve as effective barriers for dislocation motion thereby strengthening the material [45, 135]. In our case, the Hall-Petch type strengthening is related to the twin lamella thickness instead of the grain size, which is consistent with prior works.

Our simulations show that for the same sample thickness, the first yield drop is the largest for the single crystal specimen and reduces as the twin spacing decreases, despite similar YS for both twinned and untwinned specimens. This is attributed to the absence of barriers in the single crystal specimen. Due to the low stacking fault energy of Cu, the SF ribbon nucleated from the crack-tip extends till the free surface, and leads to a corresponding large yield drop in the stress strain curve due to stress relaxation.

We further observe that the TBs effectively contain the dislocations within two twin lamellae, thus restricting the plasticity. No such localization of defects is seen in the single crystals. Despite the localization of the plastic deformation, the crack continues to exhibit blunting by continued dislocation emission on primary or secondary slip systems. This is because the TBs provide additional routes for dislocations to reach the free surfaces and thus prevent stress concentration

by dislocation pile-up. Since the TBs are also $\{111\}$ planes, the dislocations are absorbed and glide along the TBs to eventually exit from the free surface as shown in the defect structures (Figures 4.3 and 4.6).

Table 4.4: Comparison of YS (in GPa) of different sizes for the 0TB and 4TB ($\lambda = 8\text{nm}$, 6nm and 4nm) samples

Thickness\TB	0TB	4TB - 8nm	4TB - 6nm	4TB - 4nm
7nm	2.84	2.818	2.763	
10nm	2.253	2.278	2.254	2.241
14nm	1.976	1.983	1.990	2
18nm	1.947	1.961	1.957	

Table 4.5: Comparison of UTS (in GPa) of different sizes for the 0TB and 4TB ($\lambda = 8\text{nm}$, 6nm and 4nm) samples

Thickness\TB	0TB	4TB - 8 nm	4TB - 6 nm	4TB - 4 nm
7nm	3.13	3.820	3.823	
10nm	2.48	3.341	3.450	3.652
14nm	2.17	3.291	3.082	3.440
18nm	2.283	3.381	3.466	

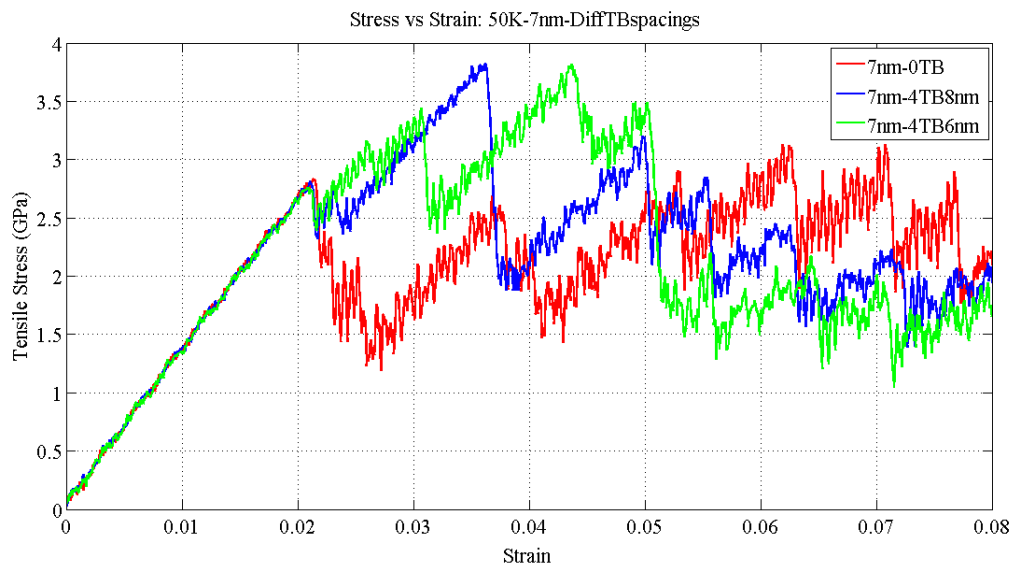


Figure 4.9: Comparison of the stress-strain curves for the twinned (4TB with $\lambda = 8\text{nm}$ and 6nm) and untwinned (0TB) samples with size $4\text{nm} \times 7\text{nm} \times 28\text{nm}$.

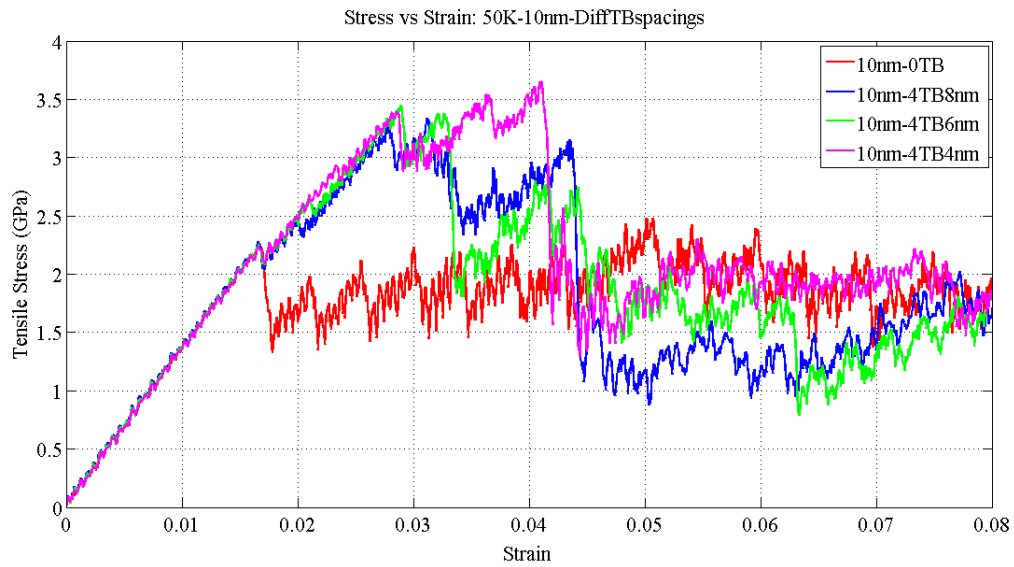


Figure 4.10: Comparison of the stress-strain curves for the twinned (4TB with $\lambda = 8\text{nm}$ and 6nm) and untwinned (0TB) samples with size $4\text{nm} \times 10\text{nm} \times 40\text{nm}$

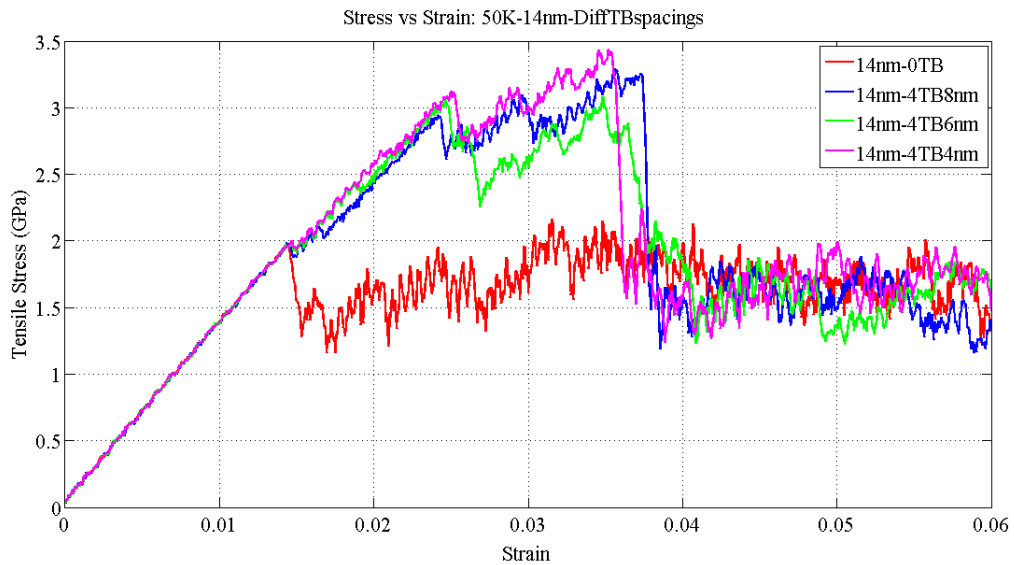


Figure 4.11: Comparison of the stress-strain curves for the twinned (4TB with $\lambda = 8\text{nm}$ and 6nm) and untwinned (0TB) samples with size $4\text{nm} \times 14\text{nm} \times 56\text{nm}$

4.4.3 Effect of Twin-Spacing

Based on Tables 4.4 and 4.5, we remark that there is not much influence of the twin spacing on the yield strength of the nanotwinned samples. This indicates that the presence of TBs does not affect the stress concentration at the crack tip that leads to the first nucleation event. We do see a slight increase in the UTS with decrease in the twin spacing for the same thickness of the nano pillars. Figure 4.13 shows the defect structures for the 10 nm thick nanotwinned samples with varying twin spacing. Moreover, since the plastic deformation is restricted within two twin lamellae for all nanotwinned samples studied here, we find that the smaller the twin spacing, more localized is the dislocation activity.

4.4.4 Effect of Different FCC Metals

In order to examine the response of different fcc metals, we performed similar simulations on Al and Ag nanotwinned samples to cover a range of parameters

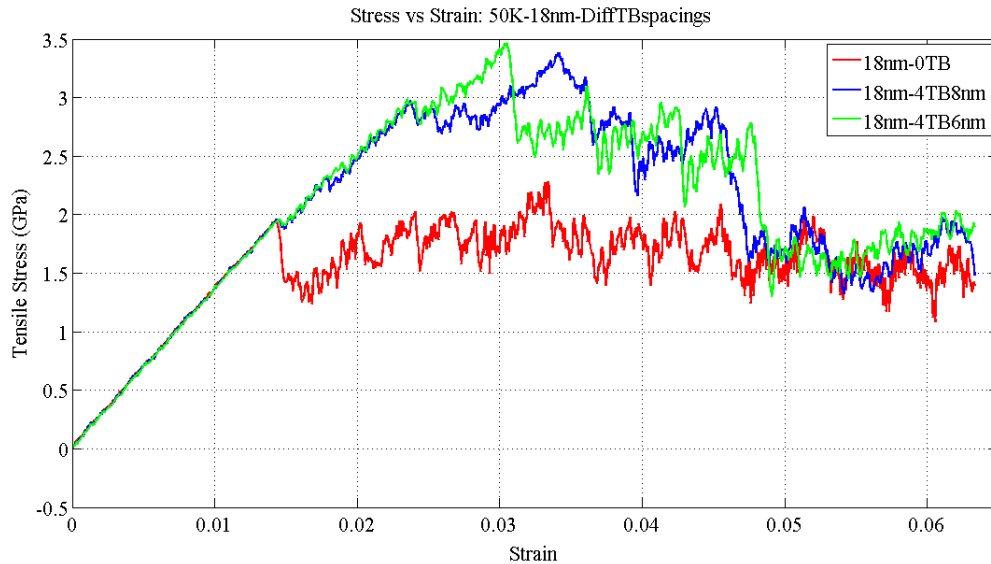
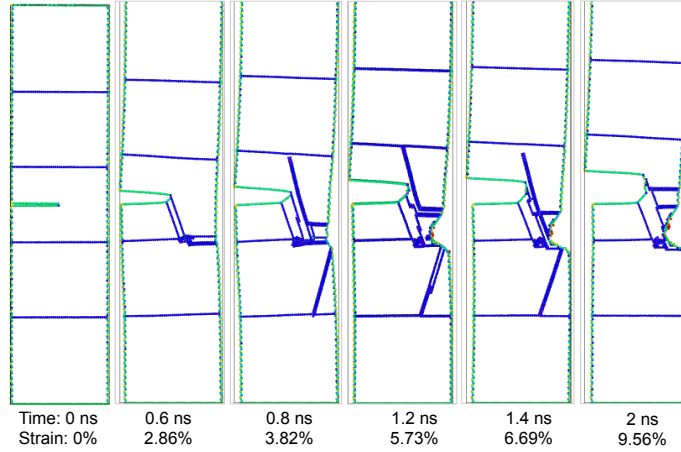
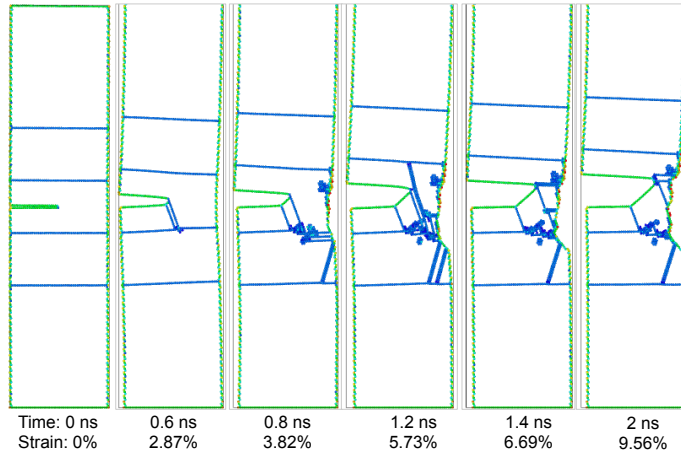


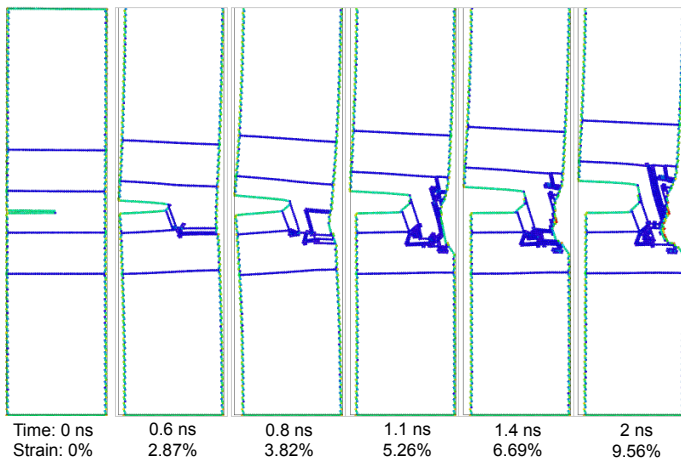
Figure 4.12: Comparison of the stress-strain curves for the twinned (4TB with $\lambda = 8\text{nm}$ and 6nm) and untwinned (0TB) samples with size $4\text{nm} \times 18\text{nm} \times 72\text{nm}$



(a) Nanopillar with 4TB λ 8nm



(b) Nanopillar with 4TB λ 6nm



(c) Nanopillar with 4TB λ 4nm

Figure 4.13: Defect structures at different strains/time-intervals for the twinned nanopillars with thickness 10nm.

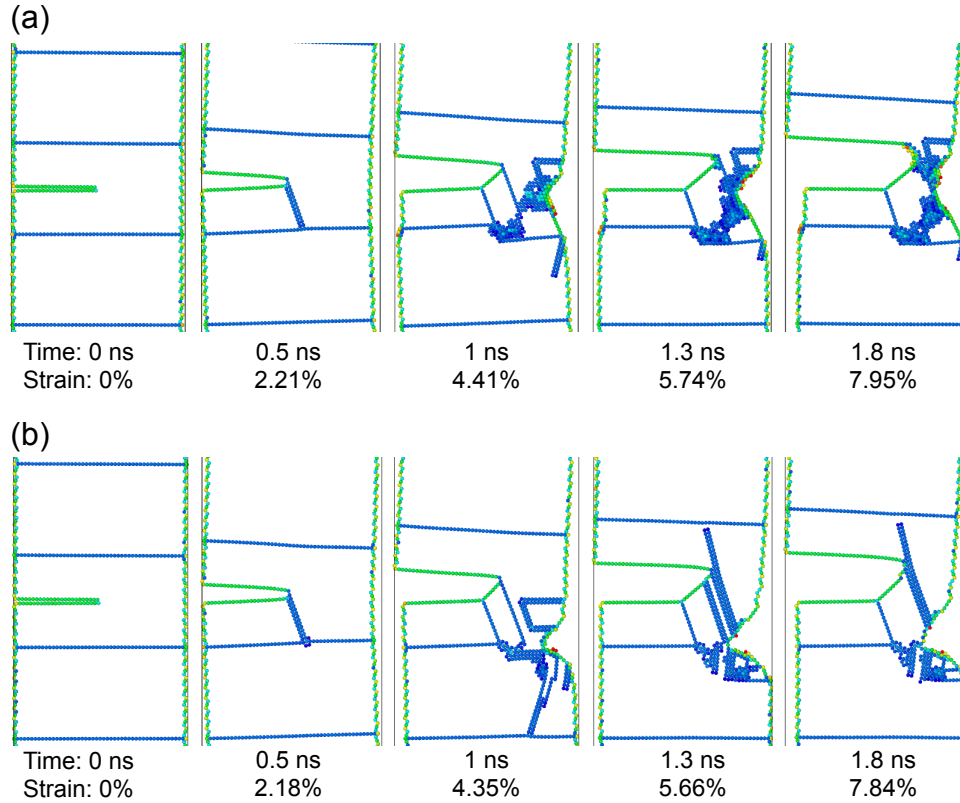


Figure 4.14: Snapshots of defect structures at different strains/timesteps of 12nm thick twinned nanopillars with $\lambda = 6\text{nm}$ for (a) Al and (b) Ag.

such as the stacking fault energies, and unstable stacking fault energies which are known to play a role in the brittle versus ductile response of fcc metals. In our simulations, these fcc metals also exhibit similar deformation mechanisms and restriction of the plasticity within two twins for samples of various thicknesses with an aspect ratio of 4. Some of the results are given in 4.14.

4.5 Conclusion

In summary, this chapter reports our study of the role of twin boundaries in the fracture response of twinned nanopillars. We find that the TBs lead to a dramatic strengthening as compared to the single crystal counterparts by serving as effective barriers for dislocation motion as well as providing routes for

dislocations to exit from the free surface. We observe a considerable size-effect in both twinned and untwinned nanopillars, with smaller pillars demonstrating higher yield strength. For the thicknesses and aspect ratio considered here, our simulations reveal that the TBs also restrict the plastic deformation within two twin lamellae in the vicinity of the crack tip. Although our primary study is on Cu, we find that Al and Ag also show similar behavior. Some preliminary simulations (not discussed here) show a possible critical aspect ratio below which the dislocation activity is no longer contained within the nearby TBs. We speculate that this critical aspect ratio is dependent on the thickness and the twin spacing of the nanotwinned pillars. Taken together, our findings show an interesting role of twin boundaries in restricting the plastic deformation as well as enhancing the fracture response of nanotwinned pillars, which can provide useful insights for the optimal design of nanotwinned structures. Further investigation of the effect of aspect ratio, and large sample thicknesses on different fcc metals provides some avenues for future work.

CHAPTER 5 FRACTURE RESPONSE OF NANOTWINNED POLYCRYSTALLINE COPPER WITH COLUMNAR GRAINS

5.1 Introduction

The study of the coherent twin boundary (TB) interaction in FCC metals in the previous chapters focused on bicrystals or nanotwinned pillars. This has been extended to polycrystals in this chapter. Polycrystals consisting of columnar hexagonal grains are used to compare the behavior of the samples with and without twin boundaries. Two different twin spacings (λ) of 5 nm and 3 nm are considered. A pre-existing elliptical crack is also introduced in middle of the center grain to examine the fracture response of the polycrystalline nanotwinned metals. Two positions of the crack are compared, horizontal and vertical with respect to the x-axis. The twinned samples show only a slightly higher strength as compared to the polycrystals without the TBs in case of the samples with horizontal cracks. A crack along a TB also show cleavage in accordance with our previous work [136] described in chapter 3. The TBs are more effective strengthening motifs for the samples with vertical cracks and showed a much higher strength when compared to the untwinned samples which are rendered weak due to the increase in triple junctions.

5.2 Methodology

The molecular dynamics (MD) simulations were performed on polycrystals consisting of hexagonal columnar grains of fcc copper with lattice constant 3.615

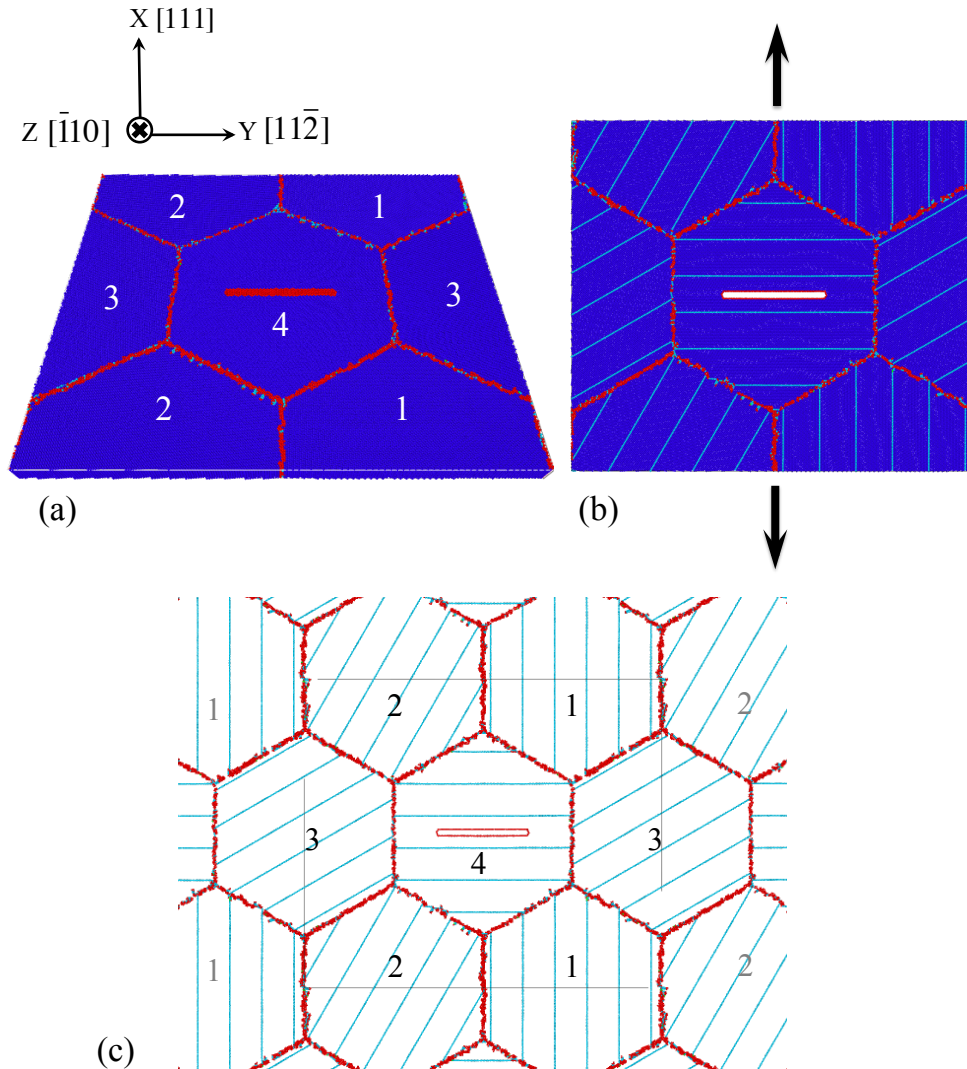


Figure 5.1: Polycrystalline sample after being relaxed which is (a) untwinned and (b) twinned with $\lambda = 5$ nm. (c) Shows the twinned sample with periodic images of the grains.

Å. The computational periodic cell consisted of four hexagonal grains numbered 1 through 4. The orientation of grain 1 was along the $[11\bar{2}]$, $[111]$ and $[1\bar{1}0]$ crystallographic directions. Grains 2, 3 and 4 were rotated around the $[1\bar{1}0]$ axis by 30° , 60° and 90° respectively in the x-y plane. The grains were equiaxed and the diameter of each grain was approximately 30 nm with the longer diameter (along x-direction) being 32 nm while the shorter diameter (along y-direction) being 28 nm. The size of the sample along the x and y directions was about (48×56) nm,

consisting of about 580,592 atoms. The thickness of the cell along the z direction was kept small at approximately 25 Å. As such, we model 2D-columnar grains as a simplified surrogate for the full 3D grain structure. Nanotwinned specimen were constructed by inserting coherent twin boundaries (TB) in each grain for comparison with the polycrystals without the twins, i.e., untwinned (0TB). Two different twin spacings of 3 nm and 5 nm were considered. A pre-existing elliptical blunt crack was created in the y-direction (horizontally) at the middle of the center grain by removing four layers of atoms. The length of the crack was 14 nm which was half the grain diameter. The initial structure was first relaxed using conjugate gradient energy minimization. Figure 5.1 shows the relaxed atomistic structure after energy minimization of (a) an untwinned specimen and (b) a nanotwinned sample with λ of 5 nm with the direction of the center grain, and numbering of the grains according to their orientations mentioned above. The coloring of the atoms is based on common neighbor analysis with the dark blue colors representing the fcc atoms, light blue being the hcp atoms, green being the bcc atoms and red representing all the other atoms. Figure 5.1 (c) shows the twinned polycrystalline sample with the periodic images of the grains with their numbering. The inset rectangle indicates our actual sample and the perfect fcc crystal atoms are not shown in the figure. Visualization of the samples are done using OVITO [18].

The MD program, LAMMPS [10], with an embedded-atom potential, developed by Mishin et al. [109], was used to simulate the behavior of 2D-columnar nanotwinned copper under uniaxial tensile deformation. We considered periodic boundary conditions in all three directions, and the simulations were performed in a constant NVT ensemble (fixed number of atoms, volume and temperature). The structure was then deformed by applying a constant tensile engineering strain rate, 10^8 /sec , along the x direction. Therefore, the box length

increased 0.01% of its original length in every picosecond (ps) in this direction. The applied deformation is uniaxial and the other two directions (y and z) are kept stress-free to shrink without keeping the periodic cell volume constant as it would be realistically. Atomic positions, velocities and accelerations are updated at each time step using the Velocity-Verlet algorithm. The total simulation time was set to 2 nanosecond (ns) with a time step of 0.001 ps. The very high strain rate is inherent to every MD simulation, and necessary to obtain a significant amount of deformation within a reasonable simulation time. For our simulation, the applied strain rate allows the structure to deform 10% in the x-direction. The temperature of the simulations is controlled using the NPT ensemble using the Nosé-Hoover thermostat [107] set to a constant temperature of 50 K. This method and the columnar grain samples used are similar to those used by Shabib and Miller [137], [96] and also by Jiao and Kulkarni in [138].

5.3 Results & Discussion

5.3.1 Effect of Twin Spacing

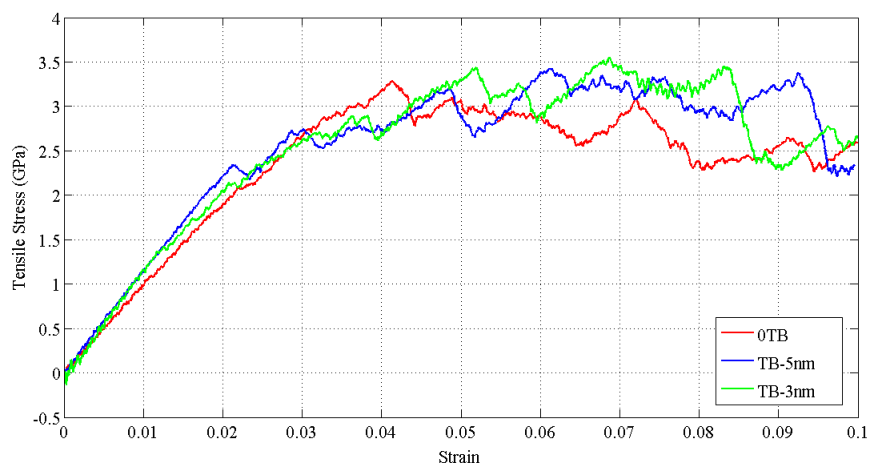


Figure 5.2: Stress-strain curves for the untwinned (0TB) and twinned (TB with $\lambda = 5$ nm and 3 nm) samples.

The tensile stress versus strain curves of the polycrystalline samples are compared for the untwinned samples and the twinned samples with λ equal to 5 nm and 3 nm in Figure 5.2. The values of the yield strength (YS) and the ultimate tensile strength (UTS) have been tabulated in Table 5.1. The YS of the twinned sample with λ 5 nm is slightly higher than that with λ 3 nm. The YS of the twinned samples is higher than that of untwinned sample as observed in several publications [96] [83] [129]. Due to the presence of the large amount of initial defects (grain boundaries) and different orientations of the grains, the yielding of the polycrystalline samples is not very conspicuous on the stress-strain curves. The YS for the untwinned sample is almost indistinguishable in the stress-strain curve. However, the UTS of the samples can be clearly seen in Figure 5.2. There is only a slight difference in the values of the UTS. Although all the three curves are very similar, the twinned sample with the smallest λ has the highest UTS while the untwinned sample has the lowest. This is consistent with our bicrystal results in section 4.4.3 and also other works [137] [139] [96] [83] [129].

Table 5.1: Comparison of YS and UTS for the untwinned (0TB) and twinned (TB with $\lambda = 5$ nm and 3 nm) samples.

Sample\Twin-Spacing	Yield Strength (GPa)	Tensile Strength (GPa)
0TB	2.09	3.29
TB λ 5nm	2.34	3.42
TB λ 3nm	2.14	3.55

The untwinned nanocrystalline sample shows crack blunting facilitated by the following deformation mechanisms which are illustrated in Figure 5.3, including partial or full dislocation emission from the crack tips and grain boundaries (GB), nucleation of twinning faults, TB migration, and interaction of dislocations with the dislocations and TBs. A lot of twinning accompanied by twin migration and annihilation are also observed in the surrounding grains. These are some key processes that have also been observed by other researchers, such as Shabib

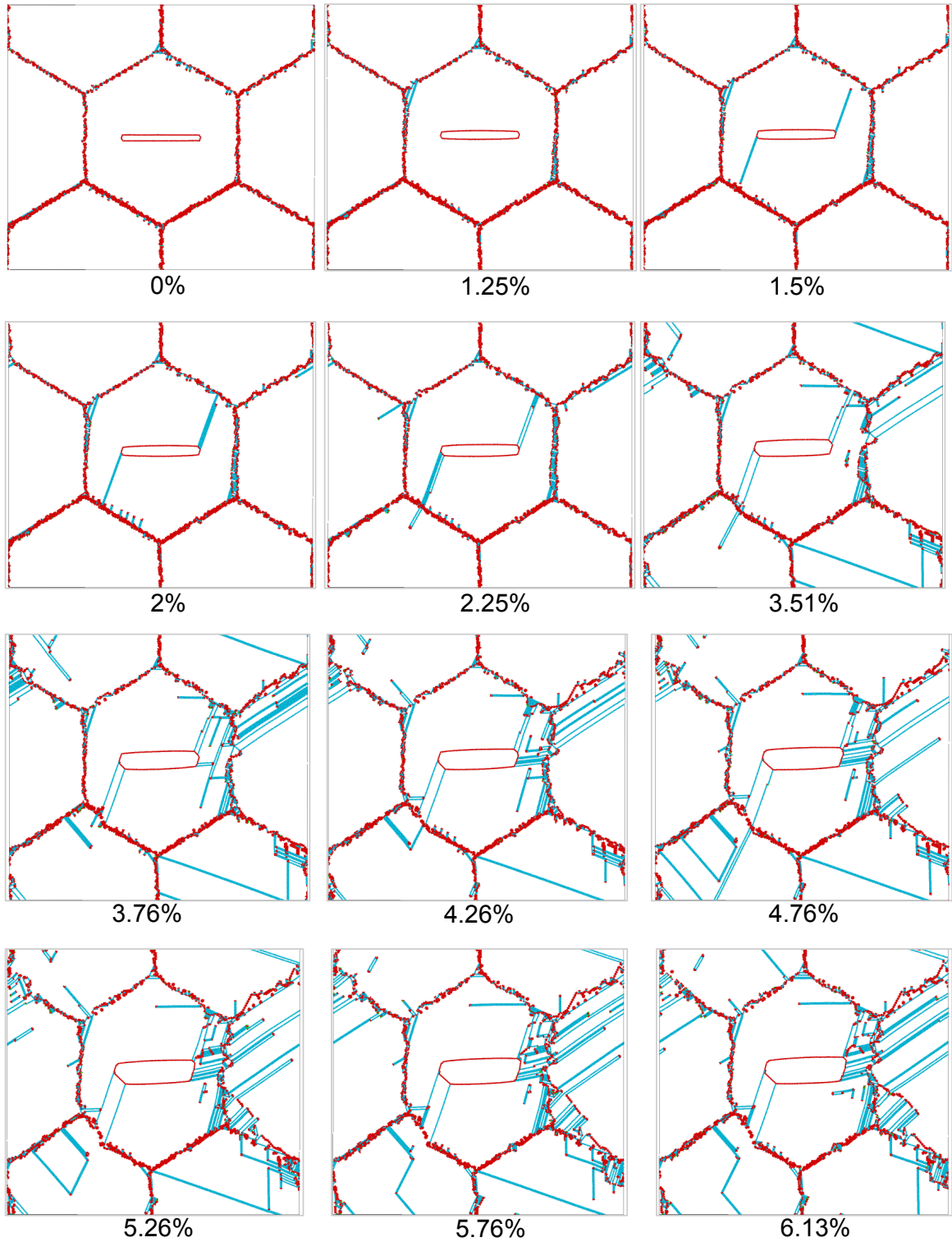


Figure 5.3: Defect structures at different strains of the untwinned polycrystalline sample containing a horizontal crack.

and Miller [137], Yamakov et al. [139], Zhou et al. [97], Cao and Wei [129], and Frøseth et al. [140].

The defect structures for the twinned samples with λ equal to 5 nm and 3 nm are presented in figures 5.4 and 5.5 respectively. The nanotwinned polycrystalline samples deform with all the foresaid mechanisms along with a few differences. The crack tip in this case undergoes blunting in the initial stages of deformation and eventually experiences a deflection as it propagates along a pileup of dislocations connecting it to a TB. This has been circled in black in Figure 5.4 on the images corresponding to strains 5.26% and 6.13%.

Another interesting mechanism observed in the twinned samples is the formation of curved TBs which has also been reported in previous publications [97] [141]. The curved TBs have been marked by the green arrows in figures 5.4 and 5.5. The formation of curved TBs is a bi-product of the reactions that lead to TB migration. The migration process is a result of partial dislocations emitted from the GBs at the GB/TB junction. In every instance, the migration process starts from the GBs and ends on the other side of the grain, shifting the entire TB into the neighboring (111) plane, as circled in orange in figures 5.4 and 5.5. Figure 5.6 illustrates a few examples of TB migration, circled in orange, and annihilation, marked in pink, in the twinned sample with λ equal to 3 nm. As evident from the figure, successive emissions of partial dislocations cause gradual change of the actual twin width inside the grain. However, when there is an excessive pileup of partial dislocations along the TB, it results in the formation of the curved TBs.

The deformation in both the λ equal to 5 nm and 3 nm are very similar. The only difference is the dislocation density in both the cases. As the deformation progresses, dislocations start to pile up against the TBs. The density of accumulated dislocations against the TBs is higher in the higher twin density models compared to the lower twin density models, as in the latter case there is more ev-

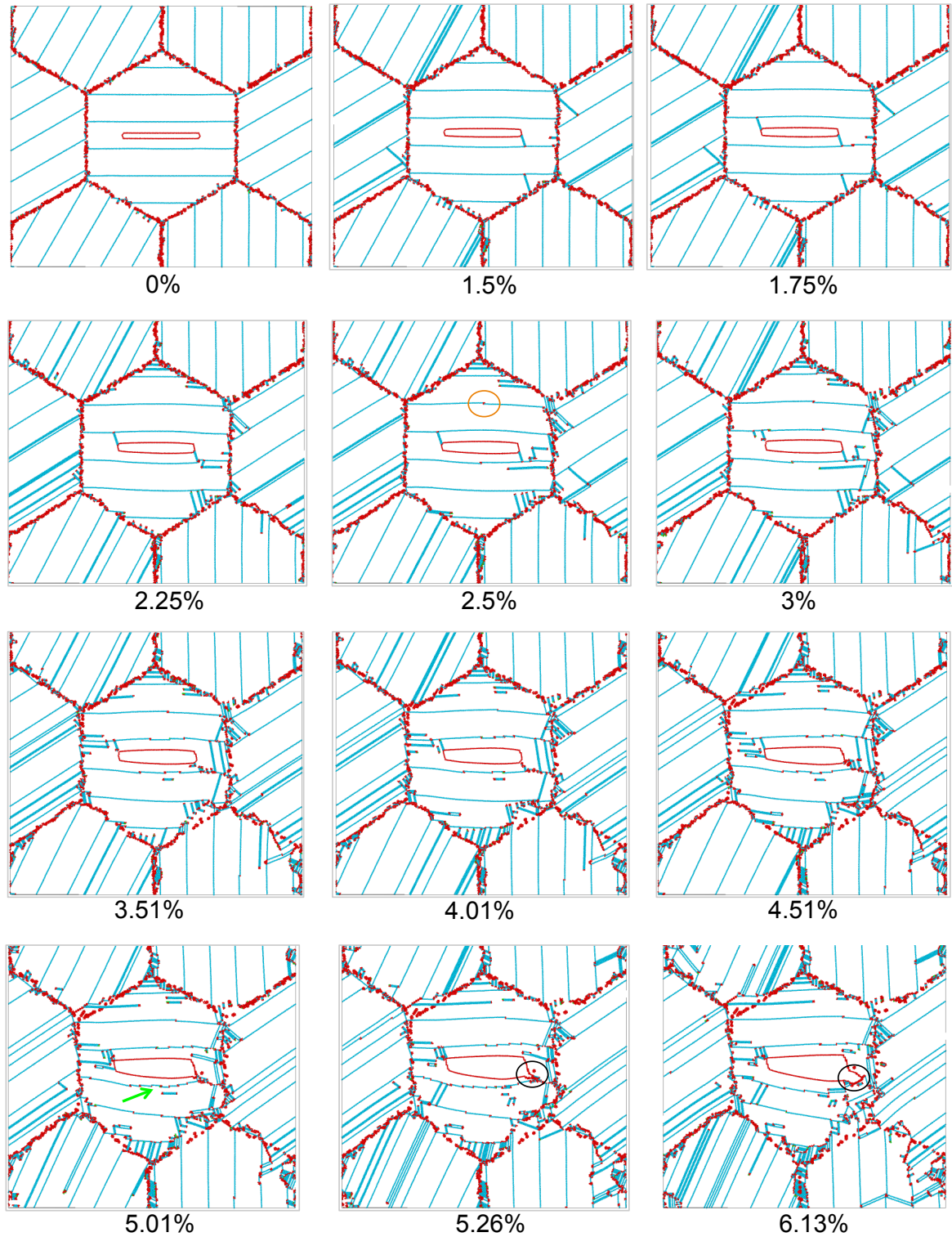


Figure 5.4: Defect structures at different strains for the twinned polycrystalline sample with $\lambda = 5$ nm containing a horizontal crack.

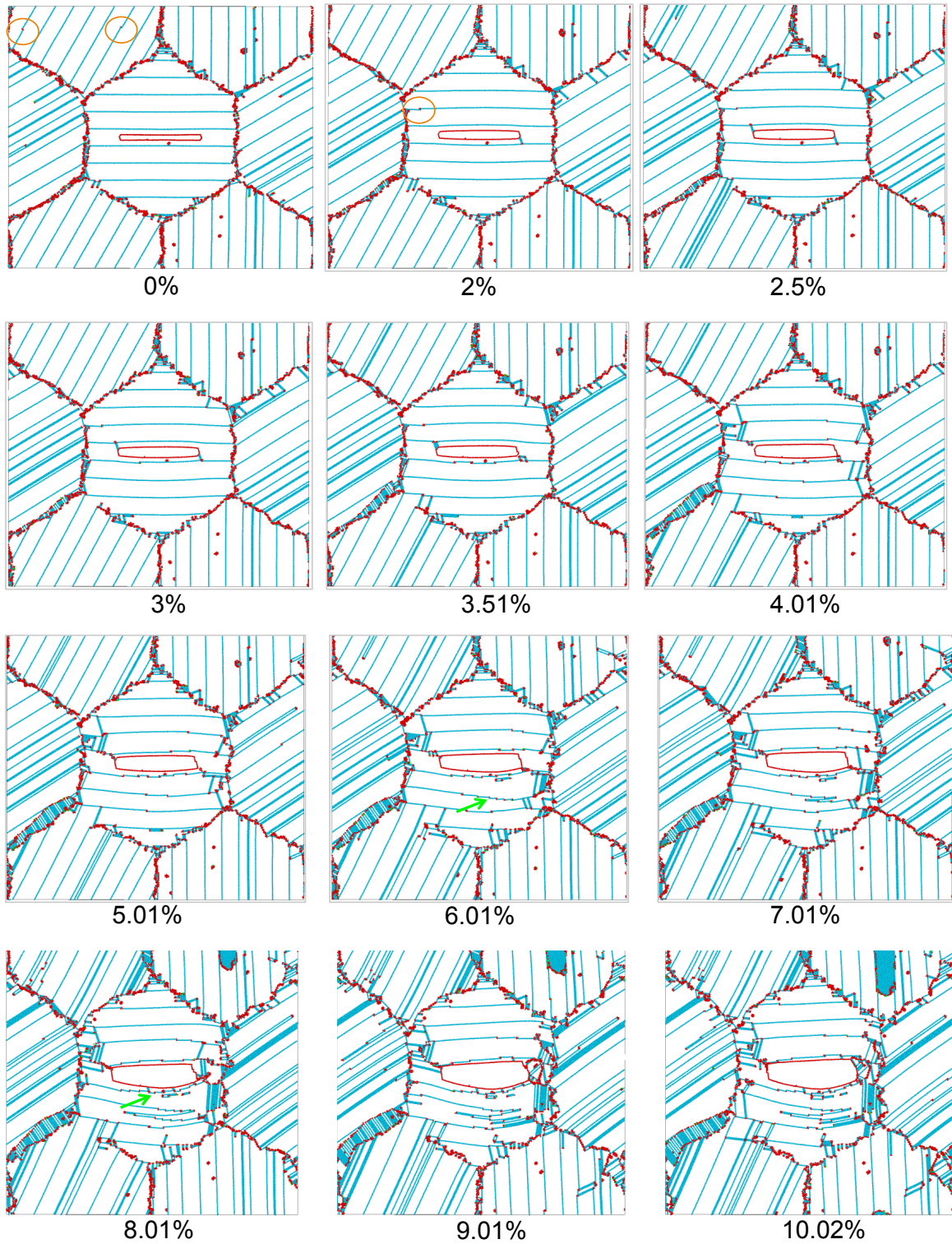


Figure 5.5: Defect structures at different strains for the twinned polycrystalline sample with $\lambda = 3$ nm containing a horizontal crack.

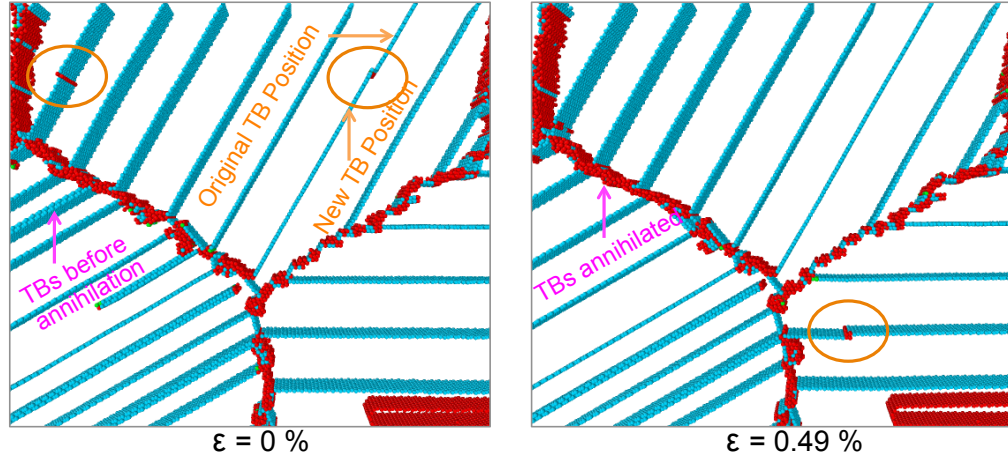


Figure 5.6: The TB migration process (orange) and the TB annihilation process (pink) in a twinned polycrystal with λ 3 nm.

idence of dislocations moving across the TBs that are subsequently intersected by the dislocations moving along the TBs. Moreover, as the twin density increases, the number of intersection points between the TBs with the GBs also increases. Hence, the possibility of triggering new dislocations in the neighboring grains also increases. Thus, the total number of nucleated dislocations is also found to be higher in the λ equal to 3 nm than in λ equals 5 nm sample [137].

5.3.2 Effect of a Cracked TB

In order to verify the hypothesis [136] we proposed in chapter 3, we positioned the crack such that one of its cleaved surfaces lies along a TB in the polycrystalline sample with λ equal to 3 nm. Since this crack has two crack tips unlike our nanopillar models in chapter 3, we observe two different behaviors of the crack tips. While the left crack tip is "ductile", the right crack tip is intrinsically "brittle". The deformation snapshots have been illustrated in Figure 5.7.

As discussed in section 3.3, an acute angle formed by the orientation of the crystals above and below the TB causes the crack tip to act ductile due to the ease of nucleation of the Shockley partials. On the other hand, an obtuse angle formed

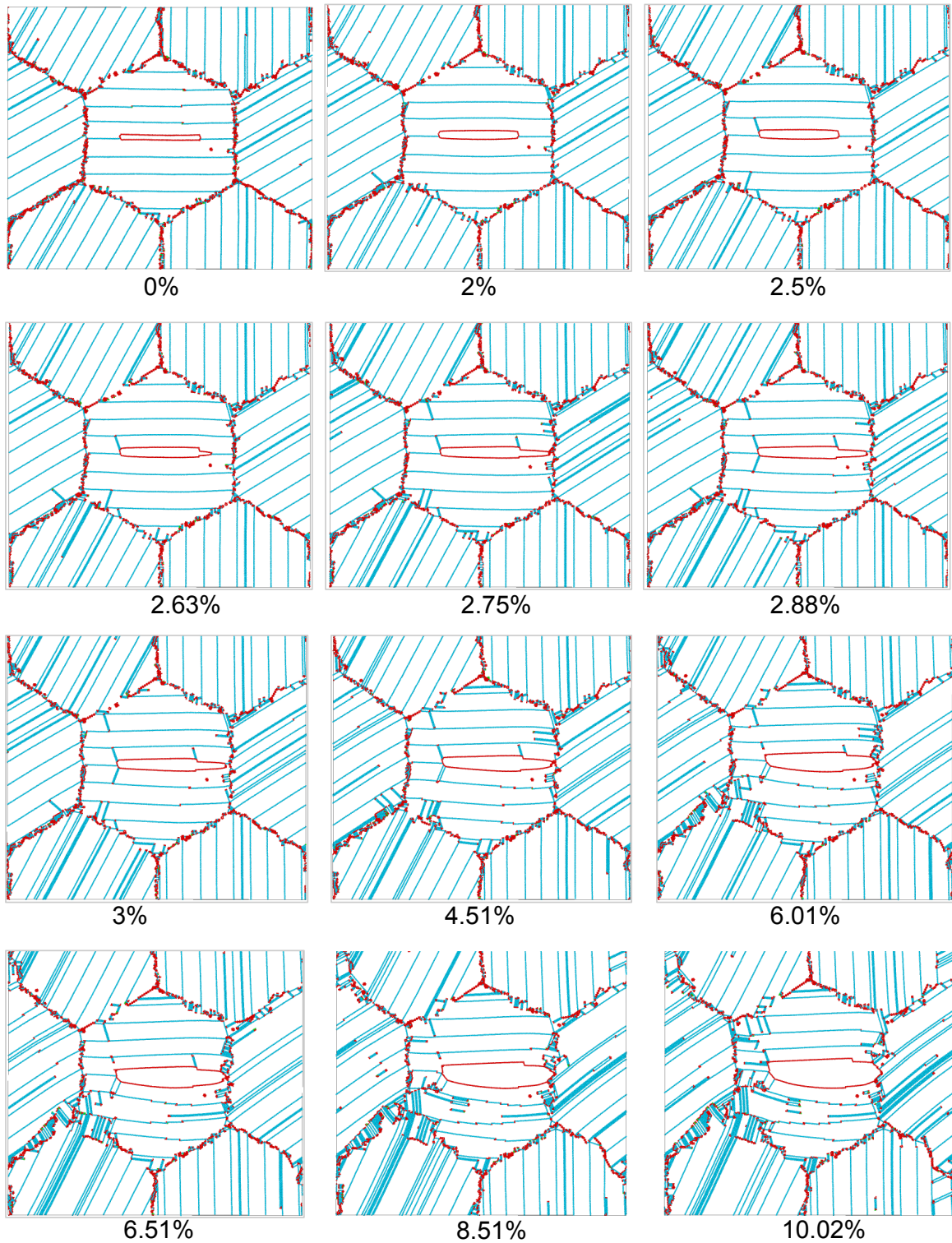


Figure 5.7: Defect structures at different strains for the twinned polycrystalline sample with $\lambda = 3$ nm containing a (horizontal) crack along a TB.

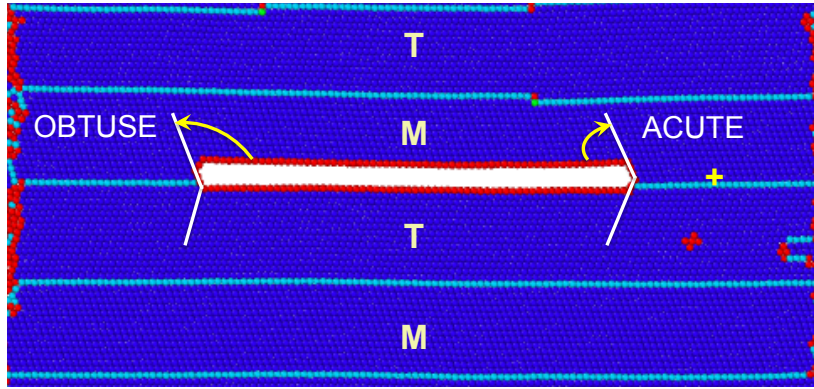


Figure 5.8: The obtuse (left) and acute (right) angles formed at the crack tips by the orientation of the matrix (M) and the twin (T) resulting in a ductile (left) and a brittle (right) crack tips .

in a similar fashion would cause the crack tip to be brittle and would readily cleave along the TB. Here we have the crack's surface along a positive TB with the left crack tip forming an acute angle while the right crack tip making an obtuse angle as depicted by Figure 5.8. Not surprisingly, we see partials nucleating from the left crack tip while the right crack tip results in propagation of the crack by decohesion along the TB to its right. The crack cleaves open in the right direction until it is arrested by the GB. This is interesting since our previous work had shown that although a crack tip that is inherently brittle would be expected to cleave along a TB, it need not do so in case of a "blunt" crack. We believe that this difference could be an effect of temperature. Since our prior work was carried out at 300 K, the intrinsically brittle blunt crack showed a more ductile response. The current simulations show a brittle response of a blunt crack due to very low temperature.

The stress-strain response of the twinned polycrystalline sample ($\lambda = 3$ nm) with the crack on TB has been compared for similar sample with a horizontal crack away from the TB in Figure 5.9. Due to the brittle nature of one of the crack tips, the strength is compromised when the TB is cracked.

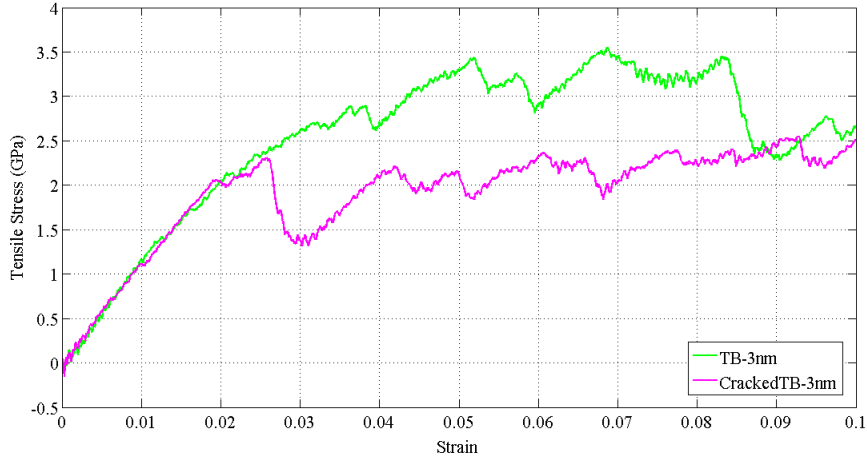


Figure 5.9: Comparison of the stress-strain curves for the twinned samples (TB with $\lambda = 3$ nm) and a crack along a TB (magenta) and a horizontal crack in the lamella (green).

5.3.3 Effect of Crack Orientation

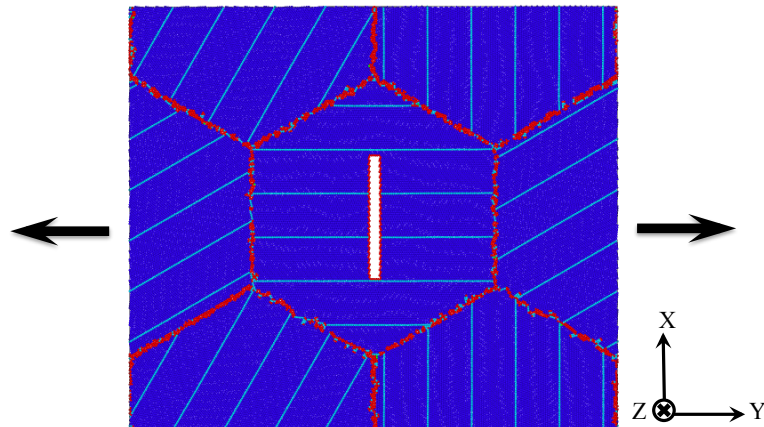


Figure 5.10: A vertical crack in a twinned polycrystal with λ 3 nm under mode I uniaxial tension.

To further investigate the interaction of the dislocations, TBs and GBs with the crack tip, a vertical crack (along x-direction) is introduced in the polycrystalline samples instead of the horizontal crack (along the y-direction) of the same length, 14 nm. This too is a mode I tensile simulation and the uniaxial deformation in this case is in y-direction as shown in Figure 5.10.

Figure 5.11 shows the comparison of the stress-strain curves for the un-

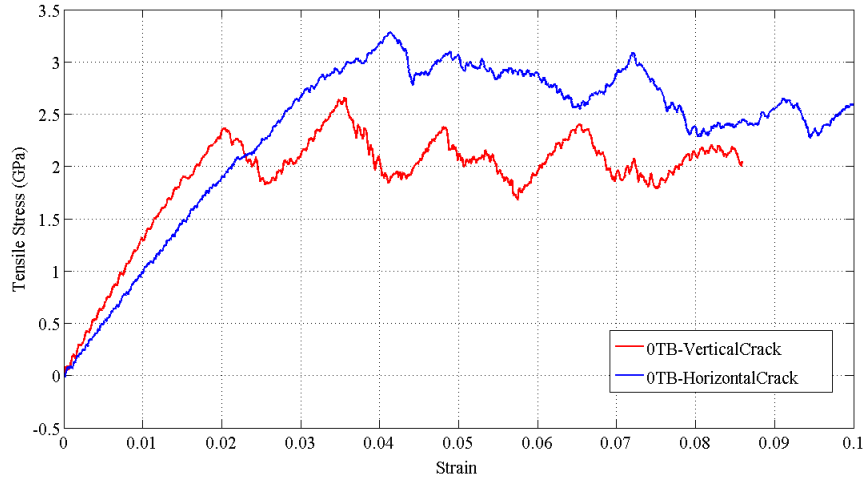


Figure 5.11: Comparison of the stress-strain curves for the untwinned (0TB) samples with a vertical crack (red) and a horizontal crack (blue) .

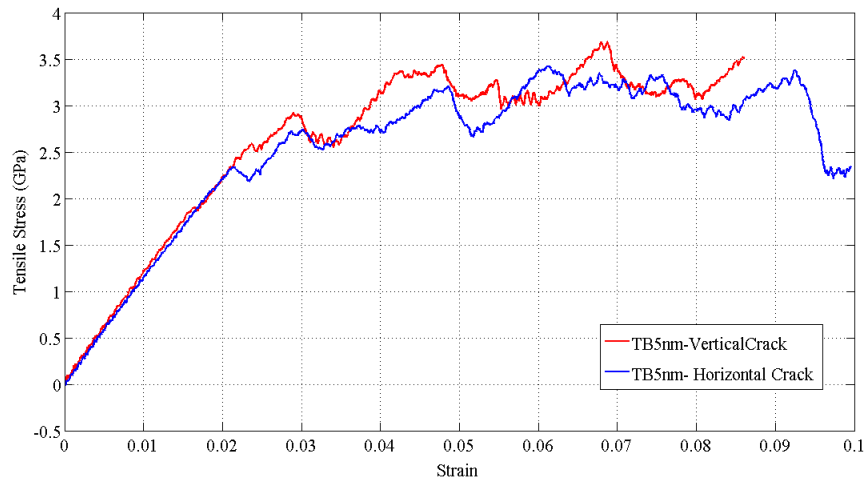


Figure 5.12: Comparison of the stress-strain curves for the twinned samples (TB with $\lambda = 5$ nm) with a vertical crack (red) and a horizontal crack (blue).

twinned polycrystalline samples containing the vertical crack with the one containing the horizontal crack. Just changing the orientation of the crack from horizontal to vertical, significantly decreases the strength of the untwinned sample. Similar comparison is made for the twinned polycrystalline sample λ equal to 5 nm in Figure 5.12. In this case, there is a slight increase in the strength when the orientation of the crack is changed from horizontal to vertical in the nanotwinned

sample. The defect structures for the untwinned and the twinned samples with the vertical cracks are presented in Figure 5.13. Their stress-strain curves are superimposed in Figure 5.14 showing a much higher strength and considerable hardening for the twinned sample than the untwinned sample.

This difference in strength caused by the change in orientation of the crack can be attributed to the presence of triple junctions and the change in the loading direction both of which result in significant defect activity. We observe more extensive stacking fault formations and twinning in all the grains when the loading is in the y-direction, compared to the previous case when the loading was along the x-direction. A triple junction is a point where three grain boundaries intersect. Thus, every vertex of our hexagonal grains would contribute as a triple junction. Triple junctions have been associated with initiation of plastic deformation [142, 143] through dislocation nucleation and grain boundary migration. Thus, having more triple junctions leads to enhanced plasticity and, in the absence of the reinforcing TBs as in case of an untwinned sample, results in softening of the sample. This can be observed in Figure 5.13(a) where GBs along the vertical crack (y-axis) disintegrate very quickly. This is not seen for the horizontal crack in Figure 5.3. Contrary to the untwinned case, the twinned sample experiences a slight increase in its strength. This is because the presence of TBs changes the deformation mechanism drastically. The TBs impede the free motion of dislocations and also assist in accumulation of dislocations which result in strain hardening and therefore, improves strength. Along with the triple junction points, which are responsible for plastic dislocation nucleation, the twinned samples also have several intersection points of TB-GB which also serve as primary sources of dislocation emission. The presence of TBs in between the crack tips and the triple junction points, suppresses the effect of these junctions on the crack tips for both the horizontal and vertical cracks. This explains the comparable strengths observed for

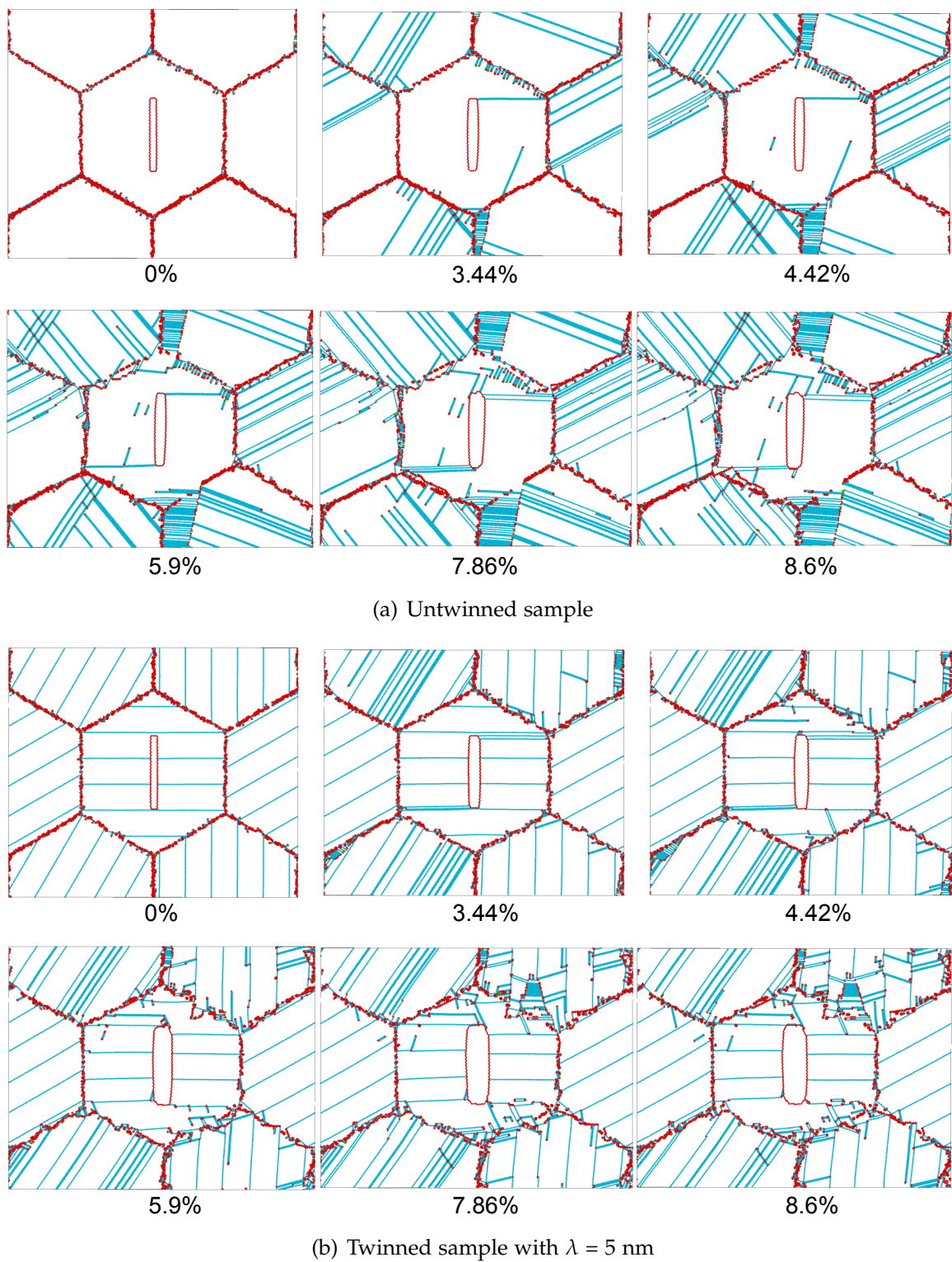


Figure 5.13: Defect structures at different strains for different polycrystalline samples containing a vertical crack.

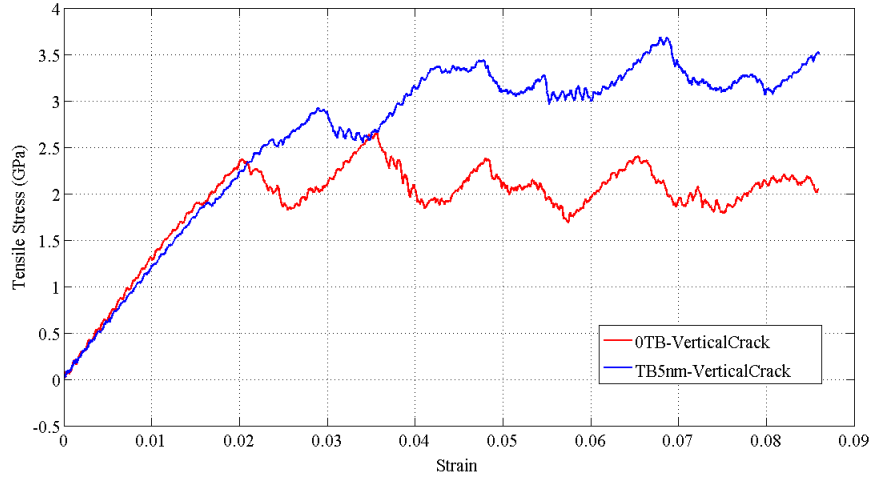


Figure 5.14: Comparison of the stress-strain curves for the untwinned (0TB) and twinned (TB with $\lambda = 5$ nm) samples.

the horizontal and vertical cracks in the twinned polycrystalline samples.

5.4 Conclusion

In summary, the deformation behavior of nanotwinned copper under uniaxial tensile load has been investigated by MD simulation. Several interesting deformation mechanisms have been revealed including: extended partial dislocation emission from the GBs, interaction of the partials with the TBs, TB migration, TB annihilation and dislocation emission from the steps on the TBs. The twinned samples with the horizontal cracks showed slightly higher strength than the untwinned sample due to dislocation-twin boundary interactions. Decrease in the twin spacing also increases the strength as it increases the TBs that act as effective barriers to dislocation motion. When the position of the crack is moved from a twin lamella to a TB, it shows an interesting combination of brittle and ductile response of the crack. While the left crack, that forms an obtuse angle, shows ductile behavior, the right crack, forming an acute angle, is intrinsically brittle and it cleaves along the TB until it hits the GB to its right. Unlike our previous

work, we were able to obtain a perfectly brittle behavior from a blunt brittle crack tip. This reveals that the shape of the blunt crack tip would dominate the fracture response of a crack along a TB. Changing the crack orientation from horizontal to vertical affected the results to a large extent due to loading direction and presence of triple junctions such that the twinned specimen exhibit enhanced strengthening than untwinned specimen for the vertical crack whereas their strengths are comparable for the horizontal crack. Although the present study provides insights into the effects of twin spacing, and position of the crack, it also opens up avenues for further computational studies on the effect of crack orientation, loading direction and temperature on the overall fracture response of polycrystalline nanotwinned materials.

CHAPTER 6 SUMMARY AND FUTURE

DIRECTIONS

Before closing, we summarize the primary accomplishments of this dissertation and discuss some of the limitations and potential directions for future investigations.

6.0.1 Conclusions

In Chapter 2, we elucidate the high temperature stability of coherent twin boundaries by way of shear simulations over a range of temperatures. Our study reveals an intriguing transition in the behavior of twin boundaries (TBs) at higher temperatures. At low and intermediate temperatures, the TBs exhibit normal motion coupled to shear deformation as expected, while at higher temperatures (above 0.5-0.7 T_m) considerable deformation twinning is observed, an occurrence that has not been observed before in fcc metals. It is found that the deformation mechanism at low and medium temperatures is shear-coupled normal motion for different fcc metals. However, the transition to twinning at high temperatures and the associated transition temperature is observed to vary in different metals. According to our study, Pd and Cu exhibit a transition temperature of about 0.65 T_m , while in Ag twin formation becomes the dominant mode of deformation at a much lower transition temperature of about 0.5 T_m . In sharp contrast, Al shows no transition at all even up to temperatures as high as 0.86 T_m and continues to exhibit twin migration. Thus, we conclude that metals which have greater twinnability (or higher β_t) also exhibit a greater tendency towards deformation twinning at higher temperatures. We also conjecture that in the metals which exhibit the transition, it possibly occurs due to the difference in the temperature

sensitivity of the competing mechanisms, namely, twin migration and homogeneous nucleation of a stacking fault. This work has been published in the Journal of Applied Physics [124].

In Chapter 3, we investigate the propagation of pre-existing cracks, in copper twinned nanopillars, along coherent TBs to elucidate the fracture response of TBs owing to the effect of the crystallographic orientations in the adjoining twins. An important revelation of our study is that TBs exhibit alternating intrinsic brittleness and ductility. This is an interesting consequence of the directional anisotropy of an atomically sharp crack along a TB that favors cleavage in one direction and dislocation emission from the crack-tip in the opposite direction. For a "positive" TB, when the crack is directed along the positive Y-direction (the crack is on the left), it propagates via cleavage along the TB. However, when the direction of the crack is reversed (the crack is on the right), it favors dislocation emission from the crack-tip. The behavior reverses for a "negative" TB, i.e., a left crack nucleates dislocations from the crack-tip while a right crack propagates by decohesion along the TB. In the nanotwinned sample with multiple twins every alternating TB is positive and the adjacent ones are negative. Despite Cu being a ductile material, the brittle response essentially stems from the suppression of energetically favored slip planes for dislocation emission. It is further observed that a blunt crack exhibits ductility in all cases albeit with dramatically distinct deformation mechanisms associated with intrinsically brittle and ductile twin boundaries. Our findings resolve some of the intriguing studies of the brittle versus ductile response of nanotwinned metals reported in recent literature and sheds light on the previously held notion that twin boundaries are inherently brittle. This work has been submitted for publication and is currently under review [136].

While we further investigate the effect of twin-spacing (λ) and sample thickness on propagation of a pre-existing mode I crack in a twinned nanopillar, Chap-

ter 4 brings to light an interesting phenomenon of plasticity being localized within just two twin lamellae in nanopillars containing four coherent TBs. This response is also observed for other fcc metals, namely, Ag and Al. The yield strength exhibits noticeable size-effect in both single crystal and twinned specimen that stems from the size dependence of the critical stress required for dislocation nucleation. Increase in the thickness results in an overall decrease in strength of the sample. The presence of the TBs leads to significant strain hardening reminiscent of Hall-Petch strengthening as TBs arrest dislocation motion. The role of TBs in containing the plasticity in the vicinity of the crack tip observed for certain twin-spacings and aspect ratio of the nanopillars, is a key finding of this work which may be an important factor to consider in designing of nanotwinned structures.

Chapter 5 extends the analysis of the fracture response of nanotwinned metals to polycrystalline samples comprising of columnar hexagonal grains and containing an elliptical crack. It highlights several deformation mechanisms including extended partial dislocation emission from grain boundaries, interaction of the partials with the TBs, TB migration, TB annihilation and dislocation emission from the steps on TBs that govern the ductile response of a pre-existing crack. The twinned samples with the horizontal cracks showed slightly higher strength than the untwinned sample due to dislocation-twin boundary interactions. Decrease in the twin spacing also increases the strength as it increases the TBs that act as effective barriers to dislocation motion. When the position of the crack is moved from a twin lamella to a TB, it shows an interesting combination of brittle and ductile response of the crack consistent with our results of Chapter 3. While the left crack-tip, which is intrinsically ductile, shows ductile behavior, the right crack-tip is intrinsically brittle and cleaves along the TB.

6.0.2 Limitations and Future Work

We would like to note that finite temperature molecular dynamics simulations are limited by high strain rates. Consequently, a systematic study of the strain-rate dependence of some of the phenomena observed herein is beyond the scope of this work based purely on molecular dynamics. In the context of the high temperature response of twin boundaries, using free-energy minimization methods or time scaling approaches, such as the autonomous basin climbing method [144], and calculating the free energy barriers for twin motion versus twin formation in fcc metals at finite temperature could provide further insights into the anomalous deformation twinning observed in our simulations. It would be quite insightful to further investigate the response of realistic nanotwinned structures at high temperatures based on the competition between these mechanisms as well as GB mediated processes which become dominant at higher temperatures. In the context of the study of crack propagation along TBs, it bears emphasis that the contrasting behavior of alternating CTBs may often be dominated by other competing mechanisms. Our preliminary investigations indicate that changing the crack-length can lead to distinct deformation mechanisms. Moreover, the response of Al can also be different from other fcc metals such as Cu, and Ag. To provide atomistic insights into these aspects, the effects of the crack-length, material properties, and temperature are important avenues that warrant further experimental and computational investigations. Although the present study on twinned nanopillars and columnar nanotwinned structures provides insights into the role of twin boundaries, effects of twin boundary spacing, and sample dimensions, it also opens up avenues for further computational studies on the effect of crack orientation, loading direction and temperature on the overall fracture response of nanotwinned materials. We would also like to mention that all our studies were performed on perfect coherent twin boundaries, although fabricated

nanotwinned materials often have twin boundaries with steps or kinks and incoherent twin boundaries. In order for atomistic studies to be truly predictive, future focus on defective twin boundaries is needed.

REFERENCES

- [1] H. Gleiter, "Nanocrystalline Materials," *Progress in Materials Science*, vol. 33, no. 4, pp. 223–315, 1989.
- [2] T. D. de la Rubia and V. V. Bulatov, "Materials Research by Means of Multiscale Computer Simulation," *MRS Bulletin*, vol. 26, no. 03, pp. 169–175, 2001.
- [3] A. Nakano, M. E. Bachlechner, T. J. Campbell, R. K. Kalia, A. Omeltchenko, K. Tsuruta, P. Vashishta, S. Ogata, I. Ebbsjö, and A. Madhukar, "Atomistic Simulation of Nanostructured Materials," *Computing in Science and Engineering*, vol. 5, no. 4, pp. 68–78, 1998.
- [4] M. A. Meyers, A. Mishra, and D. J. Benson, "Mechanical Properties of Nanocrystalline Materials," *Progress in Materials Science*, vol. 51, no. 4, pp. 427–556, 2006.
- [5] L. Shilkrot, R. E. Miller, and W. A. Curtin, "Multiscale Plasticity Modeling: Coupled Atomistics and Discrete Dislocation Mechanics," *Journal of the Mechanics and Physics of Solids*, vol. 52, no. 4, pp. 755–787, 2004.
- [6] W. H. Beamer and C. R. Maxwell, "Physical Properties of Polonium. II. X-Ray Studies and Crystal Structure," *The Journal of Chemical Physics*, vol. 17, no. 12, pp. 1293–1298, 1949.
- [7] V. Bulatov and W. Cai, *Computer Simulations of Dislocations*. Oxford University Press, 2006.
- [8] M. Xiling and Y. Wei, "MD Simulation for Nanocrystals," *Acta Mechanica Sinica*, vol. 19, no. 6, pp. 485–507, 2003.

- [9] D. Chandler, *Introduction to Modern Statistical Mechanics*. Oxford University Press, 1987.
- [10] S. Plimpton, "Fast Parallel Algorithms for Short-Range Molecular Dynamics," *Journal of Computational Physics*, vol. 117, no. 1, pp. 1–19, 1995.
- [11] D. Frenkel and B. Smit, *Understanding Molecular Simulations From Algorithms to Applications*. Academic press, 2001.
- [12] M. S. Daw and M. I. Baskes, "Embedded-Atom Method: Derivation and Application to Impurities, Surfaces, and Other Defects in Metals," *Physical Review B*, vol. 29, no. 12, p. 6443, 1984.
- [13] M. S. Daw and M. Baskes, "Semiempirical, Quantum Mechanical Calculation of Hydrogen Embrittlement in Metals," *Physical Review Letters*, vol. 50, no. 17, p. 1285, 1983.
- [14] R. Johnson, "Analytic Nearest-Neighbor Model for FCC Metals," *Physical Review B*, vol. 37, no. 8, p. 3924, 1988.
- [15] C. L. Kelchner, S. Plimpton, and J. Hamilton, "Dislocation Nucleation and Defect Structure during Surface Indentation," *Physical Review B*, vol. 58, no. 17, p. 11085, 1998.
- [16] J. D. Honeycutt and H. C. Andersen, "Molecular Dynamics Study of Melting and Freezing of Small Lennard-Jones Clusters," *Journal of Physical Chemistry*, vol. 91, no. 19, pp. 4950–4963, 1987.
- [17] J. Li, "AtomEye: An Efficient Atomistic Configuration Viewer," *Modelling and Simulation in Materials Science and Engineering*, vol. 11, no. 2, p. 173, 2003.

- [18] A. Stukowski, "Visualization and Analysis of Atomistic Simulation Data with OVITO—the Open Visualization Tool," *Modelling and Simulation in Materials Science and Engineering*, vol. 18, no. 1, p. 015012, 2010.
- [19] G. Nieman, J. Weertman, and R. Siegel, "Microhardness of Nanocrystalline Palladium and Copper Produced by Inert-Gas Condensation," *Scripta Metallurgica*, vol. 23, no. 12, pp. 2013–2018, 1989.
- [20] K.-M. Lee, D.-J. Lee, and H. Ahn, "XRD and TEM studies on Tin Oxide (II) Nanoparticles Prepared by Inert Gas Condensation," *Materials Letters*, vol. 58, no. 25, pp. 3122–3125, 2004.
- [21] C. Suryanarayana, "Mechanical Alloying and Milling," *Progress in Materials Science*, vol. 46, no. 1, pp. 1–184, 2001.
- [22] H. Fecht, E. Hellstern, Z. Fu, and W. Johnson, "Nanocrystalline Metals Prepared by High-Energy Ball Milling," *Metallurgical Transactions A*, vol. 21, no. 9, pp. 2333–2337, 1990.
- [23] J. Eckert, J. Holzer, C. Krill, and W. Johnson, "Structural and Thermodynamic Properties of Nanocrystalline FCC Metals Prepared by Mechanical Attrition," *Journal of Materials Research*, vol. 7, no. 07, pp. 1751–1761, 1992.
- [24] U. Erb, "Electrodeposited Nanocrystals: Synthesis, Properties and Industrial Applications," *Nanostructured Materials*, vol. 6, no. 5, pp. 533–538, 1995.
- [25] L. Lu, R. Schwaiger, Z. Shan, M. Dao, K. Lu, and S. Suresh, "Nano-Sized Twins Induce High Rate Sensitivity of Flow Stress in Pure Copper," *Acta Materialia*, vol. 53, no. 7, pp. 2169–2179, 2005.
- [26] S. Zhong, T. Koch, M. Wang, T. Scherer, S. Walheim, H. Hahn, and T. Schimmel, "Nanoscale Twinned Copper Nanowire Formation by Direct Electrodeposition," *Small*, vol. 5, no. 20, pp. 2265–2270, 2009.

- [27] K. Lu, J. Wang, and W. Wei, "A New Method for Synthesizing Nanocrystalline Alloys," *Journal of Applied Physics*, vol. 69, no. 1, pp. 522–524, 1991.
- [28] Y. Iwahashi, J. Wang, Z. Horita, M. Nemoto, and T. G. Langdon, "Principle of Equal-Channel Angular Pressing for the Processing of Ultra-Fine Grained Materials," *Scripta Materialia*, vol. 35, no. 2, pp. 143–146, 1996.
- [29] Y. S. Park, K. H. Chung, N. J. Kim, and E. J. Lavernia, "Microstructural Investigation of Nanocrystalline Bulk Al–Mg Alloy Fabricated by Cryomilling and Extrusion," *Materials Science and Engineering: A*, vol. 374, no. 1, pp. 211–216, 2004.
- [30] R. Perez, B. Huang, and E. Lavernia, "Thermal Stability of Nanocrystalline Fe-10 wt.% Al Produced by Cryogenic Mechanical Alloying," *Nanostructured Materials*, vol. 7, no. 5, pp. 565–572, 1996.
- [31] C. Shute, B. Myers, S. Xie, T. Barbee Jr, A. Hodge, and J. Weertman, "Microstructural Stability during Cyclic Loading of Multilayer Copper/Copper Samples with Nanoscale Twinning," *Scripta Materialia*, vol. 60, no. 12, pp. 1073–1077, 2009.
- [32] M. Meyers and M. Carvalho, "Shock-Front Irregularities in Polycrystalline Metals," *Materials Science and Engineering*, vol. 24, no. 1, pp. 131–135, 1976.
- [33] P. Sanders, J. Weertman, and J. Barker, "Structure of Nanocrystalline Palladium and Copper Studied by Small Angle Neutron Scattering," *Journal of Materials Research*, vol. 11, no. 12, pp. 3110–3120, 1996.
- [34] L. Lu, X. Chen, X. Huang, and K. Lu, "Revealing the Maximum Strength in Nanotwinned Copper," *Science*, vol. 323, no. 5914, pp. 607–610, 2009.
- [35] Y. Shen, L. Lu, Q. Lu, Z. Jin, and K. Lu, "Tensile Properties of Copper with Nano-Scale Twins," *Scripta Materialia*, vol. 52, no. 10, pp. 989–994, 2005.

- [36] P. Sanders, J. Eastman, and J. Weertman, "Elastic and Tensile Behavior of Nanocrystalline Copper and Palladium," *Acta Materialia*, vol. 45, no. 10, pp. 4019–4025, 1997.
- [37] E. Hall, "The Lüders Deformation of Mild Steel," *Proceedings of the Physical Society. Section B*, vol. 64, no. 12, p. 1085, 1951.
- [38] N. Petch, "The Cleavage Strength of Polycrystals," *Journal of the Iron Steel Institute*, vol. 174, pp. 25–28, 1953.
- [39] G. E. Dieter and D. Bacon, *Mechanical Metallurgy*. McGraw-Hill New York, 1986.
- [40] J. P. Hirth and J. Lothe, *Theory of Dislocations*. John Wiley & Sons, 1982.
- [41] A. Chokshi, A. Rosen, J. Karch, and H. Gleiter, "On the Validity of the Hall-Petch Relationship in Nanocrystalline Materials," *Scripta Metallurgica*, vol. 23, no. 10, pp. 1679–1683, 1989.
- [42] H. Höfler and R. Averback, "Grain Growth in Nanocrystalline TiO₂ and its Relation to Vickers Hardness and Fracture Toughness," *Scripta Metallurgica et Materialia*, vol. 24, no. 12, pp. 2401–2406, 1990.
- [43] T. Volpp, E. Göring, W.-M. Kuschke, and E. Arzt, "Grain Size Determination and Limits to Hall-Petch Behavior in Nanocrystalline NiAl powders," *Nanostructured Materials*, vol. 8, no. 7, pp. 855–865, 1997.
- [44] J. Schiøtz and K. W. Jacobsen, "A Maximum in the Strength of Nanocrystalline Copper," *Science*, vol. 301, no. 5638, pp. 1357–1359, 2003.
- [45] S. Yip, "Nanocrystals: the strongest size," *Nature*, vol. 391, no. 6667, pp. 532–533, 1998.

- [46] X. Zhang, H. Wang, R. Scattergood, J. Narayan, C. Koch, A. Sergueeva, and A. Mukherjee, "Studies of Deformation Mechanisms in Ultra-Fine-Grained and Nanostructured Zn," *Acta Materialia*, vol. 50, no. 19, pp. 4823–4830, 2002.
- [47] C. Koch, D. Morris, K. Lu, and A. Inoue, "Ductility of Nanostructured Materials," *Mrs Bulletin*, vol. 24, no. 02, pp. 54–58, 1999.
- [48] X. Zhang, H. Wang, R. Scattergood, J. Narayan, and C. Koch, "Modulated Oscillatory Hardening and Dynamic Recrystallization in Cryomilled Nanocrystalline Zn," *Acta Materialia*, vol. 50, no. 16, pp. 3995–4004, 2002.
- [49] Y. Wang and E. Ma, "Temperature and Strain Rate Effects on the Strength and Ductility of Nanostructured Copper," *Applied Physics Letters*, vol. 83, no. 15, pp. 3165–3167, 2003.
- [50] Y. Wang, E. Ma, R. Z. Valiev, and Y. Zhu, "Tough Nanostructured Metals at Cryogenic Temperatures," *Advanced Materials*, vol. 16, no. 4, pp. 328–331, 2004.
- [51] E. Ma, Y. Wang, Q. Lu, M. Sui, L. Lu, and K. Lu, "Strain Hardening and Large Tensile Elongation in Ultrahigh-Strength Nano-Twinned Copper," *Applied Physics Letters*, vol. 85, no. 21, pp. 4932–4934, 2004.
- [52] M. Dao, L. Lu, Y. Shen, and S. Suresh, "Strength, Strain-Rate Sensitivity and Ductility of Copper with Nanoscale Twins," *Acta Materialia*, vol. 54, no. 20, pp. 5421–5432, 2006.
- [53] E. Qin, L. Lu, N. Tao, and K. Lu, "Enhanced Fracture Toughness of Bulk Nanocrystalline Cu with Embedded Nanoscale Twins," *Scripta Materialia*, vol. 60, no. 7, pp. 539–542, 2009.

- [54] A. Karimpoor, K. Aust, and U. Erb, "Charpy Impact Energy of Nanocrystalline and Polycrystalline Cobalt," *Scripta Materialia*, vol. 56, no. 3, pp. 201–204, 2007.
- [55] T. Hanlon, E. Tabachnikova, and S. Suresh, "Fatigue Behavior of Nanocrystalline Metals and Alloys," *International Journal of Fatigue*, vol. 27, no. 10, pp. 1147–1158, 2005.
- [56] H. Li and F. Ebrahimi, "Transition of Deformation and Fracture Behaviors in Nanostructured Face-Centered-Cubic Metals," *Applied Physics Letters*, vol. 84, no. 21, pp. 4307–4309, 2004.
- [57] H. Li and F. Ebrahimi, "Ductile-to-Brittle Transition in Nanocrystalline Metals," *Advanced Materials*, vol. 17, no. 16, pp. 1969–1972, 2005.
- [58] I. Ovid'ko, A. Sheinerman, and E. Aifantis, "Stress-Driven Migration of Grain Boundaries and Fracture Processes in Nanocrystalline Ceramics and Metals," *Acta Materialia*, vol. 56, no. 12, pp. 2718–2727, 2008.
- [59] I. Ovid'ko and A. Sheinerman, "Grain Size Effect on Crack Blunting in Nanocrystalline Materials," *Scripta Materialia*, vol. 60, no. 8, pp. 627–630, 2009.
- [60] C. Peng, Y. Zhan, and J. Lou, "Size-Dependent Fracture Mode Transition in Copper Nanowires," *Small*, vol. 8, no. 12, pp. 1889–1894, 2012.
- [61] Y. Lu, J. Song, J. Y. Huang, and J. Lou, "Fracture of Sub-20nm Ultrathin Gold Nanowires," *Advanced Functional Materials*, vol. 21, no. 20, pp. 3982–3989, 2011.
- [62] V. Stolyarov, R. Valiev, and Y. Zhu, "Enhanced Low-Temperature Impact Toughness of Nanostructured Ti," *Applied Physics Letters*, vol. 88, no. 4, p. 041905, 2006.

- [63] L. Lu, Y. Shen, X. Chen, L. Qian, and K. Lu, "Ultrahigh Strength and High Electrical Conductivity in Copper," *Science*, vol. 304, no. 5669, pp. 422–426, 2004.
- [64] M. Dao, L. Lu, R. Asaro, J. T. M. De Hosson, and E. Ma, "Toward a Quantitative Understanding of Mechanical Behavior of Nanocrystalline Metals," *Acta Materialia*, vol. 55, no. 12, pp. 4041–4065, 2007.
- [65] K. Lu, L. Lu, and S. Suresh, "Strengthening Materials by Engineering Coherent Internal Boundaries at the Nanoscale," *Science*, vol. 324, no. 5925, pp. 349–352, 2009.
- [66] L. Lu, T. Zhu, Y. Shen, M. Dao, K. Lu, and S. Suresh, "Stress Relaxation and the Structure Size-Dependence of Plastic Deformation in Nanotwinned Copper," *Acta Materialia*, vol. 57, no. 17, pp. 5165–5173, 2009.
- [67] X. Zhang, H. Wang, X. Chen, L. Lu, K. Lu, R. Hoagland, and A. Misra, "High-Strength Sputter-Deposited Cu Foils with Preferred Orientation of Nanoscale Growth Twins," *Applied Physics Letters*, vol. 88, no. 17, pp. 173116–173116, 2006.
- [68] L. Lu, M. Dao, T. Zhu, and J. Li, "Size Dependence of Rate-Controlling Deformation Mechanisms in Nanotwinned Copper," *Scripta Materialia*, vol. 60, no. 12, pp. 1062–1066, 2009.
- [69] Y. Shen, L. Lu, M. Dao, and S. Suresh, "Strain Rate Sensitivity of Cu with Nanoscale Twins," *Scripta Materialia*, vol. 55, no. 4, pp. 319–322, 2006.
- [70] Q. Wei, S. Cheng, K. Ramesh, and E. Ma, "Effect of Nanocrystalline and Ultrafine Grain Sizes on the Strain Rate Sensitivity and Activation Volume: FCC versus BCC Metals," *Materials Science and Engineering: A*, vol. 381, no. 1, pp. 71–79, 2004.

- [71] H. Conrad, "Plastic Deformation Kinetics in Nanocrystalline FCC Metals Based on the Pile-up of Dislocations," *Nanotechnology*, vol. 18, no. 32, p. 325701, 2007.
- [72] R. J. Asaro and S. Suresh, "Mechanistic Models for the Activation Volume and Rate Sensitivity in Metals with Nanocrystalline Grains and Nano-Scale Twins," *Acta Materialia*, vol. 53, no. 12, pp. 3369–3382, 2005.
- [73] T. Zhu, J. Li, A. Samanta, H. G. Kim, and S. Suresh, "Interfacial Plasticity Governs Strain Rate Sensitivity and Ductility in Nanostructured Metals," *Proceedings of the National Academy of Sciences*, vol. 104, no. 9, pp. 3031–3036, 2007.
- [74] R. J. Asaro and Y. Kulkarni, "Are Rate Sensitivity and Strength Effected by Cross-Slip in Nano-Twinned FCC Metals," *Scripta Materialia*, vol. 58, no. 5, pp. 389–392, 2008.
- [75] Y. Kulkarni, R. J. Asaro, and D. Farkas, "Are Nanotwinned Structures in FCC Metals Optimal for Strength, Ductility and Grain Stability?" *Scripta Materialia*, vol. 60, no. 7, pp. 532–535, 2009.
- [76] J. W. Cahn, Y. Mishin, and A. Suzuki, "Coupling Grain Boundary Motion to Shear Deformation," *Acta Materialia*, vol. 54, no. 19, pp. 4953–4975, 2006.
- [77] A. Hodge, Y. Wang, and T. Barbee Jr, "Mechanical Deformation of High-Purity Sputter-Deposited Nano-Twinned Copper," *Scripta Materialia*, vol. 59, no. 2, pp. 163–166, 2008.
- [78] A. Cao, Y. Wei, and S. X. Mao, "Deformation Mechanisms of Face-Centered-Cubic Metal Nanowires with Twin Boundaries," *Applied Physics Letters*, vol. 90, no. 15, p. 151909, 2007.

- [79] K. A. Afanasyev and F. Sansoz, "Strengthening in Gold Nanopillars with Nanoscale Twins," *Nano Letters*, vol. 7, no. 7, pp. 2056–2062, 2007.
- [80] X. Li, Y. Wei, L. Lu, K. Lu, and H. Gao, "Dislocation Nucleation Governed Softening and Maximum Strength in Nano-Twinned Metals," *Nature*, vol. 464, no. 7290, pp. 877–880, 2010.
- [81] L. Li and N. M. Ghoniem, "Twin-Size Effects on the Deformation of Nanotwinned Copper," *Physical Review B*, vol. 79, no. 7, p. 075444, 2009.
- [82] Z. Shan, L. Lu, A. Minor, E. Stach, and S. Mao, "The Effect of Twin Plane Spacing on the Deformation of Copper Containing a High Density of Growth Twins," *Journal Of the Minerals*, vol. 60, no. 9, pp. 71–74, 2008.
- [83] A. Marchenko and H. Zhang, "Effects of Location of Twin Boundaries and Grain Size on Plastic Deformation of Nanocrystalline Copper," *Metallurgical and Materials Transactions A*, vol. 43, no. 10, pp. 3547–3555, 2012.
- [84] C. Saldana, T. Murthy, M. Shankar, E. Stach, and S. Chandrasekar, "Stabilizing Nanostructured Materials by Coherent Nanotwins and their Grain Boundary Triple Junction Drag," *Applied Physics Letters*, vol. 94, no. 2, p. 021910, 2009.
- [85] Y. Kulkarni and R. J. Asaro, "Are Some Nanotwinned FCC Metals Optimal for Strength, Ductility and Grain Stability?" *Acta Materialia*, vol. 57, no. 16, pp. 4835–4844, 2009.
- [86] F. Sansoz and J. Molinari, "Mechanical Behavior of Σ Tilt Grain Boundaries in Nanoscale Cu and Al: A Quasicontinuum Study," *Acta Materialia*, vol. 53, no. 7, pp. 1931–1944, 2005.

- [87] X. Zhang, O. Anderoglu, R. Hoagland, and A. Misra, "Nanoscale Growth Twins in Sputtered Metal Films," *Journal Of the Minerals*, vol. 60, no. 9, pp. 75–78, 2008.
- [88] H. Zhou and S. Qu, "The Effect of Nanoscale Twin Boundaries on Fracture Toughness in Nanocrystalline Ni," *Nanotechnology*, vol. 21, no. 3, p. 035706, 2010.
- [89] H. Zhou and S. Qu, "Molecular Dynamics Simulation of the Interaction between Nanoscale Twin Boundaries and Partial Dislocations," *Journal of Computational and Theoretical Nanoscience*, vol. 7, no. 10, pp. 1931–1934, 2010.
- [90] S.-W. Kim, X. Li, H. Gao, and S. Kumar, "In Situ Observations of Crack Arrest and Bridging by Nanoscale Twins in Copper Thin Films," *Acta Materialia*, vol. 60, no. 6, pp. 2959–2972, 2012.
- [91] J. Wang, F. Sansoz, J. Huang, Y. Liu, S. Sun, Z. Zhang, and S. X. Mao, "Near-Ideal Theoretical Strength in Gold Nanowires Containing Angstrom Scale Twins," *Nature Communications*, vol. 4, p. 1742, 2013.
- [92] D. Jang, X. Li, H. Gao, and J. R. Greer, "Deformation Mechanisms in Nanotwinned Metal Nanopillars," *Nature Nanotechnology*, vol. 7, no. 9, pp. 594–601, 2012.
- [93] L. Liu, J. Wang, S. Gong, and S. Mao, "Atomistic Observation of a Crack Tip Approaching Coherent Twin Boundaries," *Scientific Reports*, vol. 4, 2014.
- [94] L. Sun, X. He, J. Wang, and J. Lu, "Deformation and Failure Mechanisms of Nanotwinned Copper Films with a Pre-Existing Crack," *Materials Science and Engineering: A*, vol. 606, pp. 334–345, 2014.
- [95] Y.-G. Zheng, Y.-F. Fu, H.-W. Zhang, and H.-F. Ye, "Atomistic Investigations of Tensile and Shear Mechanical Properties of Nanotwinned Copper with

- Embedded Defects," *International Journal of Computational Materials Science and Engineering*, vol. 3, no. 02, 2014.
- [96] I. Shabib and R. Miller, "A Molecular Dynamics Study of Twin Width, Grain Size and Temperature Effects on the Toughness of 2D-Columnar Nanotwinned Copper," *Modelling and Simulation in Materials Science and Engineering*, vol. 17, no. 5, p. 055009, 2009.
- [97] H. Zhou, S. Qu, and W. Yang, "Toughening by Nano-Scaled Twin Boundaries in Nanocrystals," *Modelling and Simulation in Materials Science and Engineering*, vol. 18, no. 6, p. 065002, 2010.
- [98] A. Singh, L. Tang, M. Dao, L. Lu, and S. Suresh, "Fracture Toughness and Fatigue Crack Growth Characteristics of Nanotwinned Copper," *Acta Materialia*, vol. 59, no. 6, pp. 2437–2446, 2011.
- [99] E. Qin, L. Lu, N. Tao, J. Tan, and K. Lu, "Enhanced Fracture Toughness and Strength in Bulk Nanocrystalline Cu with Nanoscale Twin Bundles," *Acta Materialia*, vol. 57, no. 20, pp. 6215–6225, 2009.
- [100] A. Hasnaoui, H. Van Swygenhoven, and P. Derlet, "Dimples on Nanocrystalline Fracture Surfaces as Evidence for Shear Plane Formation," *Science*, vol. 300, no. 5625, pp. 1550–1552, 2003.
- [101] F. Dalla Torre, H. Van Swygenhoven, and M. Victoria, "Nanocrystalline Electrodeposited Ni: Microstructure and Tensile Properties," *Acta Materialia*, vol. 50, no. 15, pp. 3957–3970, 2002.
- [102] T. Zhu and H. Gao, "Plastic Deformation Mechanism in Nanotwinned Metals: An Insight from Molecular Dynamics and Mechanistic Modeling," *Scripta Materialia*, vol. 66, no. 11, pp. 843–848, 2012.

- [103] L. Zhu, H. Ruan, X. Li, M. Dao, H. Gao, and J. Lu, "Modeling Grain Size Dependent Optimal Twin Spacing for Achieving Ultimate High Strength and Related High Ductility in Nanotwinned Metals," *Acta Materialia*, vol. 59, no. 14, pp. 5544–5557, 2011.
- [104] S. Qu, P. Zhang, S. Wu, Q. Zang, and Z. Zhang, "Twin Boundaries: Strong or Weak?" *Scripta Materialia*, vol. 59, no. 10, pp. 1131–1134, 2008.
- [105] P. Zhang, Z. Zhang, L. Li, and Z. Zhang, "Twin Boundary: Stronger or Weaker Interface to Resist Fatigue Cracking?" *Scripta Materialia*, vol. 66, no. 11, pp. 854–859, 2012.
- [106] Y. Cheng, Z.-H. Jin, Y. Zhang, and H. Gao, "On Intrinsic Brittleness and Ductility of Intergranular Fracture along Symmetrical Tilt Grain Boundaries in Copper," *Acta Materialia*, vol. 58, no. 7, pp. 2293–2299, 2010.
- [107] S. Nosé, "A Unified Formulation of the Constant Temperature Molecular Dynamics Methods," *The Journal of Chemical Physics*, vol. 81, no. 1, pp. 511–519, 1984.
- [108] X.-Y. Liu, F. Ercolessi, and J. B. Adams, "Aluminium Interatomic Potential from Density Functional Theory Calculations with Improved Stacking Fault Energy," *Modelling and Simulation in Materials Science and Engineering*, vol. 12, no. 4, p. 665, 2004.
- [109] Y. Mishin, M. Mehl, D. Papaconstantopoulos, A. Voter, and J. Kress, "Structural Stability and Lattice Defects in Copper: Ab Initio, Tight-Binding, and Embedded-Atom Calculations," *Physical Review B*, vol. 63, no. 22, p. 224106, 2001.

- [110] P. Williams, Y. Mishin, and J. Hamilton, "An Embedded-Atom Potential for the Cu–Ag System," *Modelling and Simulation in Materials Science and Engineering*, vol. 14, no. 5, p. 817, 2006.
- [111] A. F. Voter and S. P. Chen, "Accurate Interatomic Potentials for Ni, Al and Ni₃Al," in *MRS Proceedings*, vol. 82. Cambridge Univ Press, 1986, p. 175.
- [112] A. G. Frøseth, P. M. Derlet, and H. Van Swygenhoven, "Twinning in Nanocrystalline FCC Metals," *Advanced Engineering Materials*, vol. 7, no. 1-2, pp. 16–20, 2005.
- [113] S. Hu, C. H. Henager Jr, and L. Chen, "Simulations of Stress-Induced Twinning and De-Twinning: A Phase Field Model," *Acta Materialia*, vol. 58, no. 19, pp. 6554–6564, 2010.
- [114] C.-T. Lu and K. Dayal, "Linear Instability Signals the Initiation of Motion of a Twin Plane under Load," *Philosophical Magazine Letters*, vol. 91, no. 4, pp. 264–271, 2011.
- [115] H. Van Swygenhoven, P. Derlet, and A. Frøseth, "Stacking Fault Energies and Slip in Nanocrystalline Metals," *Nature Materials*, vol. 3, no. 6, pp. 399–403, 2004.
- [116] J. W. Christian and S. Mahajan, "Deformation Twinning," *Progress in Materials Science*, vol. 39, no. 1, pp. 1–157, 1995.
- [117] G. G. Yapici, I. Karaman, and Z.-P. Luo, "Mechanical Twinning and Texture Evolution in Severely Deformed Ti–6Al–4V at High Temperatures," *Acta Materialia*, vol. 54, no. 14, pp. 3755–3771, 2006.
- [118] N. Bernstein and E. Tadmor, "Tight-Binding Calculations of Stacking Energies and Twinnability in FCC Metals," *Physical Review B*, vol. 69, no. 9, p. 094116, 2004.

- [119] J. R. Rice, "Dislocation Nucleation from a Crack Tip: an Analysis Based on the Peierls Concept," *Journal of the Mechanics and Physics of Solids*, vol. 40, no. 2, pp. 239–271, 1992.
- [120] V. Yamakov, D. Wolf, S. Phillpot, and H. Gleiter, "Deformation Twinning in Nanocrystalline Al by Molecular-Dynamics Simulation," *Acta Materialia*, vol. 50, no. 20, pp. 5005–5020, 2002.
- [121] M. Chen, E. Ma, K. J. Hemker, H. Sheng, Y. Wang, and X. Cheng, "Deformation Twinning in Nanocrystalline Aluminum," *Science*, vol. 300, no. 5623, pp. 1275–1277, 2003.
- [122] N. Sermollo, T. Sinha, and Y. Kulkarni, unpublished.
- [123] S. Ryu, K. Kang, and W. Cai, "Entropic Effect on the Rate of Dislocation Nucleation," *Proceedings of the National Academy of Sciences*, vol. 108, no. 13, pp. 5174–5178, 2011.
- [124] T. Sinha and Y. Kulkarni, "Anomalous Deformation Twinning in FCC Metals at High Temperatures," *Journal of Applied Physics*, vol. 109, no. 11, p. 114315, 2011.
- [125] J. Schiøtz and A. Carlsson, "The Influence of Surface Stress on Dislocation Emission from Sharp and Blunt Cracks in FCC Metals," *Philosophical Magazine A*, vol. 80, no. 1, pp. 69–82, 2000.
- [126] F. Sansoz, H. Huang, and D. H. Warner, "An Atomistic Perspective on Twinning Phenomena in Nano-Enhanced FCC Metals," *Journal Of the Minerals*, vol. 60, no. 9, pp. 79–84, 2008.
- [127] D. Hull and D. J. Bacon, *Introduction to Dislocations*. Butterworth-Heinemann, 2001.

- [128] J. Schiøtz, L. Canel, and A. Carlsson, "Effects of Crack Tip Geometry on Dislocation Emission and Cleavage: A Possible Path to Enhanced Ductility," *Physical Review B*, vol. 55, no. 10, p. 6211, 1997.
- [129] A. Cao and Y. Wei, "Molecular Dynamics Simulation of Plastic Deformation of Nanotwinned Copper," *Journal of Applied Physics*, vol. 102, no. 8, p. 083511, 2007.
- [130] K. J. Hsia, Z. Suo, and W. Yang, "Cleavage due to Dislocation Confinement in Layered Materials," *Journal of the Mechanics and Physics of Solids*, vol. 42, no. 6, pp. 877–896, 1994.
- [131] M. D. Uchic, D. M. Dimiduk, J. N. Florando, and W. D. Nix, "Sample Dimensions Influence Strength and Crystal Plasticity," *Science*, vol. 305, no. 5686, pp. 986–989, 2004.
- [132] V. Deshpande, A. Needleman, and E. Van der Giessen, "Plasticity Size Effects in Tension and Compression of Single Crystals," *Journal of the Mechanics and Physics of Solids*, vol. 53, no. 12, pp. 2661–2691, 2005.
- [133] J. R. Greer and W. D. Nix, "Size Dependence of Mechanical Properties of Gold at the Sub-Micron Scale," *Applied Physics A*, vol. 80, no. 8, pp. 1625–1629, 2005.
- [134] F. Hammami and Y. Kulkarni, "Size Effects in Twinned Nanopillars," *Journal of Applied Physics*, vol. 116, no. 3, p. 033512, 2014.
- [135] R. Armstrong, "The (Cleavage) Strength of Pre-Cracked Polycrystals," *Engineering Fracture Mechanics*, vol. 28, no. 5, pp. 529–538, 1987.
- [136] T. Sinha and Y. Kulkarni, "Alternating Brittle and Ductile Response of Twin boundaries in Nanotwinned Structures," 2014, under review.

- [137] I. Shabib and R. E. Miller, "Deformation Characteristics and Stress–Strain Response of Nanotwinned Copper via Molecular Dynamics Simulation," *Acta Materialia*, vol. 57, no. 15, pp. 4364–4373, 2009.
- [138] S. Jiao and Y. Kulkarni, "Radiation Response of Nanotwinned Metals," 2014, to be published.
- [139] V. Yamakov, D. Wolf, S. Phillpot, and H. Gleiter, "Dislocation–Dislocation and Dislocation–Twin Reactions in Nanocrystalline Al by Molecular Dynamics Simulation," *Acta Materialia*, vol. 51, no. 14, pp. 4135–4147, 2003.
- [140] A. Frøseth, H. Van Swygenhoven, and P. Derlet, "The Influence of Twins on the Mechanical Properties of nc-Al," *Acta Materialia*, vol. 52, no. 8, pp. 2259–2268, 2004.
- [141] Y. M. Wang, F. Sansoz, T. LaGrange, R. T. Ott, J. Marian, T. W. Barbee Jr, and A. V. Hamza, "Defective Twin Boundaries in Nanotwinned Metals," *Nature Materials*, vol. 12, no. 8, pp. 697–702, 2013.
- [142] H. Van Swygenhoven, P. Derlet, and A. Hasnaoui, "Atomic Mechanism for Dislocation Emission from Nanosized Grain Boundaries," *Physical Review B*, vol. 66, no. 2, p. 024101, 2002.
- [143] Z. Wu, Y. Zhang, and D. Srolovitz, "Deformation Mechanisms, Length Scales and Optimizing the Mechanical Properties of Nanotwinned Metals," *Acta Materialia*, vol. 59, no. 18, pp. 6890–6900, 2011.
- [144] T. T. Lau, A. Kushima, and S. Yip, "Atomistic Simulation of Creep in a Nanocrystal," *Physical Review Letters*, vol. 104, no. 17, p. 175501, 2010.

